From Quantum Mechanics to Experimental Observables: Computational Investigations of Energy-Related Heterogeneous Catalysts

Thesis by

Jin Qian

In Partial Fulfillment of the Requirements for

the degree of

Doctor of Philosophy

CALIFORNIA INSTITUTE OF TECHNOLOGY

Pasadena, California

2019

(Defended January 8th, 2019)

Jin Qian
ORCID: [0000-0002-0162-0477]

ACKNOWLEDGEMENTS

First, I would like to express my sincere gratitude to my advisor Prof. William A. Goddard III for the continuous support of my Ph.D study and related research, for his patience, motivation, and immense knowledge. I am amazed by his broad understanding, sharp chemical intuition, and high standard for science. He's not only a world-class scientist, but also a wise mentor for life. When I felt most frustrated, he shared with me that what is most important question is to "think what you want to do for life," and that "once the mind is set, you should just go for it". His guidance helped me during my research and I could not have imagined having a better advisor and mentor for my Ph.D study.

Besides my advisor, I would like to thank the rest of my thesis committee: Professor Brent Fultz, Professor Harry Atwater, and Professor Manuel Soriaga for their insightful comments and encouragement, and also for the hard questions which incented me to widen my research from various perspectives.

My sincere thanks also goes to Dr. Ethan Crumlin and Dr. Yano Junko at the Lawrence Berkeley National Lab. They were great mentors and collaborators who gave me access to the laboratory and research facilities. Dr. Crumlin shared his knowledge, experiences, and distinct perspectives as an experimental expert in the leading field of ambient pressure XPS. He motivated me to jump out of the box and discover my full potential. He made me realize how powerful and fruitful it is when we work closely as a team with theory and experiment hand in hand. Without the precious support of these metors, it would not have been possible to conduct the CO_2 reduction and H_2O adsorption research. I thank Dr. Yifan Ye, who has worked very closely with me in the Lawrence Berkeley National Lab for being such a wonderful experimental collaborator. Thank you for the countless honest discussions and feedbacks, that kept polishing and refining our hypotheses until we got down to the truth. Thank you for being such a knowledgeable, patient, compassionate, and cheerful collaborator and friend.

My next thanks go to Dr. Rebecca Fushimi and Dr. Yixiao Wang from Idaho National Lab. I enjoyed our discussions on Haber Bosch related research. I also want to thank Dr. Robert

"Smith" Nielsen, Dr. Alessandro Fortunelli, Dr. Qi An, Prof. Hai Xiao, and Dr. Tao Chen for opening the door of surface catalysis for me.

I thank my fellow lab mates for the stimulating discussions, for the weekdays and weekends we worked together, and for all the fun we have had in the last four years. Thank you Yalu Chen for being a great friend, for sharing funny stories, and for all the laughter. Thank you Dr. Soonho Kwon, and Dr. Hyeyoung Shin for the memorable trip and for always being so kind and supportive. Thank you Dr. Yufeng Huang and Prof. Yuanyue Liu, my "lunch buddies", for all the insightful and interesting discussions at the table. I thank all my friends at Caltech and outside Caltech for their emotional support.

Last but not the least, I would like to give my biggest thanks to my family: my parents, my husband Han, his family, and my two cats, Tom-Yum and Frederic, for their emotional support and unconditional love throughout my life.

ABSTRACT

One of the most severe challenges in this decade is assuring more secure, more efficient, cleaner, and more sustainable energy to power our world. This work takes a catalytic approach to help overcome this challenge.

The Haber Bosch process is one of the towering achievements of industrial chemistry. It consumes a huge amount of energy due to the high temperature and high pressure reaction condition, and in turn, has enabled us to produce enough nitrogen fertilizer to feed the current world population. An essential goal of present research is therefore to dramatically reduce Haber Bosch energy cost by improving the catalytic performance of the presently used Fe-based heterogeneous catalysts. We use quantum mechanics (QM) and kinetic Monte Carlo (kMC) to predict reaction mechanisms and kinetics for NH_3 synthesis on Fe(111) – the best Fe single crystal surface for NH_3 synthesis. We find excellent agreement with a predicted turnover frequency (TOF) of 17.7 sec^{-1} per 2x2 site (5.3 x 10^{-9} moles/cm^2/sec) compared to TOF=10 sec^{-1} per site from experiment, and we further predict that top-layer Co doping leads to an acceleration by a factor of 2.3 in reaction rates of ammonia synthesis.

Compared to the industrialized Haber Bosch reaction, renewable energy technologies are still in their infancy with a great deal of questions unanswered, as well as a lot of barriers to overcome. Here we report our atomistic understanding of how CO_2 and H_2O molecules adsorb on the catalyst surface and interact to initiate CO_2 dissociation and subsequent product formation. Using synergistic experimental and theoretical analyses, we show that Cu and Ag operate entirely differently for the first step of activating CO_2. We develop a method of predicting the ambient pressure XPS spectrum in an ab-initio multiscale fashion: from electronic structure, to atomic picture, to chemical reaction network (CRN), and eventually to the experimental observable. We bridge both the qualitative and quantitative gap from quantum mechanics to XPS, and demonstrate our approach by decoding the initial H_2O adsorption and complex formation on Ag(111) surface, which we encourage to be the new standard protocol in this field.

PUBLISHED CONTENT AND CONTRIBUTIONS

Jin Qian, Qi An, Alessandro Fortunelli, Robert J. Nielsen, and William A. Goddard III*. "Reaction mechanism and kinetics for ammonia synthesis on the Fe (111) Surface." *Journal of the American Chemical Society* 140, no. 20 (2018): 6288-6297. doi: 10.1021/jacs.7b13409.

J.Q. participated in the conception of the project, built up the mechanism, conducted all QM calculations, and wrote the manuscript.

Jin Qian, Alessandro Fortunelli, and William A. Goddard III*. "Effect of Co Doping on Mechanism and Kinetics of Ammonia Synthesis on Fe(111) Surface." *Journal of catalysis*. Submitted Oct 2018, under review and revise.

J.Q. participated in the conception of the project, built up the mechanism, conducted all QM calculations, and wrote the manuscript.

Yifan Ye, Hao Yang, **Jin Qian**, Hongyang Su, Kyung-Jae Lee, Tao Cheng, Hai Xiao, Junko Yano*, William A. Goddard III*, and Ethan Crumlin*. " Dramatic differences in CO_2 adsorption and initial steps of reduction between Ag and Cu." *Nature Communication.* Submitted Oct 2018, Accepted.

J.Q. participated in the conception of the project, conducted calculations, and helped writing the manuscript.

Jin Qian, Yifan Ye, Hao Yang, Junko Yano*, Ethan Crumlin* and William A. Goddard III*. "Bridging the gap between Quantum Mechanics Calculations and XPS Spectroscopy: Decoding the initial H_2O adsorption and complex formation on Ag(111) surface.", *Journal of the American Chemical Society*. Submitted Dec 2018, under review.

J.Q. participated in the conception of the project, built up the mechanism, conducted all calculations, and wrote the manuscript.

TABLE OF CONTENTS

LIST OF ILLUSTRATIONS AND/OR TABLES

Figure Number *Page*

Table Number *Page*

C h a p t e r 1

Introduction

1. 1 Statement of Problem

World population growth speed topped around the 1960s, and is projected to rise by nearly 2.5 billion. It is predicted to increase from 7.3 billion to an estimated 9.8 billion between 2015 and 2050. Despite the notable improvements in decreasing hunger and poverty on a global scale, progress has been slow in countries with high fertility rates of in recent decades. Unfortunately, nations with the fastest growing populations tend to suffer more from poverty, hunger, pollution, environmental degradation, and fragility. Moreover, many of these countries face enormous obstacles to economic development in the form of climate change, regional or ethnic conflict, or water scarcity. [1-2] Further understanding and optimization of current industrialized technologies are needed to overcome these obstacles. Such technologies include, but are not limited to the Haber Bosch reaction of producing ammonia that feeds the growing population. Thus, the first half of the current work (Chapter 2 to 3) is dedicated to Haber Bosch process.

Although abundant in food and resources, the world's leading countries are facing a different kind of challenge: the transition from conventional energy to renewable energy. According to reference [3], renewable energy technologies can meet much of the growing demand at prices lower than those usually forecast for conventional energy, if adequate support is provided from policies and scientific advancement. By the year of 2050, renewable sources of energy are predicted to account for three-fifths of the world's electricity market, as well as two-fifths of the market for fuels used directly. In addition, the transition from a conventional energy economy to a renewables-intensive one could provide environmental and other benefits, which are not measured in standard economic accounts. These benefits include but are not limited to: social and economic development, land restoration, reduced air pollution,

abatement of global warming, fuel supply diversity, and reduction of the risks of nuclear weapons proliferation. Given all these benefits, renewable clean energy is necessarily required. Therefore, the second half (Chapters 4 and 5) is dedicated to renewable energy.

1.2 The Catalytic Approach

We take a catalytic approach to attempt to solve these energy-related challenges. A good catalyst can provide an active site that optimizes the residence time of the adsorbate, as well as helping its conversion into desirable products. [4] In general, there are three big classes of catalysis: homogeneous catalysis, biological catalysis, and heterogeneous catalysis. Homogeneous catalysis refers to a catalytic reaction where the catalyst and the reactants are in the same phase. Molecular catalysts and single-site catalysts are representatives of this class. [5] As for biological catalysis, enzymes are arguably the most famous representatives. [6] Heterogeneous catalysis, by definition, represent systems where the catalyst is in a different phase from that of the reactants. [7] Solids can catalyze reactions of molecules in either the gas or solution phase, and the reactions at the interfaces are of special complexity and interest. These systems can be far from thermodynamic equilibrium, and a wide range of phenomena, such as rate oscillations, spatiotemporal patterns and chaos has been observed and reported. [8-10]

Heterogeneous catalysis has been of special interest throughout history. Our knowledge about heterogeneous catalysis has been continuously expanding, and the timeline is summarized and sketched in the bottom half of Figure 1-1 in black. The information in Figure 1-1 is adopted from reference [11] and reference [12]. Ever since Davy discovered in the early 1800s that the mixture of coal gas and air makes platinum wire white hot, the field paused for several decades. It started booming thanks to a series of inventions of experimental methods such as Infrared Spectroscopy, UHV (ultra high vacuum), TPD (temperature programed desorption), LEED (low energy electron diffraction), XPS (X-ray photoelectron spectroscopy), XAS (X-ray adsorption spectroscopy), etc.

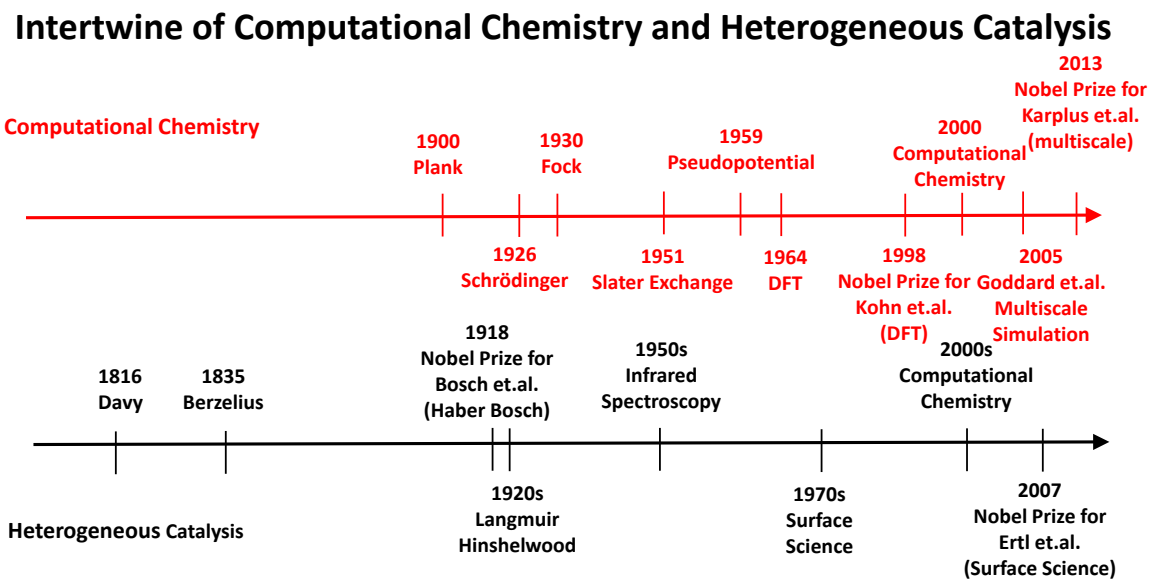

Figure 1-1. Intertwine of computational chemistry and heterogeneous catalysis on parallel timeline. The field of heterogeneous catalysis advanced rapidly twice in the history: once in the 1950s, and once since 2000s; thanks to the inventions characterization techniques and later the wide adaption of computational chemistry in research labs.

1.3 Computational Method

The goal of molecular electronic structure theory is prediction of molecular structure and properties by solving the equations of quantum mechanics from first principles—or "ab initio". [13] As summarized in Figure 1-1, quantum mechanics revolutionized people's understanding of physics and chemistry. The proposition of Schrödinger equation opened a new chapter in human history, but it was not until the Hatree-Fock theory that the solution of many-body electron systems could be approximated. The detailed derivation from the simple hydrogen atom to many body systems can be found in reference [14] but it is not within the scope of current thesis.

The Density Functional Theory (DFT) is the current area of interest, as the calculations of a series of desired properties such as geometries, electronic energies, zero point energies, and

vibrational frequencies are possible. [15] The flavor of DFT, including the choice of functional, is of special importance, as it describes the quality of exchanged energy approximation. [16] A good balance between computational expense and accuracy must be achieved. Most of the calculations within this work are carried using VASP [17] software package, at GGA (general gradient approximation) level in order to solve problems in heterogeneous catalysis. The following sections are brief discussions of energy-related applications in catalysis using the method of DFT.

1.4 Optimize the Industrialized Technology: Haber Bosch

The first half of the current work (Chapters 2 and 3) is dedicated to the Haber Bosch process, which consumes a huge amount of energy due to the high temperature and high pressure reaction condition, and in turn, has enabled us to produce enough nitrogen fertilizer to feed the current world population.

Several transition metals, such as iron, ruthenium, osmium, uranium and cobalt-molybdenum, catalyze the Haber-Bosch process, but iron is still the most common and attractive choice because of its hardness and low cost. An essential goal of modern-day research is therefore to dramatically reduce Haber Bosch energy cost by improving the catalytic performance of the presently used Fe-based catalysts. In order to do so, we need to first understand the mechanism, and then look at possible improvements. In our full mechanism study (Chapter 2), we combined Quantum Mechanics and Kinetic Monte Carlo to predict the turn over frequency (TOF) for Fe(111) surface, the most reactive surface reported, and found an excellent agreement with the TOF from experiment. Large change in spin and magnetic moment was found during critical reaction steps. This observation motivated us to further investigate the effect of modified spin, such as by using Co dopant.

In Chapter 3, we build up on the findings from Chapter 2 and conclude that at typical target condition T = 673 K, $P(H_2)$ = 15 atm, $P(N_2)$ = 5 atm, and $P(NH_3)$ = 1 atm, top-layer Co doping leads to an acceleration by a factor of 2.3 in reaction rates of ammonia synthesis, and therefore an expected corresponding decrease in production costs. We also purpose a

nomenclature guideline that carefully takes into consideration the extra degree of freedom due to the symmetry breaking introduced by surface Co dopant. This guideline can be generalized and applied to any dopant system. We study the full mechanism with surface Co dopant using QM, and then feed the QM data into kinetic Monte Carlo to get the final TOF of ammonia. The work in Chapter 2 and 3 could be interesting to theorists and experimentalists alike in the field of catalysis. Theorists would benefit from a detailed guideline for doping in general, as well as the complete reaction mechanism for producing ammonia. Experimentalists could be interested in conducting experiments comparing pure Fe catalyst and Co-doped catalyst under a realistic Haber Bosch process condition.

1.5 Explore the Renewable Energy Option: CO_2 reduction

After we address the challenges in industrialized catalytic process, the second half of this current work (Chapter 4 and 5) is dedicated to state-of-art renewable energy applications.

A national priority is to reduce CO_2 to produce energy, liquid fuels, and hydrocarbon feedstocks. Current electrocatalysts are not adequate, and enormous experiment and quantum mechanics (QM) theoretical efforts are underway to discover new catalysts that are energy efficient, selective in producing specific hydrocarbon or oxygenated products (HCOx hereafter), and comprised of earth abundant materials. A great deal of progress has been made with empirically inspired approaches but faster progress is needed. High throughput experimental and computational screening methods have been employed to discover new alloys or compounds but are based on preconceived notions or the reaction scheme. To expedite this research, we describe in Chapter 4 the development of a complete atomistic understanding of how CO_2 interacts with catalyst surfaces is required to empower guided catalyst design to selectively tune the mechanisms for adsorption and activation.

Along the line with this research, we find H_2O adsorption on the same catalytic surface of specific interest. From the catalytic point of view, it is important to understand because it is directly related to the next hydrogenations steps of CO_2 reduction. It is crucial from a fundamental point of view in science as well because it is a good toy model for the

experimental test of our theory. XPS experiments allow us to probe the oxygen containing species, who leave a “fingerprint” due to their different chemical environments. In the meantime, DFT calculations allow us to predict the electronic structure, and thus the corelevel shift of such species. Furthermore, kinetic theory allows us to build up a network of reactions with different rates, and eventually determine the equilibrium populations of oxygen containing species on the surface. We demonstrate in Chapter 5 a creative protocol of understanding the XPS data, which we urge to become the new standard in this field.

BIBLIOGRAPHY

(1) Walker, Robert J. "Population Growth and its Implications for Global Security." American Journal of Economics and Sociology 75, no. 4 (2016): 980-1004.

(2) Boserup, Ester. *The conditions of agricultural growth: The economics of agrarian change under population pressure*. Routledge, 2017.

(3) Johansson, Thomas B., Amulya KN Reddy, Henry Kelly, Robert H. Williams, and Laurie Burnham, eds. *Renewable energy: sources for fuels and electricity*. Island press, 1993.

(4) Thomas, John Meurig, Robert Raja, and Dewi W. Lewis. "Single-site heterogeneous catalysts." *Angewandte Chemie International Edition* 44, no. 40 (2005): 6456-6482.

(5) Bhaduri, Sumit, and Doble Mukesh. *Homogeneous catalysis: mechanisms and industrial applications*. John Wiley & Sons, 2014

(6) Benkovic, Stephen J., and Sharon Hammes-Schiffer. "A perspective on enzyme catalysis." *Science* 301, no. 5637 (2003): 1196-1202.

(7) Thomas, John Meurig, and W. John Thomas. *Principles and practice of heterogeneous catalysis*. John Wiley & Sons, 2014.

(8) Imbihl, Ronald, and Gerhard Ertl. "Oscillatory kinetics in heterogeneous catalysis." *Chemical Reviews* 95, no. 3 (1995): 697-733.

(9) King, David Anthony, ed. *The chemical physics of solid surfaces and heterogeneous catalysis*. Vol. 5. Elsevier, 2012.

(10) Wicke, E., P. Kummann, W. Keil, and J. Schiefler. "Unstable and oscillatory behaviour in heterogeneous catalysis." *Berichte der Bunsengesellschaft für physikalische Chemie* 84, no. 4 (1980): 315-323.

(11) Chorkendorff, Ib, and Johannes W. Niemantsverdriet. Concepts of modern catalysis and kinetics. John Wiley & Sons, 2017.

(12) Ertl, Gerhard. "Reactions at surfaces: from atoms to complexity (Nobel Lecture)." *Angewandte Chemie International Edition* 47, no. 19 (2008): 3524-3535.

(13) Shao, Yihan, Laszlo Fusti Molnar, Yousung Jung, Jörg Kussmann, Christian Ochsenfeld, Shawn T. Brown, Andrew TB Gilbert et al. "Advances in methods and algorithms in a modern quantum chemistry program package." *Physical Chemistry Chemical Physics* 8, no. 27 (2006): 3172-3191.

(14) Szabo, Attila, and Neil S. Ostlund. *Modern quantum chemistry: introduction to advanced electronic structure theory*. Courier Corporation, 2012.

(15) Bauschlicher Jr, Charles W. "A comparison of the accuracy of different functionals." *Chemical Physics Letters* 246, no. 1-2 (1995): 40-44.(11) Chorkendorff, Ib, and Johannes W. Niemantsverdriet. Concepts of modern catalysis and kinetics. John Wiley & Sons, 2017.

(16) Becke, Axel D. "Density-functional exchange-energy approximation with correct asymptotic behavior." *Physical review A* 38, no. 6 (1988): 3098.

(17) Kresse, Georg, and Jürgen Furthmüller. "Efficient iterative schemes for ab initio total-energy calculations using a plane-wave basis set." *Physical review B* 54, no. 16 (1996): 1116988): 3098. Kresse, Georg, and Jürgen Furthmüller. "Efficient iterative schemes for ab initio total-

energy calculations using a plane-wave basis set." *Physical review B* 54, no. 16 (1996): 11169.

(16) Perdew, John P., Kieron Burke, and Matthias Ernzerhof. "Generalized gradient approximation made simple." *Physical review letters* 77, no. 18 (1996): 3865.

C h a p t e r 2

Reaction Mechanism and Kinetics for Ammonia Synthesis On the Fe (111) surface

Jin Qian, Qi An, Alessandro Fortunelli, Robert J. Nielsen, and William A. Goddard III*. "Reaction mechanism and kinetics for ammonia synthesis on the Fe (111) Surface." *Journal of the American Chemical Society* 140, no. 20 (2018): 6288-6297. doi: 10.1021/jacs.7b13409.

Abstract

The Haber Bosch industrial process for synthesis of ammonia (NH_3) from hydrogen (H_2) and nitrogen (N_2), produces the millions of tons of ammonia gas annually needed to produce nitrates for fertilizers required to feed the earth's growing populations. This process has been optimized extensively, but it still uses enormous amounts of energy (2% of the world's supply), making it essential to dramatically improve its efficiency. To provide guidelines to accelerate this improvement, we used quantum mechanics (QM) to predict reaction mechanisms and kinetics for NH_3 synthesis on Fe(111) – the best Fe single crystal surface for NH_3 synthesis. We predicted the free energies of all reaction barriers for all steps in the mechanism and built these results into a kinetic Monte Carlo model for predicting steady state catalytic rates to compare with single-crystal experiments at 673 °K and 20 atm. We find excellent agreement with a predicted turnover frequency (TOF) of 17.7 sec^{-1} per 2x2 site (5.3 x 10^{-9} moles/cm^2/sec) compared to TOF=10 sec^{-1} per site from experiment.

2. 1. Introduction

The invention of the Haber-Bosch process for converting nitrogen gas (N_2) and hydrogen gas (H_2) into the ammonia (NH_3) needed to generate the nitrates for the fertilizers underlying the agricultural revolution that feeds the world, is one of the greatest advances from scientific research. Millions of tons of NH_3 are produced each year [1] for agricultural and industrial purposes. Efficiency of up to 70% [2] has been achieved with commercially available iron based catalysts [3] and with ruthenium-based catalysts under lab settings [4]. Ruthenium-based catalysts are more active than iron-based ones [5-6], and have been recently further

developed. [7-8] However, ruthenium-based catalysts suffer from environmental problems due to ruthenium's scarce abundance in Earth's crust, high cost, together with its toxicity when in the form of compounds [9], so that the industrial Haber-Bosch process is still based on iron catalysts. The industrial Haber-Bosch process requires drastic conditions of temperature (700°K-850°K) and pressure (50-200atm), consuming 2% of the world's power, [3, 5, 10-12] which has motivated repeated attempts to improve the efficiency of Fe catalyst. [5]

In order to provide a basis for making more rapid progress in such improvements, we want to use QM to determine the reaction mechanism and rates to help guide the search for improvements. In order to validate the QM predictions, we need to compare to experiments on well characterized surfaces. Fortunately, Somorjai et al [13] reported comprehensive investigations of the rates for NH_3 synthesis on Fe single crystals to which we can compare directly. Somorjai et al considered a pressure of 20 atm and temperatures in the range of 638 to 723°K, to determine the rates of ammonia formation. For 673°K they found relative rates of 418: 25: 1 for Fe(111), Fe(100), and Fe(110) surfaces, respectively. In another study [14], they concluded that C7 sites (Fe atoms with seven nearest neighbors) are the most active in iron ammonia synthesis catalysts. Such sites involve the top three layers of Fe(111) exposed to the reactant gases, rationalizing the reactivity of Fe(111) > Fe(100) > Fe(110). Somorjai showed that small amounts of K promote the catalysis increasing the rates by a factor of 2. However the location of the K in the catalyst is not known, so we will compare to Somorjai results for the most active Fe(111) bare surface without K or other promoters.

We report here QM calculations on the 26 surface adsorbate configurations important in the **full reaction mechanism including the free energy barriers** that determine the rates for the 17 steps that we find to play an important role in the catalysis under Somorjai conditions. Then we use these predicted rates in a self-consistent kinetic Monte Carlo (kMC) model to predict the steady state rates of all the reaction steps to obtain the turn over frequency (TOF) for the Somorjai single crystal conditions. At 673K and 20 atm pressure, **we predict TOF=17.7 sec^{-1} per 2x2 site (5.3 x 10^{-9} moles/sec-cm^2), which is in excellent agreement**

with the experimental TOF=9.7 sec^{-1}. This validates our modeling results, providing the basis for using theory to help design improved catalytic systems.

2. 2 Methods

For these QM studies we use the Perdew-Burke-Ernzerhof (PBE) flavor of Density Functional theory (DFT). including the D3 (Becke Johnson) [15] empirical corrections for long range London dispersion (van der Waals attraction). [16] The reason is that this level of QM has been validated recently for several systems. Thus reference[17] carried out systematic studies for the oxygen reduction reaction (ORR, O_2 + protons ➔ H_2O) on Pt(111) using the same PBE-D3 level as in this paper. Including 5 layers of explicit solvent in QM metadynamics on all reaction steps, comparisons could be made to experimental activation barriers for two values of the external potential. In both cases the calculated activation barriers were within 0.05 eV of the experiment.

For the CO reduction reaction on Cu(100) the same level of theory obtains an activation energy within 0.05 eV of experiment. [18-21] This same level of theory has also led to similar accuracy for the oxygen evolution reaction on IrO_2 [22] and for onset potentials on Cu(111). [23-25]

This is not a guarantee that PBE-D3 will work as well for Fe, where the presence of unpaired spins could cause problems, but it provides a reasonable starting point. Indeed, the accuracy compared to experiment seems to be comparable to these other cases.

Indeed, we carried out exactly the same set of calculations at the PBE level without D3 (results in the SI) and find TOF=89.3 compared to 17.7 for PBE-D3 and 9.7 experiment. This indicates that for this system PBE-D3 provides better accuracy than pure PBE.

All calculations were carried out with the VASP [26] software package. We established that an energy cutoff of 400eV leads to converged forces. The K-point sampling was chosen to be 4 x 4 x 1. All calculations include spin-polarization.

2.2.a Small Gas Molecules

Calculations for the gas phase molecules used the PBE functional (as implemented in Jaguar) with the D3 empirical correction for London dispersion. [15, 27-29] Free energy corrections including enthalpy (H), entropy (S), and zero-point energy (ZPE) from Jaguar calculations are included in Supplemental Information (SI).

To obtain the total free energy, G=H-TS, for the gas molecules at temperature T, we add to the DFT electronic energy (E), the zero-point energy (ZPE) from the vibrational levels (described as simple harmonic oscillators), and the specific heat corrections in the enthalpy from 0 to T. The entropy (S), as a sum of vibrational, rotational and translational contributions, are evaluated from the same levels. To correct the free energy for pressure, we assume an ideal gas and add $RT*\ln(P_2/P_1)$ with a reference pressure of P= 1 atm.

The Free energy changes (δG) for the overall Haber Bosch reaction $N_2+3H_2 \Rightarrow 2NH_3$ under various conditions are calculated as

$$\delta G=2*E(NH_3)+2*ZPE(NH_3)+2*H(NH_3)-2T*S(NH_3)-$$
$$[E(N_2)+3*E(H_2)+ZPE(N_2)+3*ZPE(H_2)+H(N_2)+3*H(H_2)-T*S(N_2)-3T*S(H_2)]$$

The pressure dependence is added using $RT*\ln(P_2/P_1)$, 5atm and 15atm for N_2 and H_2 respectively. We calculate δG is -0.52 eV for the reaction under 673°K, and 20atm total pressure, which can be compared with δG =-0.02eV at 700°K and 5:15:1 atm N_2, H_2 and NH_3, respectively, from experiment. [30] We calculate δG is –1.22 eV for the reaction under 673°K, 5atm: 15atm: 1.5 torr for N_2, H_2, and NH_3 respectively.

2.2.b Surface Optimization

The PBE-D3(BJ) level of DFT leads to a calculated lattice parameter of a = 2.807 Å for the bulk Fe bcc structure at 0°K, slightly smaller than the experimental value 2.866 Å at 298°K. [31] This level of DFT predicts a magnetic moment for bulk Fe of 2.23 μB in excellent agreement with the experimental value, 2.22 μB. [31]

For calculating the surface chemistry, we selected the (111) surface which Somorjai showed to be the most active catalytically. For these DFT calculations we use a two-dimensional periodic slab with six layers of Fe atoms each of which consists of a (2 x 2) (6.912 Å x 8.276 Å) unit cell (4 surface Fe per cell). We include 15 Å of vacuum in the z direction to minimize

possible interactions between the replicated cells. The top five layers are relaxed while the bottom layer is kept fixed at the optimum geometry calculated for bulk Fe.

The vibrational frequencies for free energy calculations are calculated by allowing the adsorbed molecules and the top 3 layers of Fe to relax, with the bottom two layers fixed. For these phonon calculations we used 10^{-6} eV energy convergence threshold to obtain reliable phonon frequencies (no negative eigenvalues.) To obtain the Free energy, G=H-TS, for the various equilibrium configurations, we used density functional perturbation theory (DFPT) to calculate the phonon density of states, which was used to calculate the ZPE, the temperature correction to the enthalpy, and the vibrational contributions to the entropy. An identical procedure was used for the transition states. We note that some of the frequencies correspond to hindered translational or rotational modes, for which the harmonic oscillator description is less accurate. In these cases, namely NH_3 and N_2 desorption calculations, we use ZPE corrections only. [32-34]

2.2.c Transition States

Transition state searches used the climbing image NEB method in the VASP-VTST code. [35] Here the initial and final states geometries were minimized first. Then three intermediate images were optimized, excluding initial and final images. An additional NEB climbing-image calculation was performed to obtain the final value of the barrier. The climbing NEB method generates a true transition state, as we confirmed by performing vibrational frequency calculations showing a single negative curvature in the Hessian. Dimer calculations [36-37] were performed whenever extra imaginary frequencies were found in the NEB transition state image.

2.2.d Surface sites

The adsorption sites for the various species H, N, NH, NH_2, NH_3 calculated here are consistent with previous experimental [38] and DFT results [39-41]. The Fe(111) surface has four types of adsorption sites: top (T), bridge (B), 3-fold-shallow (S), and 3-fold-deep (D), with top/shallow (TS), and top-Shallow-deep (TSD) intermediate sites, as shown in Figure 2-1.

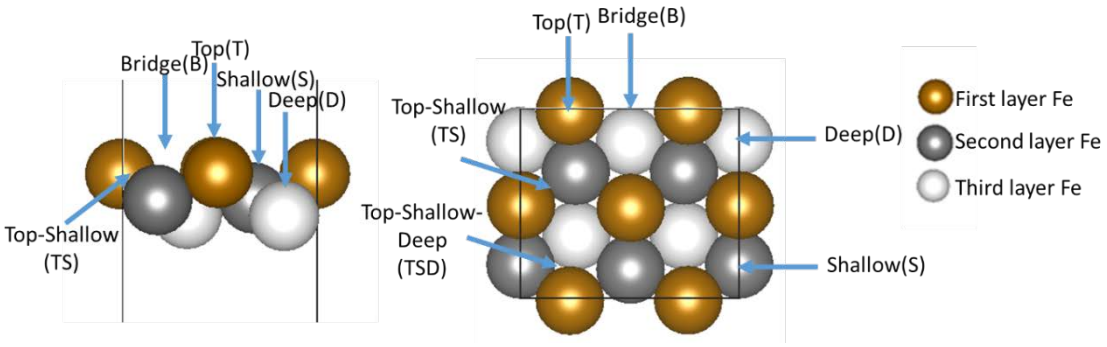

Figure 2-1. Structure of the Fe(111) surface with various surface adsorption sites noted. Bronze spheres represent the top layer, dark grey spheres represent the second layer, while white spheres are third layer Fe atoms. Multiple adsorption sites are labeled from both top and side views, including B, T, S, D, TS, and TSD sites. This figure shows only 3 of the 6 layers used in the calculations.

We find generally that

- H prefers the TS site between a top Fe and a 2nd layer Fe or the TSD site between Fe on all 3 layers
- N prefers the B site,
- NH prefers the BD site, with N sitting on the bridge(B) site, but NH pointing sideways toward the D site
- NH_2 prefers the TS site between a top Fe and a 2nd layer Fe.
- NH_3 prefers the T site.

but as shown below in Figure 2-3 occupation of other sites sometimes shifts the minima.

2. 3. Energy landscape. The most favorable pathways for converting $3H_2 + N_2$ to $2NH_3$, with illustrations for T=673°K and p=20atm

We carried out DFT calculations including various numbers of H, N, NH, NH_2, NH_3 molecules bound to the various stable sites for a 2x2 supercell of the (111) surface. For each combination of sites, we calculated the vibrational frequencies to obtain the free energy at

the operational temperature. Then we calculated the reaction barriers for the various reaction pathways. We then used these values to find reaction sequences with lowest overall free energy barrier for the full process of converting one N_2 and three H_2 to form two NH_3.

For a total pressure P=20 atm under stoichiometric conditions and T=673°K, we find that the lowest free energy for an equilibrium in which no reactions are allowed is the $3N\_NH_2$ configuration shown in Figure 2-2. Thus, prior to allowing reactions to proceed, the equilibrium condition on the Fe(111) surface in our 2x2 model would be predominantly the $3N\_NH_2$ configuration. We take the free energy of this state as our reference point, with G=0. However, as discussed in section 4, the steady state kinetic process producing NH_3 leads to different distributions of states that depend on the NH_3 pressure assumed for the steady state.

We examined the barriers between all the states connecting though reactions of N_2 and H_2 at various sites, leading finally to the energy landscape in Figure 2-2**,** involving 26 intermediates and leading to the lowest maximum barriers. We include in Figure 2-2 the states that we found to be important for the steady state kinetics as described in section 5. We confined our calculations to the 2x2 supercell.

The favorable path selected in Figure 2-2 includes the following transitions (all energies in eV)

1. $3N\_NH_2$ + $3H_2$gas+N_2gas; G=0 at T=673°K and p=20atm
2. =>$3N_NH_2$_2H (H_2gas➔ H* + H*) G=0.57, where we expect a barrier of 0.57 eV.
3. =>$3N_NH_3$_H (H* + NH_2*➔ NH_3*) G=0.30 and G†= 1.47
4. => 3N_H (NH_3*to NH_3gas) G= -0.26 and G†= 1.12
5. =>2N_NH (H*+N*➔NH*) G= 0.22 and G†= 0.66
6. =>2N_NH_2H (H_2gas➔ H* + H*) G=0.30, we calculate a barrier of 0.57 eV.
7. =>$2N_NH_2$_H (NH*+H*➔NH_2*) G= -0.39 and G†= 0.56, described in detail in transition state section.
8. =>$2N\_NH_3$ (NH_2*+H*➔NH_3*) G=0.39 and G†= 1.36, however, there is an alternative path from $2N_NH_2$_2H to $2N_NH_3$_H, with a lower barrier of G†= 1.13,

this will be further discussed in the kMC section. The resting state of this step is indeed 2N_NH_2_H, with G = -0.39, together making this barrier 1.13+0.39 = 1.52 in kMC.

9. =>2N (NH_3*to NH_3gas) G=0.11 and G†= 1.40 Similar with the previous step, there is an alternative path from 2N_NH_3_H => 2N_H, with a lower barrier of G†= 1.03. Similarly, the resting state is 2N_NH_2_H, with G = -0.39, together making this barrier 0.39+1.03 = 1.42 in kMC. These alternative paths are shown in Figure 2-2 using green color.
10. => 2N_N_2(N_2gas➔N2*triple bonded, top layer) G= 0.20. This step involves N_2 adsorption (G†= 0.94) and its resting state is 2N_2H (edge configuration, see the SI) with G = -0.63, together making this barrier 0.94+0.63 = 1.57 in kMC.
11. => 4N(N_2*➔N*+N*) G= -1.10 and G†= 0.64 is the highest barrier along N_2 dissociation, see Figure S2-4.
12. => 3N_NH_H (H*+ N*➔ NH*) G= -0.65 and G†= -0.07
13. =>3N_NH_2 (NH*+H*➔NH_2* to complete the cycle).

    The above states are described by a simple linear energy landscape in Figure 2-2, confined in a 2x2 cell. However, we have also included the most populated states involved in the steady state kMC calculations, such as 2N_H and 2N_2H.

14. 3N_NH_3 => 3N (NH_3*to NH_3gas), G from 0.30 => 0.41, and G†= 1.34
15. 2N_NH_2_2H =>2N_NH_3_H (NH_2*+ H*➔ NH_3*), G from -0.27 => 0.01, and G†= 1.13
16. 2N_NH_3_H => 2N_H (NH_3*to NH_3gas), G from 0.01 => -0.22, and G†= 1.03
17. 2N_H => 2N, G from -0.22 => 0.11
18. 2N => 2N_2H, G from 0.11 => -0.63

In this simplified scheme we considered dissociative chemisorption of H_2gas to H* + H* explicitly only for the step 2N + H_2gas to 2N_2H. This step is closest to the dissociative

chemisorption of N_2gas to N* + N* that in Section 5 we single out as the RDS in our kinetic model. We find that NH_3 production rate changes from 17.7 sec^{-1} per 2x2 site to TOF 17.5 sec^{-1} if we use the calculated barrier of 0.57 eV instead of setting the barrier to zero. For other steps we assume H_2 dissociative chemisorption to have barrier that's small enough to not affect kinetics. And we form successive NH_x species by the Langmuir-Hinshelwood (LH) mechanisms: NH_x*+H*➔ NH_{x+1}* (for PBE_D3, step 12 LH is small enough, and not rate determining. Thus, we don't consider ER further).

The highest-energy transition states in the free energy landscape are, in decreasing order:

- TS3: step 3 with G†=1.47 eV involves H* + NH_2* => NH_3*, an LH mechanism. The detailed transition state structure is shown in Figure S2-3(b) of the SI.
- TS 8: step 8 with G†=1.13 eV involves H* + NH_2* => NH_3*, an LH mechanism. The detailed transition state structure is shown in Figure S2-3(a) of the SI.
- TS4: step 4 with G†=1.12 eV involves NH_3* => NH_3 gas, just as in step 9. We used electronic adsorption energy of NH3 with ZPE correction as the desorption barrier.
- TS9: step 9 with G†=1.03 eV involves NH_3* => NH_3 gas, shown in the green path of Figure 2-2. Here, we considered the alternative pathway of desorption NH_3 from 2N_NH_3_H. We used electronic adsorption energy of NH_3 with ZPE correction as the desorption barrier.
- TS10: step 10 with G†=0.94 eV, we included N_2 adsorption into consideration, and used the electronic adsorption energy together with ZPE as the desorption barrier, and this leads to G†=0.94 eV.
- TS5: step 5 with G†=0.66 eV involves H* + N* => NH*, an LH mechanism. The NEB energy and structures are shown in Figure S2-2(a) of the SI. This is the lowest energy barrier for adding an H to NHx. We also examined 3N_H + H_2(gas) => 2N_NH_2H in which gas phase H_2 adds to N* to form NH* + H*, This involves a high energy intermediate state with G= 1.78eV, so we will not consider this step further.
- TS 11: step 11 with G†= 0.64 eV. We took consideration of N_2 dissociation.

a) the initial bonding of N_2 retains the triple-bond while making a sigma bond to an on-top site on the first layer (denoted σ N≡N-T phase, where ≡ in the middle represents the bond order, and T represents adsorption on top layer, or Nørskov γ)
b) there is a barrier to moving to a sigma bond to an on-top site on the second layer (denoted σN≡N-S, where S represents adsorption on second layer, or Nørskov δ)
c) There is a barrier for one π bond of N_2 to bind to two surface Fe atoms (denoted as πN=N-η_2 or Nørskov α)
d) There is a barrier for the 2nd π bond of N_2 to 4N, with the N-N bonding to three surface Fe atoms (denoted as 2πN-Nη_3 or Nørskov α')
e) Finally, there is a barrier for the remaining N-N bond to dissociate with each N bonding to 4 surface atoms (denoted as Nørskov β phase), leading to the 4N state. The NEB energy and structures for N_2 dissociation are shown in Figure S2-4 of the SI.

- TS7: step 7 with G†=0.56 eV involves H* + NH*➔ NH_2*, an LH mechanism. The NEB energy and structures are shown in Figure S2-2(b) of the SI.
- TS12: step 12 with G†=-0.07 eV is an LH mechanism in which H*+N*=> NH*
- State 13. This is the same as the state 1 but the G=-1.22 eV because we have produced two NH_3 from $3H_2$ +N_2. Similarly, state 11 has G=-1.10 because we already have produced two NH_3 along the pathway.

The energy landscape is plotted in Figure 2-2 for the Somorjai experimental conditions of 673°K and 20 atm of total pressure (H_2 and N_2 in stoichiometric ratio and NH_3 pressure = 1.5 torr)[13]. The lowest free energy state 3N_NH_2 is taken as reference, setting G=0.

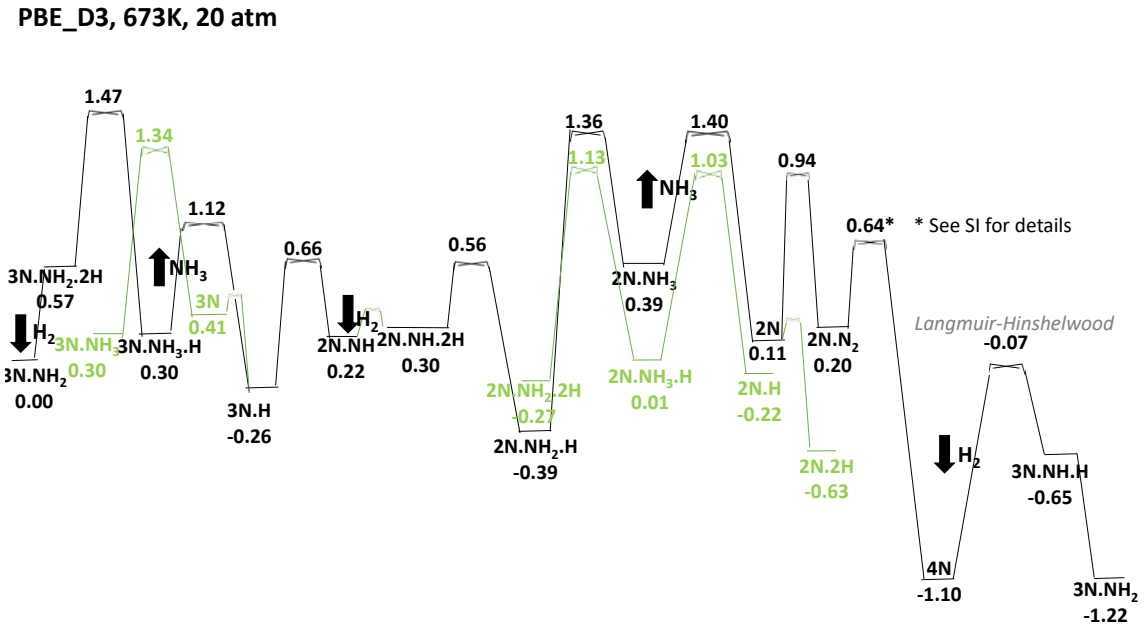

Figure 2-2. Energy landscape for NH_3 synthesis reactions under Somorjai condition, 673°K, 20atm. The lowest energy state 3N_NH_2 is taken as reference, with a free energy of zero. We considered the linear pathway in black and proposed alternative pathway in green, in order to obtain the optimum barriers.

NH_3 production rate is dominated by 3 steps:

1). N_2 dissociation and desorption,

2). hydrogenation of NH_2, and

3). NH_3 desorption.

This diagram considers the reaction of 3 H_2 plus 1 N_2 to form 2 NH_3, so that the total free energy decreases by 1.22 eV as we go from 3N_NH_2 on the left to 3N_NH_2 on the right. The free energy diagram with same states calculated at PBE level can be found in Figure S2-1.

The simplified reaction pathway described above is illustrated pictorially in Figure 2-3 showing the surface structure step by step, to clarify the nature of each adsorption site and the interactions between these adsorbed species.

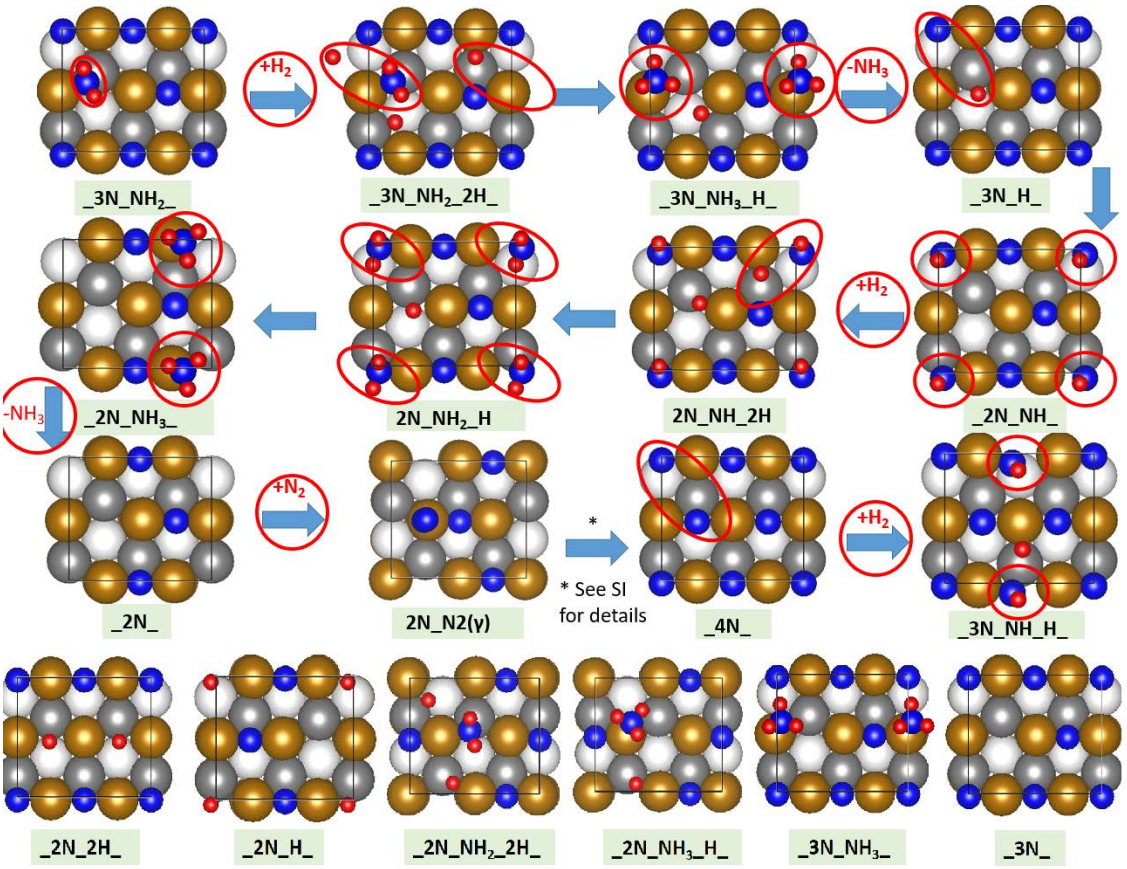

Figure 2-3. Surface structure for selected reaction steps in Figure 2-2. Bronze spheres represent first layer Fe atoms, Dark gray represents second layer Fe atoms, and white represents third layer Fe atoms. Nitrogen atoms are shown using navy blue spheres, and hydrogen atoms are shown using red spheres. Every intermediate structure is geometrically optimized with the results summarized in Figure 2-3 to illustrate the adsorption sites for various species, and interaction between these adsorbed species. Note that in cases where species are at the edges, we show all images that map onto the 2x2 cell. In cases where a circle is used to highlight the reactive species at an edge we show the other equivalent circles.

Transition state geometries are shown in Figure S2-2 through S2-4. We considered five reactions:

A. 3N_H =>2N_NH, migration of hydrogen and addition to N on the surface (LH);
B. 2N_NH_2H => 2N_NH_2_H, hydrogen migration and addition to NH on the surface (LH);

C. $3N\_NH_2\_2H$ => $3N\_NH_3\_H$, hydrogen migration and addition to NH_2 on the surface (LH);
D. $2N\_NH_2\_2H$ => $2N\_NH_3\_H$, hydrogen migration and addition to NH_2 on the surface (LH);
E. $2N\_N_2$ => 4N. This involves a complex pathway from triple-bonded N_2 adsorbed on first layer ($\sigma N\equiv N$-T or γ) => triple-bonded N_2 adsorbed on second layer ($\sigma N\equiv N$-S or δ) => double-bonded N_2 to a bridge site ($\pi N=N\eta_2$ or α) => single-bonded N_2 at a 3-fold site ($2\pi N\text{-}N\eta_3$ or α') => the dissociated state 4N(β).

2.4. Discussion of the wavefunctions

Since Fe is ferromagnetic, we analyzed the magnetic moments of the various atoms and the changes in the key steps of ammonia synthesis. Total magnetic moments for all the states along the pathway can be found in Table 2-1.

Name	Total Mag(uB)	dMAG	Covalent bond to Fe	Ratio	#Comment	#Comment
111_surface_24Fe	64.76	0.00	0			2.70 per Fe
$3N.NH_2$	57.10	-7.66	10	77%	3*3+1	
$3N.NH_2.2H$	56.49	-8.26	12	69%	3*3+1+2	0.3 per H
$TS\_3N.NH_2.2H$	55.94	-8.82				
$3N.NH_3.H$	56.33	-8.43	10	84%	3*3+1	
$3N.H+NH_3(g)$	57.00	-7.75	10	78%	3*3+1	
$TS\_3N.H+NH_3(g)$	57.54	-7.22				
$2N.NH+NH_3(g)$	58.17	-6.59	8	82%	3*2+2	
$2N.NH.2H+NH_3(g)$	57.27	-7.48	10	75%	3*2+2+2	
$TS\_2N.2H.NH+NH_3(g)$	58.80	-5.96				
$2N.NH2.H+NH_3(g)$	59.35	-5.40	8	68%	3*2+1+1	
$TS\_2N.H.NH2+NH_3(g)$	59.08	-5.67				
$2N.NH_3+NH_3(g)$	59.45	-5.30	6	88%	3*2	
$2N\_diagonal.NH_2.2H$	58.32	-6.44	9	72%	2*3+1+2	
$TS\_2N\_diagonal.NH_2.2H$	58.64	-6.12				
$2N\_diagonal.NH_3.H$	59.08	-5.68	7	81%	2*3+1	2.84 per N

2N+2NH_3(g)	59.83	-4.93	6	82%	3*2	
2N.N2(σN≡N-T)+2NH_3(g)	58.83	-5.92	6	99%	3*2	No N2 to Fe
TS(σN≡N-T => σN≡N-S)	59.21	-5.54				
2N.N2(σN≡N-S)+2NH_3(g)	58.51	-5.54	6	92%	3*2	No N2 to Fe
TS(σN≡N-S => πN=N)	58.37	-6.38				
2N.N2(πN=N)+2NH_3(g)	58.65	-6.11	8	76%	3*2+2	2 new N-Fe
TS(πN=N=>2πN-N)	58.53	-6.23				
2N_N2(2πN-N)+2NH_3(g)	58.17	-6.59	10	66%	3*2+4	4 new N-Fe
TS(2πN-N =>N+N)	57.36	-7.39			8	
4N+2NH_3(g)	54.77	-9.98	12	83%	3*4	2.50 per N
4N.2H+2NH_3(g)	54.32	-10.44	14	75%	3*4+2	
TS_4N.H2	55.40	-9.35				
3N.NH.H+2NH_3(g)	55.92	-8.84	12	74%	3*3+2+1	
3N.NH_2+2NH_3(g)	57.10	-7.66	10	77%	3*3+1	
Average in covalent character				77%		

Table 2-1. Analysis of change in spin along the pathway. Total magnetic moment for each state and the change with respect to pure Fe are reported. Covalent bond calculated using simple VB theory is presented in covalent bond column, and we assume each adsorbed N, NH, NH_2, NH_3, H to decrease spin moment 3, 2, 1, 0, 1 respectively.

We observe non-negligible changes in these moments along the reaction pathways.

In earlier studies of hydrocarbon intermediates on the metals Ru, Rh, Pd, Os, Ir, Pt, Kua and Goddard proposed a Valence Bond (VB) model in which alkyl, alkylidene, and alkylidyne intermediates to a metal surface are considered to make 1, 2, or 3 valence bonds to the metal surface and showed that this correlates well with bond energies and other properties.[42-45] We propose a similar valence bond (VB) model to understand the spin changes in spin for Figure 2-4(a) and SI table 2-2. We assume that each of the unpaired spins of N atom makes a covalent bond to an unpaired spin on the neighboring Fe atoms, reducing the spin by 3 units. Indeed, for the 4N state the spin of the cluster is reduced by 10.51 or 2.63 spins per N. We will also assume that the two unpaired spins of NH can make two bonds, which should reduce

the Fe spin by 2 units and NH_2 can make one bond, which should reduce it by 1 unit as should H.

From table 2-1, we see that the net spin changes observed in the 14 states that are not TS, average 77% of the expected value for this model, supporting this simple Valence Bond view of bonding. Of course a more complete analysis should consider the ligand field splitting to these unpaired spins and the orbital requirements to form a covalent bond from the Fe d-orbitals to the N p-orbitals, but we think that the simple VB view accounts for the major spin coupling effects.

These changes in magnetic moment suggests an important role for spin in the reactions, which suggests that engineering the spin of surface atom may provide a new way to increase Haber Bosch reaction efficiency. This suggests designing new catalysts that have different spin character, e.g., Co, Ni, Mn, or Cr all of which can exhibit localized spins, or Ru or Os which should not have large spins. Also the changes in the oxidation state of the atoms reported in Figure 2-4(b) are noteworthy and analogously suggest an important concomitant effect of charge transfer effects.

2.5. Kinetic modelling results with illustrations for T=673°K and p=20atm

2.5.a. Kinetic Monte Carlo Simulations

The free energies in Figure 2-2 provide a crude estimate for the rate. Here we might estimate the rate from transition state theory (TST) as $k=(k_BT/h)\exp[-1.57/k_BT] = 24\ sec^{-1}$, leading (after multiplication by a factor of 2 due to the presence of 2 reaction sites in the unit cell) to a TOF of 48 NH_3 molecules per second per (2x2) unit cell.

However, for such a complex mechanism, it is necessary to go beyond this rough estimate with simulations that include all distributions of the states involved and the rates between them in a full kMC model, allowing the system to achieve steady state. We evaluated each rate using transition state theory as $(k_BT/h)\exp(-\Delta G\dagger/k_BT)$, where $\Delta G\dagger$ is the difference in free energy between the starting state and the saddle point. In the case of ER reactions involving gas-phase species turning into adsorbates, we again use transition state theory, but

for the reverse LH process, and then we invoke microscopic reversibility principle to calculate the rate of the direct process.

This system is not in equilibrium. To consider the kinetics of the system in steady state, we carried out kMC calculations as discussed below. In this case we find that the state 2N_2H has the lowest ΔG under steady-state conditions at $P(H_2)$=15 atm, $P(N_2)$=5 atm, $P(NH_3)$= 1.5 torr, T = 673 °K, and the free-energy difference between this state and the highest point ΔG† along the reaction path is 1.57 eV. Taking into consideration the states important in the kMC calculations and varying NH_3 pressure leads to the diagram in Figure 2-4.

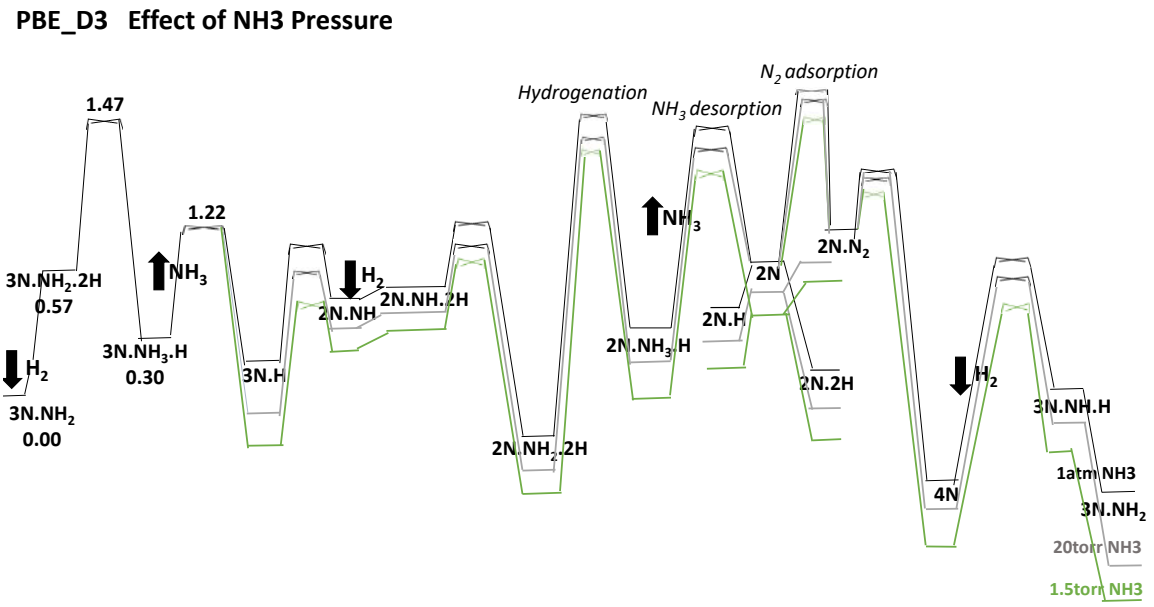

Figure 2-4. Illustration of how the equilibrium energy landscape from Figure 2-2 becomes modified for steady state kinetics of forming NH_3 at different pressures from 15 atm of H_2 and 5 atm of N_2 at 673°K (Somorjai conditions). We show the results for three pressures of NH_3 product: 1.5 torr, 20 torr, and 1 atm. Barriers in green are assumed to be fast and assigned rates of 10^{11} s^{-1}. The populations are shown in Table 2-2. We see here that NH_3 acts as a poison, decreasing the TOF from 17.7 at 1.5 torr, to 16.5 at 20 torr, to 2.8 at 1 atm.

In the Somorjai et al[13] papers, the measured ammonia production at 673 °K and 15 atm H_2, 5 atm N_2, extrapolated to zero ammonia pressure is 2.8 x 10^9 NH_3 moles/cm^2/sec which corresponds to 9.7 NH_3 molecules produced per second on a (2x2) unit cell.

We conducted kMC simulations at T = 673 °K and pressures: pH_2=15atm, pN_2=5atm and pNH_3= 1.5 torr. We used 20 independent replicas and 2 x 10^9 kMC steps each (checking that the results converged within 5% with respect to a test case using 100 replicas and 2 x 10^{10} kMC steps) for a total simulated time of 2733 sec. This leads to production of 48482 NH_3 molecules produced by our (2x2) unit cell, corresponding to a **predicted TOF= 17.7 NH_3 molecules per second per (2x2) site, in good agreement with the experimentally measured TOF of 9.7** (our predicted rate should be higher than experiment since our surface is perfect). We should caution here that the final TOF is very sensitive to the key barriers at the RDS. Thus to change the 17.7 to 9.7 we need only increase the free energy of the transition state for the 10th step from 0.94 eV to 0.98 eV.

As shown in the SI, exactly the same set of calculations at the PBE level without D3 find TOF=89.3 compared to 17.7 for PBE-D3 and 9.7 experiment. This indicates that for this system PBE-D3 provides better accuracy than pure PBE. However, the rate for the PBE level would match experiment by changing the barrier for the 3rd step from 1.47 eV to 1.64 eV. Of course the real accuracy depends on that for quite a number of individual steps.

The steady-state apparent ΔG (i.e., the logarithm of the relative populations) for the most important states are reported in Table 2-2, which shows that the processes before and after the ammonia desorption are not far from equilibrium. That is, the populations are not far from those expected on the basis of their equilibrium ΔG according to the Boltzmann distribution (the percent of residence times is also shown), except for the irreversible ammonia desorption steps.

If instead of NH_3= 1.5 torr, we use NH_3=1 atm, shown in Figure 2-5, the total rate from the kMC is 2.8 NH_3 molecules per second per (2x2) site. Thus NH_3 is a poison. Somorjai et al does not report the dependence of TOF on NH_3 pressure for the (111), but they do report it for Fe(100)[14]:

- for 20 torr pressure of NH_3, TOF=0.21 NH_3-molecules/sec/(2x2)
- for 1.5 torr pressure of NH_3, TOF=1.1 NH_3-molecules/sec/(2x2)
- extrapolating to zero NH_3 pressure, leads to TOF= 1.5 NH_3-molecules/sec/(2x2).

Thus the experimental poisoning effect of NH_3 on (100) is similar to what we predict for (111).

Analogous kMC simulations at T = 730 °K and pressures: pH_2=15atm, pN_2=5atm and pNH_3= 1.5 torr give a TOF = 83.3 NH_3 molecules per second per (2x2) site which is still in reasonable agreement with the experimentally measured TOF of 22.8 from Figure 13 of Ref.[13] In conclusion, we find that hydrogenation of NH_2, NH_3 desorption, H_2 poisoning, and N_2 desorption can be rate determining depending on the reaction conditions, while previous work on Fe-catalysts emphasized on N_2 dissociation being the sole rate determining step.[12]

2.5.b. Rates for typical Haber Bosch conditions: T=723°K and p=200atm

The Haber-Bosch (HB) industrial process is conducted under a range of temperatures and pressures, with typical temperatures in the range 450-550 °C and total pressure around ~200 atm with a stoichiometric ratio of N_2 and H_2. To compare our predictions with industrial conditions, we choose T = 730 °K and two sets of pressures: (pH_2=150 atm, pN_2=50 atm, pNH_3= 1 atm), and (pH_2=120 atm, pN_2=40 atm, pNH_3= 20 atm), corresponding approximately to conditions holding at the beginning and the end of the HB process. For comparison, we also add that at pNH_3= 1.5 torr Figure 2-2 becomes Figure S2-6 of the SI leading to a naïve TOF= 258 (or 516 after multiplying by a factor of 2), which is about 5 times what we predict for Somorjai conditions using the same rough formula.

Running kMC simulations under these two conditions leads to NH_3 production rates of 93.7 NH_3-molecules/sec/(2x2) at pNH_3= 1 atm, and 18.5 NH_3-molecules/sec/(2x2) at pNH_3= 20 atm, respectively. Free energy differences due to populations and thermodynamic free energy differences for various states are shown in Table 2-2.

	T=673, pH_2=15, pN_2=5, pNH_3=1.5/760			T=730, pH_2=150, pN_2=50, pNH_3= 1			T=730, pH_2=120, pN_2=40, pNH_3=20		
configuration	t_i (%)	$-\ln(P_i/P_0)$	ΔG	t_i (%)	$-\ln(P_i/P_0)$	ΔG	t_i (%)	$-\ln(P_i/P_0)$	ΔG
3N_NH_2	6.5	0.00	0.00	1.4	0.00	0.00	7.2	0.00	0.00
3N_NH_2_2H	3E-4	0.57	0.57	5E-4	0.50	0.49	2E-3	0.51	0.51
3N_NH_3_H	6E-4	0.54	0.30	0.003	0.38	0.21	0.19	0.23	0.23
3N_H	1.1	0.10	-0.26	0.32	0.09	-0.08	1.2	0.11	0.11
2N_NH	6E-4	0.54	0.22	3E-4	0.52	0.39	1E-3	0.54	0.59
2N_NH_2H	1E-4	0.63	0.30	3E-4	0.53	0.36	8E-4	0.57	0.61
2N_NH_2_H	20.	-0.07	-0.39	21.7	-0.17	-0.31	64.5	-0.14	-0.09
2N_NH_3	5E-5	0.69	0.39	8E-5	0.61	0.47	4E-4	0.61	0.68
2N	2E-4	0.61	0.11	1E-3	0.62	0.47	2E-5	0.82	0.88
4N	0.22	0.20	-1.10	2E-2	0.28	-0.80	0.092	0.27	-0.80
3N_NH_H	4E-3	0.57	-0.65	1E-4	0.57	-0.43	8E-4	0.57	-0.41
2N_2H_lin	53.6	-0.12	-0.63	61.1	-0.24	-0.41	11.4	-0.03	0.02
2N_2H	16.9	-0.06	-0.56	10.4	-0.13	-0.24	1.96	0.08	0.19
2N_NH_3_H	3E-3	0.45	0.24	5E-2	0.21	0.05	0.19	0.23	0.26
2N_H	5E-2	0.29	-0.22	2E-2	0.25	0.10	5E-3	0.46	0.52
2N_NH2_2H	1.6	0.08	-0.30	5.0	-0.08	-0.22	13.2	-0.04	0.03
kMC **theory** NH_3 mol/s/(2x2)	17.7			93.7			18.6		
Experiment [13] NH_3 mol/s/(2x2)	9.7			N/A			N/A		
total NH_3mol	48482			33764			2529		
3N_NH_3_H ↔ 3N_H	24262			16801			1284		
2N_NH_3_H ↔ 2N_H	24220			16963			1245		

Table 2-2. kMC result. Top rows – Per cent of populations (i.e., residence times) = t_i(%), apparent free energy differences [evaluated as minus the logarithm of ratio of populations =

P_i/P_0, where $P_0 = P_{3N\_NH2}$], and thermodynamic free energy differences (ΔG) for selected configurations in a Fe(111)-(2x2) unit cell under steady-state of ammonia synthesis as predicted by kMC simulations at different temperatures (673 and 730 K), and different H_2, N_2, NH_3 pressures using data from DFT/PBE-D3. All configurations are assumed in the zig-zag arrangement, except for "2N_2H_lin" which is linear (see SI for details). Temperature in Kelvin, pressure in atmospheres, free energy differences in eV. Bottom rows – NH_3 molecules produced per second per (2x2) unit cell under the given conditions [NH_3mol/s/(2x2) : the conversion factor to moles per second per cm^2 in ref[13] is 3 x 10^{-10}], total number of NH_3 molecules produced in the kMC runs (total NH_3mol), further partitioned into the 2 main steps involving NH_3 adsorption/desorption: $3N\_NH_3\_H \leftrightarrow 3N\_H$; $2N\_NH_3\_H \leftrightarrow 2N\_H$.

2.6. Comparison with previous literature

2.6.a Comparison with experiment

In the above discussions we compared our predicted TOF with the single crystal experimental values (Somorjai), finding excellent agreement.

Another comparison in with experiment is to Temperature Programmed Desorption (TPD) in which a monolayer (ML) of NH_3 at low temperature is heated at a uniform rate dT/dt and the products measured with a mass spectrometer. Here the temperature for the peak desorption rate, TPD peak, combined with dT/dt in the Redhead equation gives a crude estimate of the binding energy. Our predicted binding energies are consistent with available experimental literature. Thus, Figure 9 of Strongin et al [13] reports TPD experiments on Fe(111) with a very broad desorption peak centered at about 300 °K for a heating rate of 8 °K/sec, which corresponds to an activation barrier for desorption of 0.82 eV. This compares well with the values of 0.89 to 1.00 eV we calculate for the NH_3 desorption barrier.

Our results are also consistent with experiments conducted on polycrystalline Fe wires by Ertl and Huber[46-47] At T = 673 °K our barriers for NHx dehydrogenation mechanisms (NHx $\rightarrow$NHx-1 + H) range from 0.53 to 0.63 eV which are lower than the barrier for NH_3

desorption (0.76 to 0.87 eV) which in turn are lower than the barrier for both N_2 dissociation (1.27 eV) and for N-adatom recombination (2.04 eV). Our predicted NH_3 sticking coefficient at 673 °K and a NH_3 pressure of 5×10^{-6} torr is about 5 times larger than the N-adatom recombination rate (the kinetic constant corresponding to our 2.04 eV barrier is 0.03 sec-1), which should be contrasted with a near equality at T > 640 °K in previous study. However, the Ertl experiments were on Fe polycrystalline wires in which the presence of (100) and (110) facets may increase the ratio of N-adatom recombination over the NH_3 dissociative sticking rate. Indeed the experimentally derived value of 45±5 kcal/mol for the activation free energy of N-adatom recombination in literature is only slightly lower than our predicted value of 47 kcal/mol (2.04 eV). Our value is also slightly lower than the experimental value of 51 kcal/mol reported on Fe(111) by Bozso et al. [48] (At 1 torr NH_3 we predict an adsorption kinetic constant of 3×10^4 on the 2N site.)

Another TPD experiment on industrial catalysts [49] observed a N_2 desorption peak at 644 °K, with an estimated N-adatom recombination rate of 1-2 x 10^9 x exp(- 146 kJ/mol/RT). This rate corresponds to an apparent free energy barrier at 644 °K of ΔG = 2.00 to 2.04 eV, which is very close to our predicted barrier of 2.04 eV at T = 673 °K, especially considering that the industrial catalyst is K-promoted and hence is expected to exhibit a smaller barrier. In the same work, the N-adatom coverage under Haber-Bosch reaction conditions was estimated to be 0.4 of the maximum N-adatom coverage under N_2+$3H_2$ conditions, a value close to our predicted value of 0.5 for the 2N.xH configurations predominant on the (2x2) unit cell.

2.6.b Comparison with theory

The pioneering QM study for Haber Bosch chemistry on Fe(111) was reported in 1999 by Nørskov et al[50].They investigated in detail several states with N_2 molecularly adsorbed and/or dissociated and considered simplified pathways for dissociation. Their qualitative picture considers N_2 dissociation as the RDS, which we have shown to be correct with our detailed reaction kinetics based on QM free energies and reaction barriers. However, there are significant quantitative differences because we calculated reaction barriers, whereas they examined only stable species. Instead they made estimates using the Ulitsky-Elber

approximation to find minimum energy paths. In contrast we used fully relaxed NEB techniques. In addition Nørskov et.al [50] used the rev-PBE xc-functional without dispersion corrections (dispersion corrections increase adsorption energies by ~ 10 %). They used a slab with 7 layers apparently relaxed without constraints (compared to 6 in ours), but with a very small (1x1) unit cell or sometimes sqrt(3) x sqrt(3), rather than the 2x2 used in our studies. Also entropic corrections to free energies were not included in their calculations.

Nørskov et al.[50] considered dissociatively chemisorbed binding energies for N_2 and described several states labeled as α, α', δ, β, γ. We used PBE-D3 to calculate the binding energies for these states with the results in table S2-1 of the SI. We found much stronger binding for both horizontally and vertically chemisorbed N_2 states α, α', δ, β, due to a better description of dispersion correction. We also found that N_2 adsorption states have a very sensitive adsorption energy dependence with respect to the surface's N atom coverage. State α is better in electronic energy of ~0.2 eV than α' on bare surface, however, with 2N present on the surface, the result is reversed and state α' is better in energy than α by ~0.2 eV. We arrived at similar result for dissociated N atom.

However, despite some differences in the specific numbers, we confirmed the Nørskov overall pathway for dissociate chemisorption of N_2. Triple-bonded N_2 adsorbed on first layer (γ) => triple-bonded N_2 adsorbed on second layer (δ) => double-bonded N_2 bonded to a bridging site (α) => single-bonded N_2 bonded to a three-fold site (α') => dissociated N atoms (β). The biggest difference is that our calculations have two other N already bonded to 4-fold sites, which changes the overall energetics and barriers.

A more recent QM study on adsorption and dissociation of NH_3 molecule on Fe(111) by Lin et.al [41] provided comprehensive adsorption energy data for several species, including N, H, NH, NH_2, and NH_3. They used a revised Perdew-Burke-Ernzerhof (GGA-rPBE) exchange correlation functional, without dispersion corrections. They used a (3x3) unit cell, compared to our (2x2) cell. They calculated QM barriers but did not calculate the activation free energies for reactions**.** The influence of coverage on adsorption energy was not considered, nor were entropic corrections to free energies calculated. Their results in kcal/mol, are converted to eV in table S2-2 of the SI. This study by Lin et.al [41] leads to better agreement

for binding of N, NH, NH_2 (after correcting for the difference in surface coverage). It is expected that their adsorption energies would be ~ 30 % too weak due to the lack of D3 dispersion corrections.

2.7. Summary and conclusions

We report here the first comprehensive study of the mechanisms underlying NH_3 synthesis by Fe based catalysts including the reaction barriers for all 17 steps involved and considering both Langmuir-Hinshelwood (surface species reacting with surface species) and Eley-Rideal (gas phase species reacting with surface species) processes.

The QM was at the level of PBE including D3 London dispersion (van der Waals attraction) corrections that was previously applied successfully to the oxygen reduction reaction (O_2 + protons ➔ H_2O) on Pt and the CO_2 and CO reduction reactions on Cu surfaces.[17–21,23–25]

Correcting the DFT for phonons to get free energies at experimental reaction conditions, and carrying out extensive kinetic Monte Carlo calculations to obtain the steady state populations at the conditions of the single crystal experiments (673°K , 15 atm H_2, 5 atm N_2, and 1.5 torr NH_3) leads to a **predicted TOF=17.7 sec-1** per 2x2 Fe(111) surface site, in excellent agreement with the single crystal **experimental rate of TOF= 9.7 sec-1 per site**. This suggests that the accuracy of PBE-D3 for the critical barriers may be of the order of 0.04 eV.

This overall agreement in the predicted TOF with experiment indicates that the QM combined with kMC provides a new detailed understanding of the reaction mechanism underlying NH_3 synthesis. This should provide a basis for considering how to modify the catalyst to improved performance. In particular, the changes in the spins and charges in the TS provides hints, as discussed above of considering alloying with metals having localized spins, such as Cr, Mn, Co, or Ni, or with metals not expected to have localized spins such as Ru or Os.

Despite the excellent agreement, we should caution that the experiments might have been affected by impurities such as O that might affect the rates. Also the QM calculations using the phonons to predict free energies at reaction conditions might miss dynamical and

anharmonic effects that would require quantum based reaction dynamics. Moreover, the limitation to a 2x2 unit cell may eliminate some reactions that could require larger unit cells. In addition, replacing the PBE level of DFT might be important for a system such as this with localized spins and the origin of the D3 corrections for London dispersion is suspect.

Associated content

Supporting Information. Energy landscape and kinetic Monte Carlo results for Haber Bosch reaction at PBE level; transition state geometry and potential energy curves for key processes; pictorial illustration of “linear” and “zig-zag” configurations; comparison with previous theory results; detailed instructions on the use of the excel file with full numerical data (PDF). Numerical data of electronic energies and free energies for surface configurations using PBE-D3 and PBE xc-functionals at 673 °K and 730 °K, thermodynamic data for gas-phase molecules, and reaction energy barriers for key processes, reported in a 4-sheet excel file (XLSX) in Appendix A.

Acknowledgements

This work was supported by the U.S. Department of Energy (USDOE), Office of Energy Efficiency and Renewable Energy (EERE), Advanced Manufacturing Office Next Generation R&D Projects under contract no. DE-AC07-05ID14517 (program manager Dickson Ozokwelu, in collaboration with Idaho National Labs, Rebecca Fushimi). This project was initiated with modest support from the U.S. Department of Energy's Advanced Research Projects Agency-Energy (ARPA-E) under contract number DE-AR0000552 (Patrick McGrath) aimed at examining novel methods for accelerating catalytic reactions.
A.F. gratefully acknowledges financial support from a Short-Term Mission (STM) funded by ItalianConsiglio Nazionale delle Ricerche (CNR).

We thank Dr. Tao Cheng for help with the ER reaction for N_2 dissociation.

Many of the calculations were carried out on a GPU-cluster provided by DURIP (Cliff Bedford, program manager). This work used the Extreme Science and Engineering Discovery Environment (XSEDE), which is supported by National Science Foundation grant number ACI-1548562.

BIBLIOGRAPHY

(1) Erisman, Jan Willem, Mark A. Sutton, James Galloway, Zbigniew Klimont, and Wilfried Winiwarter. "How a century of ammonia synthesis changed the world." *Nature Geoscience* 1, no. 10 (2008): 636.

(2) Schlögl, Robert. "Catalytic Synthesis of Ammonia—A "Never-Ending Story"?." *Angewandte Chemie International Edition* 42, no. 18 (2003): 2004-2008.

(3) Mittasch, Alwin, and W. Frankenburg. "Early studies of multicomponent catalysts." In *Advances in catalysis*, vol. 2, pp. 81-104. Academic Press, 1950.

(4) Hara, Michikazu, Masaaki Kitano, and Hideo Hosono. "Ru-loaded C12A7: e–electride as a catalyst for ammonia synthesis." *ACS Catalysis* 7, no. 4 (2017): 2313-2324. (5) Nielsen, A. *Ammonia: Catalysis and Manufacture*; Springer: Heidelberg, 1995.

(6) Hellman, A., K. Honkala, I. N. Remediakis, A. Logadottir, A. Carlsson, S. Dahl, Christina Hviid Christensen, and Jens Kehlet Nørskov. "Ammonia synthesis and decomposition on a Ru-based catalyst modeled by first-principles." *Surface Science* 603, no. 10-12 (2009): 1731-1739.

(7) Kitano, Masaaki, Shinji Kanbara, Yasunori Inoue, Navaratnarajah Kuganathan, Peter V. Sushko, Toshiharu Yokoyama, Michikazu Hara, and Hideo Hosono. "Electride support boosts nitrogen dissociation over ruthenium catalyst and shifts the bottleneck in ammonia synthesis." *Nature communications* 6 (2015): 6731.

(8) Rossetti, Ilenia, Nicola Pernicone, and Lucio Forni. "Promoters effect in Ru/C ammonia synthesis catalyst." *Applied Catalysis A: General* 208, no. 1-2 (2001): 271-278.

(9) Akinfieva, T. A. "Establishing an MPEL for ruthenium dioxide in the air of a work area." *Gigiena truda i professional'nye zabolevaniia* 1 (1981): 46-47..

(10) Jennings, J. Richard, ed. *Catalytic ammonia synthesis: fundamentals and practice*. Springer Science & Business Media, 2013.

(11) King, David Anthony, ed. *The chemical physics of solid surfaces and heterogeneous catalysis*. Vol. 5. Elsevier, 2012.

(12) Ertl, Gerhard, Helmut Knözinger, and Jens Weitkamp, eds. *Preparation of solid catalysts*. John Wiley & Sons, 2008.

(13) Somorjai, Gabor A., and N. Materer. "Surface structures in ammonia synthesis." *Topics in Catalysis* 1, no. 3-4 (1994): 215-231.

(14) Strongin, D. R. "The importance of C7 sites and surface roughness in the ammonia synthesis reaction over iron." (1986).

(15) Johnson, Erin R., and Axel D. Becke. "A post-Hartree-Fock model of intermolecular interactions: Inclusion of higher-order corrections." *The Journal of chemical physics* 124, no. 17 (2006): 174104.

(16) Grimme, Stefan, Jens Antony, Stephan Ehrlich, and Helge Krieg. "A consistent and accurate ab initio parametrization of density functional dispersion correction (DFT-D) for the 94 elements H-Pu." *The Journal of chemical physics* 132, no. 15 (2010): 154104.

(17) Cheng, Tao, William A. Goddard, Qi An, Hai Xiao, Boris Merinov, and Sergey Morozov. "Mechanism and kinetics of the electrocatalytic reaction responsible for the high cost of hydrogen fuel cells." *Physical Chemistry Chemical Physics* 19, no. 4 (2017): 2666-2673.

(18) Cheng, Tao, Hai Xiao, and William A. Goddard. "Full atomistic reaction mechanism with kinetics for CO reduction on Cu (100) from ab initio molecular dynamics free-energy calculations at 298 K." *Proceedings of the National Academy of Sciences* (2017): 201612106.

(19) Cheng, Tao, Hai Xiao, and William A. Goddard III. "Free-energy barriers and reaction mechanisms for the electrochemical reduction of CO on the Cu (100) surface, including multiple layers of explicit solvent at pH 0." *The journal of physical chemistry letters* 6, no. 23 (2015): 4767-4773.

(20) Cheng, Tao, Hai Xiao, and William A. Goddard III. "Reaction mechanisms for the electrochemical reduction of CO2 to CO and formate on the Cu (100) surface at 298 K from quantum mechanics free energy calculations with explicit water." *Journal of the American Chemical Society* 138, no. 42 (2016): 13802-13805.

(21) Cheng, Tao, Hai Xiao, and William A. Goddard. "Nature of the active sites for CO reduction on copper nanoparticles; suggestions for optimizing performance." *Journal of the American Chemical Society* 139, no. 34 (2017): 11642-11645.

(22) Ping, Yuan, Robert J. Nielsen, and William A. Goddard III. "The reaction mechanism with free energy barriers at constant potentials for the oxygen evolution reaction at the IrO2 (110) surface." *Journal of the American Chemical Society* 139, no. 1 (2016): 149-155.

(23) Xiao, Hai, Tao Cheng, and William A. Goddard III. "Atomistic mechanisms underlying selectivities in C1 and C2 products from electrochemical reduction of CO on Cu (111)." *Journal of the American Chemical Society* 139, no. 1 (2016): 130-136.

(24) Xiao, Hai, Tao Cheng, William A. Goddard III, and Ravishankar Sundararaman. "Mechanistic explanation of the pH dependence and onset potentials for hydrocarbon products from electrochemical reduction of CO on Cu (111)." *Journal of the American Chemical Society* 138, no. 2 (2016): 483-486.

(25) Xiao, Hai, William A. Goddard, Tao Cheng, and Yuanyue Liu. "Cu metal embedded in oxidized matrix catalyst to promote CO2 activation and CO dimerization for electrochemical reduction of CO2." *Proceedings of the National Academy of Sciences* (2017): 201702405.

(26) Kresse, Georg, and Jürgen Furthmüller. "Efficient iterative schemes for ab initio total-energy calculations using a plane-wave basis set." *Physical review B* 54, no. 16 (1996): 11169.

(27) Perdew, John P., Kieron Burke, and Matthias Ernzerhof. "Generalized gradient approximation made simple." *Physical review letters* 77, no. 18 (1996): 3865.

(28) Perdew, John P., Kieron Burke, and Matthias Ernzerhof. "Generalized gradient approximation made simple." *Physical review letters* 77, no. 18 (1996): 3865.

(29) Stephens, P. J., F. J. Devlin, C. F. N. Chabalowski, and Michael J. Frisch. "Ab initio calculation of vibrational absorption and circular dichroism spectra using density functional force fields." *The Journal of Physical Chemistry* 98, no. 45 (1994): 11623-11627.

(30) Chase Jr, Malcolm W. "NIST-JANAF thermochemical tables." *J. Phys. Chem. Ref. Data, Monograph* 9 (1998).

(31) Kittel, Charles, Paul McEuen, and Paul McEuen. *Introduction to solid state physics*. Vol. 8. New York: Wiley, 1996.

(32) McClurg, Richard B., Richard C. Flagan, and William A. Goddard III. "The hindered rotor density-of-states interpolation function." *The Journal of chemical physics* 106, no. 16 (1997): 6675-6680.

(33) Campbell, Charles T., Lynza H. Sprowl, and Líney Árnadóttir. "Equilibrium constants and rate constants for adsorbates: two-dimensional (2D) ideal gas, 2D ideal lattice gas, and ideal hindered translator models." *The Journal of Physical Chemistry C* 120, no. 19 (2016): 10283-10297.

(34) Redondo, Antonio, Yehuda Zeiri, and William A. Goddard III. "Classical stochastic diffusion theory for desorption of atoms and molecules from solid surfaces." *Physical Review Letters*49, no. 25 (1982): 1847.

(35) Henkelman, Graeme, Blas P. Uberuaga, and Hannes Jónsson. "A climbing image nudged elastic band method for finding saddle points and minimum energy paths." *The Journal of chemical physics* 113, no. 22 (2000): 9901-9904.

(36) Henkelman, Graeme, and Hannes Jónsson. "A dimer method for finding saddle points on high dimensional potential surfaces using only first derivatives." *The Journal of chemical physics* 111, no. 15 (1999): 7010-7022.

(37) Heyden, Andreas, Alexis T. Bell, and Frerich J. Keil. "Efficient methods for finding transition states in chemical reactions: Comparison of improved dimer method and partitioned rational function optimization method." *The Journal of chemical physics* 123, no. 22 (2005): 224101.

(38) Grunze, M_, F. Bozso, G. Ertl, and M. Weiss. "Interaction of ammonia with Fe (111) and Fe (100) surfaces." *Applications of Surface Science* 1, no. 2 (1978): 241-265.

(39) Hsiao, Ming-Kai, Chia-Hao Su, Ching-Yang Liu, and Hui-Lung Chen. "Computational investigation of NH 3 adsorption and dehydrogenation on a W-modified Fe (111) surface." *Physical Chemistry Chemical Physics* 17, no. 45 (2015): 30598-30605.

(40) Satoh, Shinichi, Hiroshi Fujimoto, and Hisayoshi Kobayashi. "Theoretical study of NH3 adsorption on Fe (110) and Fe (111) surfaces." *The Journal of Physical Chemistry B* 110, no. 10 (2006): 4846-4852.

(41) Lin, Ren-Jie, Feng-Yi Li, and Hui-Lung Chen. "Computational investigation on adsorption and dissociation of the NH3 molecule on the Fe (111) surface." *The Journal of Physical Chemistry C* 115, no. 2 (2010): 521-528.

(42) Kua, Jeremy, and William A. Goddard. "Chemisorption of organics on platinum. 1. The interstitial electron model." *The Journal of Physical Chemistry B* 102, no. 47 (1998): 9481-9491.

(43) Kua, Jeremy, and William A. Goddard. "Chemisorption of Organics on Platinum. 2. Chemisorption of C2H x and CH x on Pt (111)." *The Journal of Physical Chemistry B* 102, no. 47 (1998): 9492-9500.

(44) Kua, Jeremy, Francesco Faglioni, and William A. Goddard. "Thermochemistry for Hydrocarbon Intermediates Chemisorbed on Metal Surfaces: CH n-m (CH3) m with n= 1, 2, 3 and m≤ n on Pt, Ir, Os, Pd, Rh, and Ru." *Journal of the American Chemical Society* 122, no. 10 (2000): 2309-2321. (45) Kua, J.; Goddard, W. A. *J. Am. Chem. Soc.* **1999**, *121*, 10928–10941.

(46) Ertl, G., and M. Huber. "Mechanism and kinetics of ammonia decomposition on iron." *Journal of Catalysis* 61, no. 2 (1980): 537-539.

(47) Ertl, G., M. Huber, S. B. Lee, Z. Paal, and M. Weiss. "Interactions of nitrogen and hydrogen on iron surfaces." *Applications of Surface Science* 8, no. 4 (1981): 373-386.

(48) Bozso, F_, G. Ertl, Mo Grunze, and M. Weiss. "Interaction of nitrogen with iron surfaces: I. Fe (100) and Fe (111)." *Journal of Catalysis* 49, no. 1 (1977): 18-41.

(49) Muhler, M., F. Rosowski, and G. Ertl. "The dissociative adsorption of N 2 on a multiply promoted iron catalyst used for ammonia synthesis: a temperature-programmed desorption study." *Catalysis letters* 24, no. 3-4 (1994): 317-331.

(50) Mortensen, Jens Jørgen, Lars Bruno Hansen, Bjørk Hammer, and Jens Kehlet Nørskov. "Nitrogen adsorption and dissociation on Fe (111)." *Journal of Catalysis* 182, no. 2 (1999): 479-488.

Chapter 3

Effect of Co Doping on Mechanism and Kinetics of Ammonia Synthesis on Fe(111) Surface

Jin Qian, Alessandro Fortunelli, and William A. Goddard III*. "Effect of Co Doping on Mechanism and Kinetics of Ammonia Synthesis on Fe(111) Surface." *Journal of catalysis*. Submitted Oct 2018, under review and revise.

Abstract

With the aim of improving the efficiency of the Haber-Bosch industrial process for the synthesis of ammonia, here we explore doping the traditional Fe-based Haber-Bosch catalyst with an impurity element. Starting from a previous experimentally-validated theoretical investigation of the reaction mechanism for Haber-Bosch synthesis of ammonia on the Fe bcc(111) surface, we focus on changes in mechanism and kinetics brought about by substitutional doping of 25% top layer iron with cobalt. The choice of Co is justified by the analysis of the wave functions of the critical reaction steps on the Fe(111) surface which showed that large changes in the net spin (magnetization) of the Fe atoms are thereby involved, and suggested that dopants with modified spins might accelerate rates. Quantum Mechanics values of free energies and reaction barriers are calculated for the Co-doped system for a set of 20 important surface configurations of adsorbates, and used as input to kinetic Monte Carlo (kMC) simulations to obtain final ammonia production. We find that at T = 673 K, P(H_2) = 15 atm, P(N_2) = 5 atm, and P(NH_3) = 1 atm, target conditions to drastically reduce the extreme energy cost of industrial ammonia synthesis process, top-layer Co doping leads to an **acceleration by a factor of 2.3 in reaction rates of ammonia synthesis**, and therefore an expected corresponding decrease in production costs.

3.1. Introduction

The Haber Bosch (HB) industrial process for the synthesis of ammonia (NH_3) from hydrogen (H_2) and nitrogen (N_2) is probably the most important reaction in heterogeneous catalysis. More than 140 millions of tons of ammonia gas are produced annually under

extreme conditions, typically at 773-823 °K and total pressure of 150-250 atm, entailing enormous expenditure of energy (2% of the world's supply).[1] [2] [3] [4] [5] [6] Several transition metals catalyze the Haber-Bosch process, such as iron, ruthenium, osmium, uranium and cobalt-molybdenum, but iron is still the most common and attractive choice because of its hardiness and low cost. [2] [6] [7] An essential goal of present research is therefore to dramatically reduce HB energy cost by improving the catalytic performance of the presently used Fe-based catalysts (so-called "ammonia iron" catalyst). [8] Given that the HB process has been investigated extensively at the experimental and industrial levels, with only marginal improvements in the last few decades, knowledge of the mechanistic steps as provided by first-principles-based theory and simulations may offer an alternative path to achieve the needed breakthrough. In this context, our line of investigation is to employ quantum-mechanics (QM)-based extensive sampling of the free-energy diagram of model but realistic systems coupled with kinetic modeling (in the form of kinetic Monte Carlo, kMC) so as to arrive at an in-depth understanding thus eventually leading to rational design. As the first step in this direction, we previously used QM/kMC to predict the reaction mechanism and kinetics for Haber-Bosch synthesis of ammonia on the Fe bcc(111) surface, which is the most active single-crystal Fe surfaces[9]. For 400 ºC and 20 atm total pressure of reactants in stoichiometric ratio at low NH_3 pressure, we predicted a turnover frequency (TOF) of 17.7 sec^{-1} per 2x2 site (5.3 x 10^{-9} moles/cm^2/sec) in excellent agreement with the TOF=9.7 sec^{-1} per site from single crystal experiments [9].[QianJACS2018] The QM calculations found 26 different surface configurations of adsorbates to play an important role and calculated the rates between these configurations that were used in kMC simulations to obtain the final rates. In analyzing the wave functions, we noticed that the critical reaction steps often involved large changes in the net spin (magnetization) of the Fe atoms involved, which suggested that using dopants with modified spins might improve some of the barriers. Preliminary calculations found that replacing Fe surface atoms with Co could lower some of the reaction barriers, making Co a reasonable candidate. Following these indications, we present here a thorough study which reports QM predictions for the free energies and reaction barriers assuming 25% Co doping of the top layer, followed by kMC to predict the overall TOF for various conditions. We provide a framework to

quantitatively investigate minority doping effects on bcc(111) surfaces, define a nomenclature for unambiguously single out Co-doped configurations, and analyze the changes in wave function and kinetics brought about by Co substitutional doping. We find that, under stoichiometric target conditions of T = 673 K, $P(H_2)$ = 15 atm, $P(N_2)$ = 5 atm, and $P(NH_3)$ = 1 atm, 25% Co-top-layer-doping leads to an acceleration in reaction rates by a factor of 2.3 in the reaction rate of ammonia synthesis, therefore potentially entailing a corresponding decrease in production costs – seemingly, a promising result for further studies.

3.2. Methods

QM calculations were performed within Density Functional theory (DFT) and using the Perdew-Burke-Ernzerhof (PBE) [10] exchange-correlation functional, including the D3 (Becke-Johnson)[11] empirical corrections for long-range dispersions (van der Waals). [12] This level of QM has been validated by comparison with experiment for the NH3 synthesis on Fe(111) and for the oxygen reduction reaction (ORR, O_2 + protons ➔ H_2O) on Pt(111)[13]. In both cases the calculated activation barriers were within 0.05 eV of the experiment.

All calculations were carried out with the VASP [14] software package, with an energy cutoff of 600eV and (4 x 4 x 1) K-point sampling, PAW pseudopotentials, and including spin-polarization.

3.2.1 Free Energy

To obtain the total free energy, G=H-TS at temperature T, we added to the DFT electronic energy (E), the zero-point energy (ZPE) from the vibrational levels (described as simple harmonic oscillators), and the specific heat contribution to the enthalpy from 0 to T. The entropy (S), as a sum of vibrational, rotational and translational contributions, is evaluated

using the same vibrational levels. To correct the free energy for pressure, we assume an ideal gas behavior and add $RT*\ln(P_2/P_1)$ with a reference pressure of $P_1 = 1$ atm.

The Free energy changes (δG) for the overall Haber Bosch reaction $N_2+3H_2 => 2NH_3$ under various conditions are calculated as

$$\delta G = 2*E(NH_3)+2*ZPE(NH_3)+2*H(NH_3)-2T*S(NH_3)-[E(N_2)+3*E(H_2)+ZPE(N_2)+3*ZPE(H_2)+H(N_2)+3*H(H_2)-T*S(N_2)-3T*S(H_2)]$$

The pressure dependence is added using $RT*\ln(P_2/P_1)$. We calculate δG is -0.52 eV for the HB reaction under 673°K, and 21 atm total pressure (5 atm and 15 atm for N_2 and H_2 respectively, and 1 atm for NH_3), which can be compared with δG =-0.02eV at 700°K and 5:15:1 atm N_2, H_2 and NH_3, respectively, from experiment.[15]

3.2.2 Surface Optimization

In the calculations here reported, we alloy only the top surface layer with 25% Co, so we use the lattice parameter of 2.807Å based on PBE-D3 value for Fe.

For pure Fe, our DFT predicts a magnetic moment for bulk Fe of 2.23 μB in excellent agreement with the experimental value, 2.22 μB.[16] We predict the magnetic moment for the 25% Co in the top layer to be 1.83 μB, while the moment on the neighboring surface Fe atoms change to 2.90 μB and the subsurface Fe to 2.50 μB.

We selected the bcc(111) surface that is known to be the most active for pure Fe [17]. We use a two-dimensional periodic slab with six layers of Fe atoms each of which consists of a (2 x 2) (6.873 Å x 7.937 Å) unit cell (4 surface Fe per cell). Then we replace 1 out of the 4 surface Fe atoms in the top layer with Co, as illustrated in Figure 3-1. We include 25 Å of vacuum in the z direction to minimize possible interactions between the replicated cells. The top three layers were relaxed while the bottom three layers were kept fixed at the optimum geometry calculated for bulk Fe.

The vibrational frequencies for free energy calculations were calculated allowing the adsorbed molecules and the top 3 layers of Fe and Co to relax (bottom 3 layers fixed), using

10^{-6} eV energy convergence threshold to obtain reliable phonon frequencies (no negative eigenvalues) within density functional perturbation theory (DFPT).

An identical procedure was used for the transition states. We note that some of the frequencies correspond to hindered translational or rotational modes, for which the harmonic oscillator description is less accurate. In these cases, namely NH_3 and N_2 desorption calculations, we use ZPE corrections only.[18–20]

3.2.3 Transition States

Transition state searches used the climbing image NEB method as implemented in the VASP-VTST code.[21] Here the initial and final states geometries were minimized first. Then three intermediate images were optimized, excluding initial and final images. An additional NEB climbing-image calculation was performed to obtain the final value of the barrier. The climbing NEB method generates a true transition state, as we confirmed by performing vibrational frequency calculations showing a single negative curvature in the Hessian. Whenever extra imaginary frequencies were found in the NEB transition state image, we performed dimer calculations [22]. For some transition state barriers that are not rate determining, we estimated the free energy corrections using the values from the previous pure Fe calculation. Examples are transition state from 3N.H hydrogenation to 2N.NH, hydrogen dissociation, and N migration. For all potential rate-determining steps, indicated by the red circles in Figure 3-3, we calculate the real barrier using the Co dopant.

3.2.4 Surface sites

The adsorption sites for the various species H, N, NH, NH_2, NH_3 calculated here are consistent with previous experimental[23,24] and DFT results[25–27]. The Fe(111) surface has four types of adsorption sites: top (T), bridge (B), 3-fold-shallow (S), and 3-fold-deep (D), with top/shallow (TS), and top-Shallow-deep (TSD) intermediate sites, as shown in Figure 3-1.

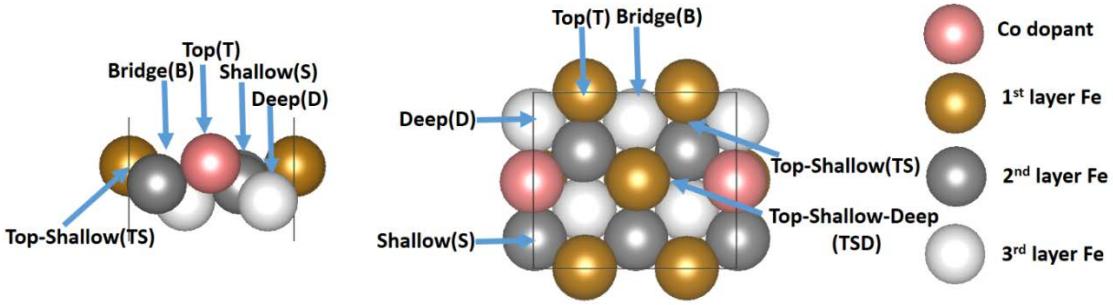

Figure 3-1. Structure of the ¼ ml Co doped-Fe(111) surface with various surface adsorption sites noted. Pink atom is Co dopant, bronze spheres represent the top layer, dark grey spheres represent the second layer, while white spheres are third layer Fe atoms. Multiple adsorption sites are labeled from both top and side views, including B, T, S, D, TS, and TSD sites. This figure shows only 3 of the 6 layers used in the calculations.

We find generally that

- H prefers the TS site between a top Fe and a 2nd layer Fe or the TSD site between Fe on all 3 layers
- N prefers the B site,
- NH prefers the BD site, with N sitting on the bridge(B) site, but NH pointing sideways toward the D site
- NH_2 prefers the TS site between a top Fe and a 2nd layer Fe.
- NH_3 prefers the T site.

but as shown below in SI Fig 1, the occupation at other sites sometimes shifts the minima.

Co dopant does not change preferred adsorption sites for any of the above species.

3.2.5 Nomenclature of configurations

Adsorption on the Co-doped surface generates a number of possible configurations, more than double the number in the pure Fe case (see Table 3-1), thus calling for the introduction of a dedicated nomenclature. This is illustrated in Table 3-1 and Figure 3-2, which considers all possible configurations in a (2x2) bcc(111) unit cell with up to 3 different species adsorbed in bridge (B) sites (D, S, TSD and TS sites can be associated with their nearest B sites). In Table 3-1 and Figure 3-2, the adsorbed species are generically named

A, B, and C. Here A is the majority adsorbate (at least 2 A present), which in Figure 3-2 A corresponds to a N adatom (in blue), while B is illustrated with a vacancy, and C is illustrated with an H adatom (in red). The rationale of the proposed nomenclature is based on the following 3 criteria:

- First, 2A stoichiometry can be realized in “linear” (indicated with “2A_l”) and “zig-zag” (indicated with “2A_z”) arrangements, depending on whether the 2 A species are located along a horizontal axis or staggered along the vertical axis.
- Second, in the Co-doped case, Co can be near the B-minority adsorbate (indicated with “/n”), at intermediate distance from B (indicated with “/i"), or far from B (indicated with “/f”), as in the 3A.B or the 2A_z.B.C configurations (thus e.g. the states: 3A.B/n, 3A.B/i, 3A.B/f, etc.).
- Third, in the Co-doped case, the Co dopant can be positioned in the same vertical column as the A species (indicated with “_a”), the B species (indicated with “_b”), or the C species (indicated with “_c”), thus e.g. the states: 2A_l.B.C_a, 2A_l.B.C_b, 2A_l.B.C_c, etc.

A given configuration of the pure Fe case can give rise up to 4 different structures after the introduction of Co, where – we note – intermediate and far configurations have typically similar energies.

Column1	Column2	Column3	Column4
Fe	# of possibilities(Fe)	Fe3Co	# of possibilities(Co)
4A	1	4A	1
3A.B	1	3A.B/n	3
		3A.B/i	
		3A.B/f	
2A_l.2B	1	2A_l.2B_a	2
		2A_l.2B_b	
2A_z.2B	1	2A_z.2B_a	2
		2A_z.2B_b	
2A_l.B.C	1	2A_l.B.C_a	3
		2A_l.B.C_b	
		2A_l.B.C_c	
2A_z.B.C	1	2A_z.B.C_a/n	4
		2A_z.B.C_a/f	
		2A_z.B.C_b	
		2A_z.B.C_c	

Table 3-1. Nomenclature for describing configurations space with at most 3 adsorbates on bridge sites of a (2x2) bcc(111) unit cell. Here capitalized characters A, B, and C indicate a different adsorbate on the surface (such as N, NH, NH_2, NH3, H, and V (vacancy)). For the 2A stoichiometry, the lower case "_z" suffix denotes a zig-zag arrangement, while "_l" indicates linear. Lower case "/n", "/i", and "/f" suffixes (for near, intermediate, and far, respectively) indicate the distance between B species and Co. Lower case "_a", "_b", and "_c" suffixes indicate that Co is in the same column as A, B, or C, respectively. See Figure 3-2 for a pictorial illustration.

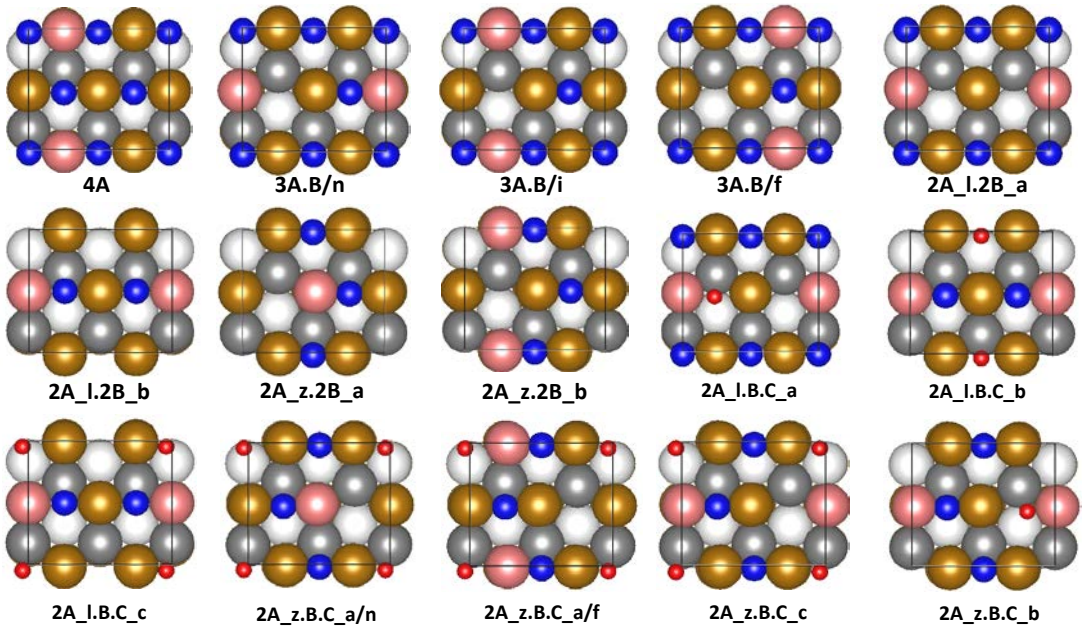

Figure 3-2. Graphical illustration of the proposed nomenclature, covering all possible states in configurational space with at most 3 adsorbates on bridge sites of a (2x2) bcc(111) unit cell. A, B, C are used for species adsorbed on the bridge site. In this illustration, A = N atom (blue circle), B = vacancy, C = H atom (red circle). First, second and third layer Fe atoms are depicted as gold, grey and white circles respectively, while surface dopant Co is in pink. Figure 3-1 and Table 3-1 are ordered in descending A stoichiometry, from 4A to 2A. A complete graphic illustration of all the possible states considered is included in the Supplementary Materials, Figure S3-1.

3.3. Energy landscape. The most favorable pathways for converting $3H_2 + N_2$ to $2NH_3$, with illustrations for T=673°K and p=20atm

We carried out DFT calculations on a subset of 20 of the important configurations previously employed for investigating the HB process on Fe(111)[9] (the 20 for Fe become 37 for the Co-doped case when considering the states differing by the position of Co). A 2x2 unit cell of the bcc(111) surface is considered with a top-layer Co dopant and a variable number of H, N, NH, NH_2, NH_3 adsorbed species. For each configuration, we calculated the vibrational frequencies to obtain the free energy at the operational temperature. Then

we calculated the reaction barriers for the various reaction pathways. We finally used these values to find reaction sequences with lowest overall free energy barrier for the HB process of converting one N_2 and three H_2 to form two NH_3.

We take the free energy of the 3N_NH_2 state as our reference point, with G=0 (which also allows a direct comparison with Ref. [9]. As shown below, this state has the highest occupancy in our kMC simulations for the Co-doped system at T=673°K, P(H_2) = 15 atm, P(N_2) = 5 atm, and P(NH_3) = 1 atm, for a total pressure of P=21 atm.

It is worth noticing that, in contrast with pure Fe, Co doping stabilizes the 2N.NH_2.2H configuration by 0.03-0.11 eV with respect to 2N.NH_2.H (at 673K and 21 atm).

We examined the barriers between all the states connecting though reactions of N_2 and H_2 at various sites. This leads finally to the energy landscapes in Table 3-2 and Figure 3-3**,** involving 37 intermediate configurations involved in the lowest maximum barriers. We include in Figure 3-2 the states we found to be important for the steady state kinetics described in section 5. The favorable path shown in Figure 3-3 and Table 3-2 includes the transitions shown in Table 3-2 (all energies in eV).

nomenclature(Co1)	Co_set1	nomenclature(Co2)	Co_set2	name(Fe)	Fe
01_3N.NH_2/i	**0.00**	**02_3N.NH_2/n**	**0.13**	**3N.NH_2**	**0.00**
TS_01_03	0.57	TS_02_04	0.70	TS_3N.NH_2_3N.NH_2.H	0.57
03_3N.NH_2/i.H	0.28	04_3N.NH_2/n.H	0.30	3N.NH_2.H	0.27
TS_03_05	1.35	TS_04_06	1.37	TS_3N.NH_2.H_3N.NH_3	1.20
05_3N.NH_3/f	0.39	06_3N.NH_3/n	0.38	3N.NH_3	0.30
TS_05_08	1.49	TS_06_07	1.45	TS_NH_3desorp	1.33
08_3N.V/i	0.51	07_3N.V/n	0.46	3N	0.41
TS_08_09	1.08	TS_07_10	1.03	TS_3N_3N.H	0.98
09_3N.H/i	0.21	10_3N.H/n	0.20	3N.H	0.09
TS_09_11	1.13	TS_10_12	1.12	TS_3N.H	1.01
11_2N_z.V.NH_b	0.69	12_2N_z.V.NH_c	0.72	2N.NH	0.57
TS_11_13	1.26	TS_12_14	1.29	TS_2N.NH_2N.NH.2H	1.14

13_2N_z.H.NH.H_b	0.78	14_2N_z.H.NH.H_c	0.70	2N.NH.2H	0.65
TS_13_15	1.04	TS_14_16	0.96	TS_2N.NH.2H_2N.NH2.H	0.91
15_2N_z.H.NH_2_b	0.26	16_2N_z.H.NH_2_c	0.25	**2N.NH_2.H**	**-0.04**
TS_15_38	0.83	TS_16_39	0.82	TS_2N.NH2.H_2N.NH2.2H	0.53
38_2N_z.NH_2.2H_c	**0.15**	**39_2N_z.NH_2.2H_b**	**0.22**	2N.NH_2.2H	0.08
TS_38_58	**1.49**	**TS_39_57**	**1.56**	**TS_2N.NH2.2H_2N.NH3.H**	**1.48**
58_2N.H.NH_3_b	0.47	57_2N.H.NH_3_b	0.42	2N.NH_3.H	0.36
TS_58_29	**1.42**	**TS_57_30**	**1.37**	**TS_NH_3desorption**	**1.38**
29_2N_z.H.V_b	0.54	30_2N_z.H.V_c	0.56	2N.H	0.48
TS_29_33	1.11	TS_30_33	1.13	TS_2N.H_2N.2H	1.05
33_2N_z.2H_b	0.23	33_2N_z.2H_b	0.24	2N_z.2H	0.14
31_2N_l.2H_a	**0.10**	**32_2N_l.2H_b**	**0.20**	**2N_l.2H**	**0.07**
33_2N_z.2H_b	0.23	33_2N_z.2H_b	0.24	2N.2H	0.14
TS_19_33	1.43	TS_19_33	1.43	TS_2N_2N.2H	1.38
19_2N_z.2V_b	0.86	19_2N_z.2V_b	0.86	2N	0.81
TS_19_52	**1.69**	**TS_19_51**	**1.69**	**TS_N_2adsorption**	**1.64**
52_2N_z.N_2gamma/n	0.85	51_2N_z.N_2gamma/f	1.04	2N.N_2_gamma	0.90
TS_52_54	1.29	TS_51_53	1.48	TS_N_2dissociation	1.34
24_4N	-0.28	24_4N	-0.28	4N	-0.40
TS_24_61	0.29	TS_24_61	0.29	TS_4N_4N.2H	0.17
61_4N.2H	0.18	61_4N.2H	0.18	4N.2H	0.08
TS_61_25	0.75	TS_61_26	0.75	TS_4N.2H_3N.NH.H	0.63
25_3N.NH.H_a/n	0.03	26_3N.NH.H_a/f	0.25	3N.NH.H	0.05
TS_25_01	0.63	TS_26_02	0.85	TS_3N.NH.H	0.65
01_3N.NH_2/i	-0.52	02_3N.NH_2/n	-0.39	3N.NH_2	-0.52

Table 3-2 Free energies along the favorable reaction pathway (36 states including transition state), organized in a parallel fashion. This compares the Fe, Co dopant set 1 and the Co dopant set 2. The transition state energy connecting every intermediate state is included. Data in this table is visualized in Figure 3-3. Important resting states such as 3N.NH_2, 2N.NH_2.H, 2N.NH_2.2H, and 2N_l.2H are shown in bold. The rate determining steps such as transition state from 2N.NH_2.2H to 2N.NH_3.H, transition state from 2N.NH_3.H to 2N.H, and transition state from 2N to 2N.N_2_gamma are highlighted using bold characters as well.

As for pure Fe, the NH_3 production rate is dominated by 3 types of reaction steps:

1). N_2 dissociation and adsorption. This barrier for Fe with respect to resting state 2N_l.2H is 1.64 – 0.07 = 1.57 eV. For Co dopants, this number changes to 1.59 eV and 1.49 eV.

2). Langmuir-Hinshelwood hydrogenation of NH_2. This barrier for Fe with respect to resting state 2N.NH_2.H is 1.48 – (-0.04) = 1.52 eV, while with Co dopants, this number changes to 1.34 eV and 1.34 eV. As noted above, there is a swap of resting state between 2N.NH_2.H for Fe and 2N_z.NH_2.2H for Co.

3). NH_3 desorption. This barrier for Fe with respect to the 2N_l.2H state is 1.38 – (-0.04) = 1.42 eV, while for Co dopants, this number changes to 1.27 eV and 1.15 eV.

We find that the NH_3 production pathway is similar overall to that on pure Fe. However, The Co surface dopant leads to a modified NH_3 turn over frequency (TOF) because it has a reduced spin, which modifies the energetics of intermediate states and transition states as shown in Figure 3-3.

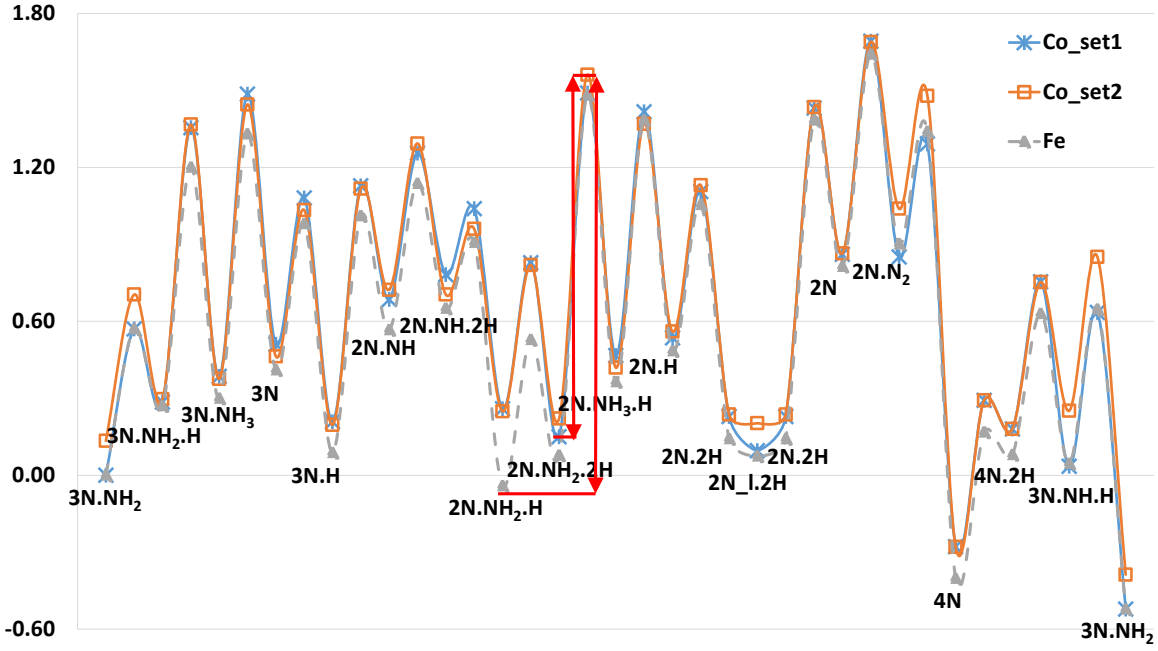

Figure 3-3. Energy landscape for NH_3 synthesis reactions with ¼ ml Co surface dopant under Somorjai condition, 673°K, 15 atm H2, 5 atm N2, 1 atm NH3. The lowest energy state 3N_NH_2 is taken as a reference, assigning a free energy of zero. We illustrate the full pathway on pure Fe(111) in dashed grey and Co doping in solid blue and orange. Two sets of pathway regarding Co dopants are considered. **Set 1 has NH_x species far from Co dopant**, while set 2 has NH_2 near Co dopant in the resting state 3N.NH_2. The major differences brought about by Co doping to the HB free-energy diagram on Fe-bcc(111) are in the energies of 2N.NH_2.2H and 2N.NH_2.H configurations relative to each other and with respect to 3N.NH_2, as highlighted using red arrow in Figure 3-2.

The major differences brought about by Co doping to the HB free-energy diagram on Fe-bcc(111) are in the energies of 2N.NH_2.2H and 2N.NH_2.H configurations relative to each other and with respect to 3N.NH_2, as highlighted using red arrow in Figure 3-2. Thus, as noted above, 2N.NH_2.2H is less stable than 2N.NH_2.H on pure Fe, but it becomes lower in energy on the Co-doped surface. Overall, these states are destabilized with respect to 3N.NH_2, which now becomes the resting state under conditions of P(H_2) = 15 atm, P(N_2) = 5 atm, P(NH_3) = 1 atm, and T=673°K, which are realistic target operating conditions for a less energy-demanding HB process.

3.4. Discussion of the wavefunctions

Since Fe is ferromagnetic, we analyzed the magnetic moments of the various atoms and the changes in the key steps of ammonia synthesis. Total magnetic moments for all the states along the pathway is reported in Table 3-1. We can compare the change in magnetic moment for Co and Fe directly.

Configurations	total mag	μ(Co)	μ(Fe)	covalent bonds	ratio(Co)	ratio(Fe)	ratio(Co)-ratio(Fe)
48_Fe3Co111	62.79						
01_3N.NH2/I	55.74	-7.05	-7.66	10	70%	77%	-6%
02_3N.NH2/n	55.87	-6.92	-7.66	10	69%	77%	-7%
03_3N.NH2/i.H	55.28	-7.51	n/a	11	68%	n/a	
04_3N.NH2/n.H	55.31	-7.48	n/a	11	68%	n/a	
05_3N.NH3/f	55.50	-7.29	n/a	9	81%	n/a	
06_3N.NH3/n	55.56	-7.23	n/a	9	80%	n/a	
07_3N.V/n	55.97	-6.82	n/a	9	76%	n/a	
08_3N.V/i	55.86	-6.93	n/a	9	77%	n/a	
09_3N.H/i	55.65	-7.14	-7.75	10	71%	78%	-6%
10_3N.H/n	55.54	-7.25	-7.75	10	73%	78%	-5%
11_2N_z.V.NH_b	56.53	-6.26	-6.59	8	78%	82%	-4%
12_2N_z.V.NH_c	56.67	-6.12	-6.59	8	76%	82%	-6%
13_2N_z.H.NH.H_b	**55.46**	**-7.33**	**-7.48**	**10**	**73%**	**75%**	**-1%**

14_2N_z.H.NH.H_c	**55.54**	**-7.25**	**-7.48**	**10**	**72%**	**75%**	**-2%**
15_2N_z.H.NH2_b	**57.70**	**-5.09**	**-5.4**	**8**	**64%**	**68%**	**-4%**
16_2N_z.H.NH2_c	**57.53**	**-5.26**	**-5.4**	**8**	**66%**	**68%**	**-2%**
17_2N_z.V.NH3_b	58.01	-4.78	-5.3	6	80%	88%	-9%
18_2N.V.NH3_a/f	58.03	-4.75	-5.3	6	79%	88%	-9%
19_2N_z.2V_b	58.25	-4.53	-4.93	6	76%	82%	-7%
20_2N_l.2V_b	57.70	-5.09	n/a	6	85%	n/a	
21_2N_l.2V_a	58.19	-4.60	n/a	6	77%	n/a	
22_2N_z.N2alpha/n	57.12	-5.66	-6.11	8	71%	76%	-6%
23_2N_z.N2alpha/f	57.06	-5.73	-6.11	8	72%	76%	-5%
24_4N	53.07	-9.71	-9.98	12	81%	83%	-2%
25_3N.NH.H_a/n	54.09	-8.70	-8.84	12	72%	74%	-1%
26_3N.NH.H_a/f	54.06	-8.73	-8.84	12	73%	74%	-1%
27_2N_edge_f.H_c	57.14	-5.65	n/a	7	81%	n/a	
28_2N_edge_c.H_f	56.98	-5.81	n/a	7	83%	n/a	
29_2N_z.H.V_b	57.95	-4.84	n/a	7	69%	n/a	
30_2N_z.H.V_c	57.90	-4.89	n/a	7	70%	n/a	
31_2N_l.2H_a	56.98	-5.81	n/a	8	73%	n/a	

32_2N_l.2H_b	56.52	-6.27	n/a	8	78%	n/a	
33_2N_z.2H_b	57.61	-5.18	n/a	8	65%	n/a	
34_3N.NH_c	54.62	-8.17	n/a	11	74%	n/a	
35_3N.NH_f	54.58	-8.21	n/a	11	75%	n/a	
36_2N.NH2_TfSD	57.87	-4.92	n/a	7	70%	n/a	
37_2N.NH2_TcSD	57.71	-5.08	n/a	7	73%	n/a	
38_2N_z.NH2.2H_c	**56.92**	**-5.86**	**-5.93**	**9**	**65%**	**66%**	**-1%**
39_2N_z.NH2.2H_b	**56.98**	**-5.81**	**-5.93**	**9**	**65%**	**66%**	**-1%**
40_2N_z.V.NH3_c	57.93	-4.86	-5.3	6	81%	88%	-7%
41_4N_sub	n/a	n/a		n/a	n/a	n/a	
42_2N_edge_f.2H_c_sub	n/a	n/a		n/a	n/a	n/a	
43_4N_2Co	n/a	n/a		n/a	n/a	n/a	
44_4N_Co.Cosub_relax5	n/a	n/a		n/a	n/a	n/a	
45_4N_Co.Cothird_relax 5	n/a	n/a		n/a	n/a	n/a	
46_4NFe	n/a	n/a		n/a	n/a	n/a	
47_Fe111	n/a	n/a		n/a	n/a	n/a	
49_2N_z.N2prime/n	56.38	-6.41	-6.59	10	64%	66%	-2%
50_2N_z.N2prime/f	56.72	-6.07	-6.59	10	61%	66%	-5%
51_2N_z.N2gamma/f	57.31	-5.48	-5.92	6	91%	99%	-7%
52_2N_z.N2gamma/n	57.40	-5.39	-5.92	6	90%	99%	-9%
53_2N.N2delta/f	57.25	-5.54	-5.54	6	92%	92%	0%
total covalent character					75%	80% (77%*)	-5%

Table 3-3. Analysis of change in spin along the reaction pathway. The total magnetic moment for each state and the change with respect to pure Fe are shown. The number of covalent bonds assumes the simple VB picture that each surface N can make 3 bonds, each NH can make two, each NH_2 can make one as can H and that NH_3 makes none. Thus we assume each adsorbed N, NH, NH_2, NH_3, H will decrease the spin moment by 3, 2, 1, 0, 1 respectively.

We observed that Co dopant reduce the covalent character of the surface bond by an average of 5%. This is consistent with the electronegativity of Co (1.88) being slightly greater than Fe (1.83) [28]. We observed that surfaces with greater covalent character tend to raise the free energy G with respect to $3N.NH_2$, while less covalent surfaces lower the free energy.

Thus for increased rates in NH_3 production, we want to decrease the energy gap between stable states (shown in blue circles in Figure 3-3) and the high energy TS states (show in red circles of Figure 3-3). $2N.NH_2.H$, $2N.NH_2.2H$ and $3N.NH_2$ configurations are further analyzed and attached in Figure S3-2.

3.5. Kinetic modeling

We used the QM-derived free-energy diagram discussed in Section 3 to predict HB reaction rates under steady-state conditions via a kinetic Monte Carlo (kMC) approach.[29]. In kMC, we evaluated rates using transition state theory [30] as $(k_BT/h)\exp(-\Delta G\dagger/k_BT)$, where $\Delta G\dagger$ is the difference in free energy between the starting state and the saddle point. In the case of ER reactions involving gas-phase species turning into adsorbates, we again use transition state theory, but for the reverse LH process, and then we invoke microscopic reversibility principle to calculate the rate of the direct process. Typically, we used 4 independent replicas and 10^{10} kMC steps in each replica, testing that the results so produced are converged within 5% in the production rate.

We focused on conditions of $P(H_2)$ = 15 atm, $P(N_2)$ = 5 atm, $P(NH_3)$ = 1 atm, and T=673°K, which are realistic target operating conditions for a less energy-demanding HB process (to investigate possible hydrogen poisoning effects we also consider the case of $P(H_2)$ = 5 atm).

In order to achieve an unbiased comparison, we contrasted the pure Fe and Co-doped systems using a set of corresponding configurations (the correspondence is typically one-to-two because of the freedom associated with the presence of Co) and identical numerical parameters. Representative results are reported in Table 3-2, where we include kMC predicted: turn-over-frequency (TOF), per-cent populations (i.e., per-cent residence times), apparent free energy differences [evaluated as minus the logarithm of ratio of populations = P_i/P_0, where the reference states are chosen as $P_0 = P_{3N\_NH2}$], and thermodynamic free energy differences (ΔG) for selected configurations in a (2x2) unit cell under steady-state of ammonia synthesis.

Significantly, at $P(H_2)$ = 15 atm, $P(N_2)$ = 5 atm, $P(NH_3)$ = 1 atm, and T=673°K, we predict TOF =5.70 NH_3 molecules per second per (2x2) site on the Co-doped surface, compared to a predict TOF = 2.45 NH_3 molecules per second per (2x2) site for pure Fe-bcc(111). **Thus Co doping of the top layer accelerates NH3 synthesis by a factor of 2.3.**

In the introduction we quoted that on the pure Fe(111) surface we found the TOF = 17.7/sec from theory and 9.7/sec from experiment[9]. This was for a NH3 pressure of 1.5 torr. For pure Fe, NH_3 acts as a poison so that increasing the NH3 pressure to 1 atm reduces the TOF to 5.70/sec. On the other hand, for the Co-doped Fe(111) surface, reducing the NH_3 pressure to 1.5 torr changes the TOF to 51.3/sec.

Stoichiometric reactant conditions are near-optimal for these systems. Thus we predict that reducing the H_2 pressure from 15 atm to 5 atm decreases production rates in pure Fe to TOF = 0.72 NH_3 molecules per second per (2x2) site, and decreases the production rate in Co-doped Fe to TOF=0.75 NH_3 molecules per second per (2x2) site, which also reduces the acceleration ensured by Co doping.

These results can be rationalized as follows. As anticipated in Sections 3, 4, the increase in catalytic efficiency for Co doping are basically associated with a destabilization of the $2N.NH_2.2H$ and $2N.NH_2.H$ configurations relative to $3N.NH_2$, which now becomes the resting state under conditions of $P(H_2)$ = 15 atm, $P(N_2)$ = 5 atm, $P(NH_3)$ = 1 atm, and T=673°K. Indeed, Table 3-3 show that the population of $3N.NH_2$ under steady-state increases from 29% to 79% in comparing pure Fe to Co-doped, while the population of

$2N.NH_2.H$ drops from 48% to 1.3%, comparing pure Fe to Co-doped (we use the sum of Co_set1 and Co_set2 configurations). We note here that the steady-state apparent ΔG (i.e., the logarithm of the relative populations) for the most relevant states, reported in Table 3-2, show that the HB process before and after the ammonia desorption is not far from equilibrium. The rate-determining step under the chosen conditions is associated with hydrogen migration from $2N.NH_2.2H$ to $2N.NH_3.H$. Co doping does not substantially alter the free energy difference between this saddle point and the $3N.NH_2$ initial state. However, on the pure Fe surface $2N.NH_2.H$ is the resting state, which is lower in free energy by $\approx$ 0.03 eV with respect to $3N.NH_2$. The destabilization of $2N.NH_2.H$ and $2N.NH_2.2H$ due to Co doping, pushes these states above $3N.NH_2$, restores this configuration as the resting state, thus reducing the overall reaction free-energy barrier calculated as the free-energy difference between the resting state and the [$2N.NH_2.2H \rightarrow 2N.NH_3.H$] saddle point. Actually, this destabilization is greater than strictly necessary to achieve HB acceleration: an ideal dopant would bring both $2N.NH_2.2H$ and $2N.NH_2.H$ close to the zero of free-energy, i.e., $3N.NH_2$.

	T=673, pH_2=15, pN_2=5, pNH_3=1 **– Fe**			T=673, pH_2= 15, pN_2=5, pNH_3= 1 **– Co**		
configuration	t_i (%)	$-\ln(P_i/P_0)$	ΔG	t_i (%)	$-\ln(P_i/P_0)$	ΔG
$3N.NH_2$	29.32	0.00	0.00	71.01/7.54	0.00/0.13	0.00
3N.H	5.11	0.10	0.09	1.46/1.75	0.23/0.21	0.21/0.20
$2N.NH_2.H$	47.95	-0.03	-0.04	0.61/0.74	0.28/0.26	0.26/0.25
$2N\_z.NH_2.2H$	6.06	0.09	0.08	4.07/1.25	0.17/0.23	0.15/0.22
4N	3.72	0.12	-0.40	1.13	0.24	-0.28
2N_z.2H	1.70	0.17	0.14	7.11/1.30	0.13/0.23	0.23/0.24
2N_l.2H	5.59	0.10	0.07	0.68	0.27	0.10/0.20
TOF from kMC NH_3 mol/s/(2x2)	**2.45**			**5.70**		
total	80			186		

NH_3mol						
3N_NH_3 ↔ 3N	39			63/30		
2N_NH_3_H↔ 2N_H	41			63/30		
	T=673, pH_2=5, pN_2=5, pNH_3=1 – **Fe**			T=673, pH_2= 5, pN_2=5, pNH_3= 1 – **Co**		
configuration	t_i (%)	-ln(P_i/P_0)	ΔG	t_i (%)	-ln(P_i/P_0)	ΔG
3N.NH_2	60.67	0.00	0.00	83.73/8.98	0.00/0.13	0.00
3N.H	3.47	0.17	0.16	0.61/0.72	0.29/0.28	0.28/0.27
2N_z.NH_2.H	10.88	0.10	0.09	0.09/0.10	0.40/0.39	0.39/0.38
2N_z.NH_2.2H	0.79	0.25	0.24	0.33/0.10	0.32/0.39	0.31/0.38
4N	22.99	0.06	-0.27	4.01	0.18	-0.15
2N_z.2H	0.13	0.36	0.34	0.33/0.06	0.32/0.42	0.43/0.44
2N_l.2H	0.43	0.29	0.27	0.03	0.46	0.30/0.40
TOF from kMC NH_3 mol/s/(2x2)	**0.72**			**0.75**		
total NH_3mol	39			36		
3N_NH_3 ↔ 3N	20			24/-6		
2N_NH_3_H↔ 2N_H	19			24/-6		

Table 3-4. Results from kMC simulations using QM/DFT data under steady-state ammonia synthesis at 673 K and pressures of: P(N_2) = 5 atm, P(NH_3) = 1 atm, and two different H_2 pressures: P(H_2) = 15 or 5 atm. Per-cent of populations (i.e., per-cent residence times) = t_i(%), apparent free energy differences [evaluated as minus the logarithm of ratio of populations = P_i/P_0, where $P_0 = P_{3N\_NH2}$], and thermodynamic free energy differences (ΔG) for selected configurations in a Fe(111)-(2x2) unit cell either pure (left – **Fe**) or Co-doped (right – **Co**). For the Co-doped case, values for configurations only differing by the position of Co are reported separated by a slash symbol ("/"). Temperature in Kelvin, pressure in atmospheres, free-energy in eV. We also report turn-over-frequencies (TOF), i.e., NH_3

molecules produced per second per (2x2) unit cell under the given conditions [NH_3mol/s/(2x2)], and total number of NH_3 molecules produced in the kMC runs (total NH_3mol), further partitioned into the 2 main steps involving NH_3 adsorption/desorption: $3N\_NH_3 \leftrightarrow 3N$; $2N\_NH_3\_H \leftrightarrow 2N\_H$.

3.6. Summary and conclusions

We report here a comprehensive study of the mechanisms underlying NH_3 synthesis on Co-doped Fe bcc(111) catalysts. We calculate the reaction barriers explicitly for all 12 important steps involved and consider both Langmuir-Hinshelwood (surface species reacting with surface species) and Eley-Rideal (gas phase species reacting with surface species) processes. The QM was at the level of PBE including the D3 London dispersion (van der Waals attraction) corrections as was previously applied successfully to the Haber Bosch synthesis on pure Fe(111).[9] Thus considering a large (20) number of configurations with varying stoichiometry (actually a larger number, 37 vs. 20, due to the greater freedom induced by Co doping), correcting the DFT for phonons to get free energies at experimental reaction conditions, and carrying out extensive kinetic Monte Carlo simulations to obtain the steady state populations at target operating conditions (673°K , 15 atm H_2, 5 atm N_2, and 1 atm NH_3), **we predict TOF=5.70 for Co doped Fe(111) which is 2.3 times faster than the TOF= 2.45 for pure Fe under the same conditions. These results show that alloying Fe with Co can appreciably increase TOF for NH_3 production.** We are not aware of experiments or previous theory suggesting this means of improving NH_3 production, which could lead to slightly less severe conditions for the same rates or guarantee a reduction by a factor larger than 2 in the energy consumption even maintaining the same conditions and industrial plants as used presently. **Thus these results suggest experimental tests with modest doping of Co.**

We note here that our calculations considered doping only of the top layer. We calculate that doping Co into the 2nd layer is more stable than doping into the by 0.19 eV, so atomic layer deposition experiments should deposit much more than ¼ ML to ensure the ¼ doping at the surface. However, we anticipate that alloying Fe with 25% Co would lead to the conditions we calculate.

Associated content

Supporting Information. Complete sampling of possible states. Pictorial illustration of reaction pathway for two sets of Co doped structures.

Acknowledgements

This work was supported by the U.S. Department of Energy (USDOE), Office of Energy Efficiency and Renewable Energy (EERE), Advanced Manufacturing Office Next Generation R&D Projects under contract no. DE-AC07-05ID14517 (program manager Dickson Ozokwelu, in collaboration with Idaho National Labs, Rebecca Fushimi).
A.F. gratefully acknowledges financial support from a Short-Term Mission (STM) funded by ItalianConsiglio Nazionale delle Ricerche (CNR).

Many of the calculations were carried out on a GPU-cluster provided by DURIP (Cliff Bedford, program manager). This work used the Extreme Science and Engineering Discovery Environment (XSEDE), which is supported by National Science Foundation grant number ACI-1548562.

BIBLIOGRAPHY

(1) Erisman, J. W., M. A. Sutton, J. Galloway, Z. Klimont, and W. Winiwarter. "How a century of ammonia synthesis changed the world, Nat. Geosci., 1, 636–639." (2008).

(2) Mittasch, Alwin, and W. Frankenburg. "Early studies of multicomponent catalysts." In *Advances in catalysis*, vol. 2, pp. 81-104. Academic Press, 1950.

(3) Appl, M. "Ammonia–Catalysis and Manufacture. ANDERS NIELSEN (ED.), Springer, Heidelberg 1995, 346 Seiten, 23 Abb., 23 Tab., DM 298–, ISBN 3-540-58335-1." *Chemie Ingenieur Technik* 68, no. 5 (1996): 588-589.

(4) Jennings, J. Richard, ed. *Catalytic ammonia synthesis: fundamentals and practice*. Springer Science & Business Media, 2013.

(5) King, David Anthony, ed. *The chemical physics of solid surfaces and heterogeneous catalysis*. Vol. 5. Elsevier, 2012.

(6) Rosowski, F., S. Storck, J. Zühlke, G. Ertl, H. Knözinger, F. Schüth, and J. Weitkamp. "Handbook of Heterogeneous Catalysis." (2008): 3426-3432.

(7) Hellman, A., E. J. Baerends, M. Biczysko, T. Bligaard, Claus H. Christensen, D. C. Clary, S. V. Dahl et al. "Predicting catalysis: Understanding ammonia synthesis from first-principles calculations." (2006): 17719-17735.

(8) Nielsen, Anders. "Review of ammonia catalysis." *Catalysis Reviews* 4, no. 1 (1971): 1-26.

(9) Qian, Jin, Qi An, Alessandro Fortunelli, Robert J. Nielsen, and William A. Goddard III. "Reaction mechanism and kinetics for ammonia synthesis on the Fe (111) Surface." *Journal of the American Chemical Society* 140, no. 20 (2018): 6288-6297.

(10) Perdew, John P., Kieron Burke, and Matthias Ernzerhof. "Generalized gradient approximation made simple." *Physical review letters* 77, no. 18 (1996): 3865.

(11) Grimme, Stefan, Stephan Ehrlich, and Lars Goerigk. "Effect of the damping function in dispersion corrected density functional theory." *Journal of computational chemistry* 32, no. 7 (2011): 1456-1465.

(12) Grimme, Stefan, Jens Antony, Stephan Ehrlich, and Helge Krieg. "A consistent and accurate ab initio parametrization of density functional dispersion correction (DFT-D) for the 94 elements H-Pu." *The Journal of chemical physics* 132, no. 15 (2010): 154104.

(13) Cheng, Tao, William A. Goddard, Qi An, Hai Xiao, Boris Merinov, and Sergey Morozov. "Mechanism and kinetics of the electrocatalytic reaction responsible for the high cost of hydrogen fuel cells." *Physical Chemistry Chemical Physics* 19, no. 4 (2017): 2666-2673.

(14) Kresse, Georg, and Jürgen Furthmüller. "Efficient iterative schemes for ab initio total-energy calculations using a plane-wave basis set." *Physical review B* 54, no. 16 (1996): 11169.

(15) Chase Jr, Malcolm W. "NIST-JANAF thermochemical tables." *J. Phys. Chem. Ref. Data, Monograph* 9 (1998).

(16) Kittel, Charles, Paul McEuen, and Paul McEuen. *Introduction to solid state physics*. Vol. 8. New York: Wiley, 2005.

(17) Strongin, D. R., and G. A. Somorjai. "The effects of potassium on ammonia synthesis over iron single-crystal surfaces." *Journal of Catalysis* 109, no. 1 (1988): 51-60.

(18) McClurg, Richard B., Richard C. Flagan, and William A. Goddard III. "The hindered rotor density-of-states interpolation function." *The Journal of chemical physics* 106, no. 16 (1997): 6675-6680.

(19) Campbell, Charles T., Lynza H. Sprowl, and Líney Árnadóttir. "Equilibrium constants and rate constants for adsorbates: two-dimensional (2D) ideal gas, 2D ideal lattice gas, and ideal hindered translator models." *The Journal of Physical Chemistry C* 120, no. 19 (2016): 10283-10297.

(20) Redondo, Antonio, Yehuda Zeiri, and William A. Goddard III. "Classical stochastic diffusion theory for desorption of atoms and molecules from solid surfaces." *Physical Review Letters*49, no. 25 (1982): 1847.

(21) Henkelman, Graeme, Blas P. Uberuaga, and Hannes Jónsson. "A climbing image nudged elastic band method for finding saddle points and minimum energy paths." *The Journal of chemical physics* 113, no. 22 (2000): 9901-9904.

(22) Henkelman, Graeme, and Hannes Jónsson. "Improved tangent estimate in the nudged elastic band method for finding minimum energy paths and saddle points." *The Journal of chemical physics* 113, no. 22 (2000): 9978-9985.

(23) Grunze, M_, F. Bozso, G. Ertl, and M. Weiss. "Interaction of ammonia with Fe (111) and Fe (100) surfaces." *Applications of Surface Science* 1, no. 2 (1978): 241-265.

(24) Bozso, F_, G. Ertl, Mo Grunze, and M. Weiss. "Interaction of nitrogen with iron surfaces: I. Fe (100) and Fe (111)." *Journal of Catalysis* 49, no. 1 (1977): 18-41.

(25) Hsiao, Ming-Kai, Chia-Hao Su, Ching-Yang Liu, and Hui-Lung Chen. "Computational investigation of NH 3 adsorption and dehydrogenation on a W-modified Fe (111) surface." *Physical Chemistry Chemical Physics* 17, no. 45 (2015): 30598-30605.

(26) Satoh, Shinichi, Hiroshi Fujimoto, and Hisayoshi Kobayashi. "Theoretical study of NH3 adsorption on Fe (110) and Fe (111) surfaces." *The Journal of Physical Chemistry B* 110, no. 10 (2006): 4846-4852.

(27) Lin, Ren-Jie, Feng-Yi Li, and Hui-Lung Chen. "Computational investigation on adsorption and dissociation of the NH3 molecule on the Fe (111) surface." *The Journal of Physical Chemistry C* 115, no. 2 (2010): 521-528.

(28) Weast, Robert C., and S. M. Selby. "Handbook of Chemistry and Physics, The Chemical Rubber Co." *Boca Raton, Ohio B*77 (1971).

(29) Gillespie, Daniel T. "A general method for numerically simulating the stochastic time evolution of coupled chemical reactions." *Journal of computational physics* 22, no. 4 (1976): 403-434.

(30) Vineyard, George H. "Frequency factors and isotope effects in solid state rate processes." *Journal of Physics and Chemistry of Solids* 3, no. 1-2 (1957): 121-127.

Chapter 4

Dramatic Differences in CO_2 Adsorption and Initial Steps of Reduction Between Ag and Cu

Yifan Ye, Hao Yang, Jin Qian, Hongyang Su, Kyung-Jae Lee, Tao Cheng, Hai Xiao, Junko Yano*, William A. Goddard III*, and Ethan Crumlin*. " Dramatic differences in CO_2 adsorption and initial steps of reduction between Ag and Cu." *Nature Communication.* Submitted Oct 2018, under review and revise.

Abstract

Converting carbon dioxide (CO_2) into liquid fuels and synthesis gas is a national priority. But there is no experimental information on the initial atomic level events for CO_2 electroreduction on the metal catalysts to provide the basis for developing improved catalysts. In order to provide this experimental information, we used ambient pressure X-ray photoelectron spectroscopy (APXPS) to examine the processes as Ag is exposed to CO_2 both alone and in the presence of H_2O at 298 K, the results of which we correlated with quantum mechanics density to provide definitive interpretations. We find that physisorbed (*l*-) and chemisorbed (*b*-) CO_2 are *not* stable on pure Ag (111) surface, but rather gaseous CO_2 reacts with absorbed O on Ag surface to form a chemisorbed surface species ($O{=}CO_2^{\delta-}$). Adding H_2O and CO_2 then leads to up to four water attaching on ($O{=}CO_2^{\delta-}$) and two water attaching onto *b*-CO_2 on the surface. On Ag we find a very different and much more favorable mechanism involving the $O{=}CO_2^{\delta-}$ compared to that involving *b*-CO_2 on Cu. Each metal surface modifies both the chemical speciation and the respective adsorption energies, thus providing a new basis for tuning CO_2 adsorption behavior to facilitate selective product formations.

4.1 Introduction

In order to close the anthropogenic carbon circle while creating a sustainable hydrocarbon-based energy cycle, it is essential to discover new electrocatalysts that can efficiently convert

carbon dioxide (CO_2) into liquid fuels and feedstock chemicals[1-7]. However, CO_2 is highly inert, making the CO_2 reduction reaction (CO_2RR) unfavorable thermodynamically. High throughput experimental and computational screening methods have been employed to discover new advanced CO_2 reduction catalysts but these approaches are based on preconceived notions of the reaction mechanisms and have not produced dramatic successes[8-11]. To accelerate progress, we believe that it is essential to develop a complete atomistic understanding of how CO_2 interacts with and is transformed by the catalyst surfaces to provide guidance to design the catalyst to selectively tune the mechanisms for adsorption and activation.

Electrocatalysts such as Au, Ag, Zn, Pd, and Ga are known to yield mixtures of CO and H_2 at varying ratios depending on the applied voltage[12-16], with Ag exhibiting particularly high activity and selectivity to CO vs. H_2. We sought to obtain a comprehensive understanding of how CO_2 and H_2O molecules adsorb on the Ag surface and interact to initiate CO_2 dissociation and subsequent product formation. Here we report our findings combining *in situ* ambient pressure X-ray photoelectron spectroscopy (APXPS) with quantum mechanics (QM), which leads to unexpected and exciting findings for CO_2 surface adsorption on Ag surface that are quite different than observed previously for Cu surfaces (**Figure 4-1a, b**).

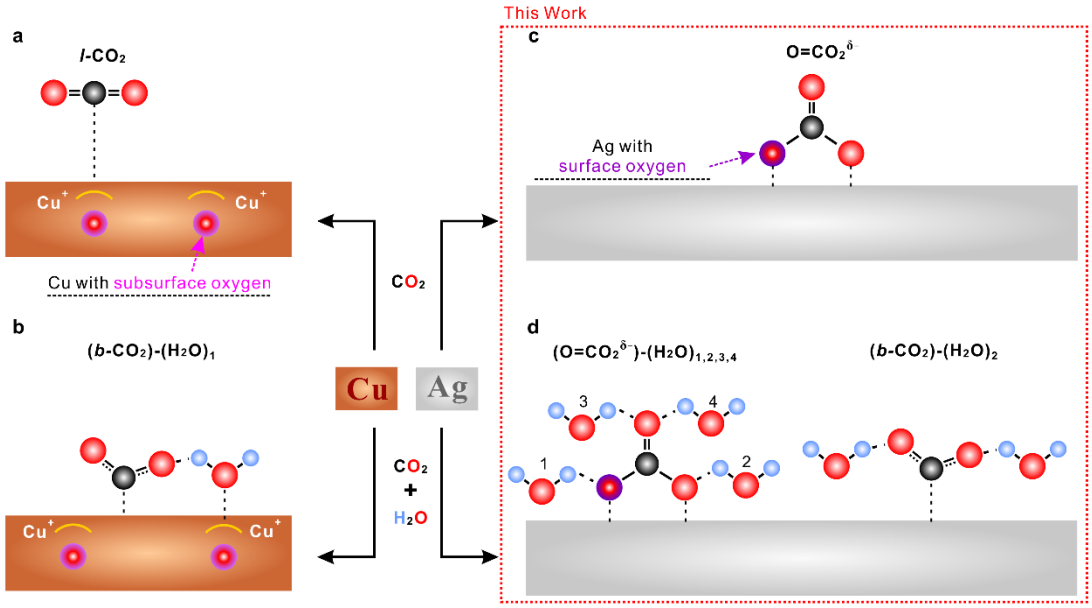

Figure 4-1 | Overview of surface adsorptions and reactions of CO_2 on Cu and Ag surfaces under various conditions. a,**b** We earlier reported CO_2 adsorption on Cu (111) at 298 K both alone and in the presence of H_2O. These studies concluded that subsurface oxygen leads to a surface Cu^+ atom that stabilizes *l*-CO_2 sufficiently strongly to be stable at 298 K and 0.7 Torr (**a**). In the presence of subsurface O, we found that H_2O adsorbs preferentially to the Cu^+ site while interacting sufficiently strongly with CO_2 to stabilize the *b*-CO_2, (through a hydrogen bond (**b**)) sufficiently to be stable at 298 K and 0.7 Torr total pressure[17]. **c**,**d**, Based on our new studies of adsorbed CO_2 on the Ag surface alone and in the presence of H_2O at 298 K. We find that *l*-CO_2 is not stable on Ag surface even at CO_2 pressure of 0.3 Torr at 298 K. However, CO_2 reacts strongly with surface oxygen to form a carbonic acid like structure (**c**). This $O{=}CO_2^{\delta-}$ species can stabilize one to four adsorbed H_2O through hydrogen bonding (**d**). Furthermore, *b*-CO_2 can also be stabilized by a pair of surface adsorbed H_2O each forming a hydrogen bond with an O of *b*-CO_2 (**d**).

For both Ag and Cu surfaces, we find that oxygen (O) plays an essential role to induce reactions involving CO_2 and H_2O, but **the consequences for each metal are dramatically different**. We find that **subsurface O** (which stabilized both the linear (*l*-) and bent (*b*-) CO_2 in the Cu system[17,18]) **is not stable on Ag**; quantum mechanics (QM) finds that putting an O in an Ag subsurface site goes without a barrier to an on-top three-fold (η_3) site (Supplementary **Figure 4-1a**). Here we consider two types of gaseous conditions at 298 K: 0.3 Torr CO_2 only (**Figure 4-1c**), and 0.3 Torr CO_2 plus 0.15 Torr H_2O (**Figure 4-1d**) on both clean Ag surfaces and with deliberate addition of surface O. As the (111) surface is the closest packed, energetically the most favorable facet for fcc metals (such as Ag and Cu), experimental evidence indicated that silver (and Cu) catalyst treated with high temperature exposes this facets[17,19,20]. Thus our simulations were performed based on the Ag (111) surface to correlate with the experimental observations on vacuum annealed polycrystalline Ag surface.

4.2 Methods

QM calculations: All calculations were carried out with the Vienna Ab-initio Simulation Package (VASP). We used the Perdew–Burke–Ernzerhof (PBE) formulation of the generalized gradient approximation (GGA) exchange-correlation functional using the projector-augmented (PAW) method and including the D3 (Grimme, Becke, and Johnson) empirical corrections for long-range London dispersion. We used a plane-wave basis set cutoff of 600 eV. Reciprocal space was sampled by a Γ-centered Monkhorst–Pack scheme with 3 x 3 x 1 for all calculations. For full details see Supplementary Methods.

***In-situ* ambient pressure X-ray photoelectron spectroscopy measurements**: Ambient pressure XPS measurements were performed at Beamline 9.3.2 of the Advanced Light Source, Lawrence Berkeley National Laboratory.[43] The pristine Ag surface was *in-situ* prepared in the vacuum chamber by repeated argon sputtering (2keV, 60mins) and vacuum annealing (900 K, 60mins), leading to a clean surface with no detectable carbon- and oxygen-based contamination. During the APXPS measurements performed at 298K, CO_2 partial pressure was kept at 0.3 Torr for CO_2 adsorption, whereas the total pressure was kept at 0.45 Torr with 0.3 Torr CO_2 and 0.15 Torr H_2O. The purities of the dosing gases (CO_2, H_2O) were *in-situ* monitored by a conventional quadrupole mass spectrometer to ensure no additional gas cross-contamination (especially, the CO and H_2 gases). The XPS spectra were collected at an incident photon energy of 670 eV, in the following order: a low-resolution survey with a binding energy of 600 eV to –5 eV, then high-resolution scans of O1s, C1s and valence band. The IMFP for the photoelectrons was below 0.9 nm for all the spectra collected. For each condition, samples were equilibrated for at least 30 min before the measurement. By taking spectra at different sample spots and comparing spectra before and after beam illumination for 2hrs, we found beam damage on the sample is negligible during the measurements. For full details see Supplementary Methods.

4.3 Results and Discussion

CO_2 adsorption on Ag surfaces. We start by carrying out QM studies to examine the stability of various surface adsorbates on pristine Ag surfaces, considering both *l*- and *b*-

CO_2. The optimized structure for *l*- and *b*- CO_2 is found to be unfavorable with E_{ads} (QM electronic binding energies) = −0.15 eV and ΔG = +0.19 eV, and E_{ads} = +0.77 eV and ΔG = +1.13 eV, respectively (Supplementary **Figure 4-1b,c**). These and all other ΔG values are from QM calculations including zero point energy, entropy, and specific heat to obtain ΔG at 298K and the pressure quoted.

CO_2 adsorption on oxygen treated Ag surfaces. We started the calculation by considering the possible promotion effect of sublayer oxygen that we found to stabilize CO_2 adsorption on Cu surface. However, the QM calculation minimizes to surface oxygen for Ag. In the presence of isolated surface O, we found that *l*-CO_2 has ΔE_{ads} = −0.21 eV, but ΔG = +0.13 eV (Supplementary **Figure 4-1d**). Thus a pressure of ~30 Torr would be required to stabilize *l*-CO_2 on the O/Ag surface at 298 K. This contrasts with observations for Cu, where subsurface O stabilized the adsorption of *l*-CO_2 on Cu surface under 0.7 Torr CO_2 partial pressure at 298 K[17] (**Figure 4-1b**). This attraction resulted from the subsurface O in a tetrahedral site inducing Cu^+ character into the single Cu atom above it on the surface, which stabilized the *l*-CO_2. This oxygen promotion effect was not observed for Ag because the O is chemisorbed on top of the Ag, which did not facilitate Ag oxidation (to Ag^+)[19,21-25]. This contrasting result provides fresh insight into the tunability of CO_2 adsorption on metal surfaces.

We evaluated the stabilization of *b*-CO_2 next to surface O_{ad} on Ag, but the QM minimized to form a surface carbonic acid-like species (Supplementary **Figure 4-1e**) with a $C{=}O_{up}$ double bond (1.222Å) pointing up while the other two O bind to adjacent three fold Ag(111) sites with C-O lengths of 1.365Å and 1.354Å and O-Ag distances of 2.276Å (**Figure 4-2a** and Supplementary **Figure 4-2**). This is *not* an ionic carbonate possessing three similar O atoms, as had been speculated previously[26-28]. We tried putting only one O bridging to the surface but the structure rotated to form the bidentate species. The CO_2 bonding energy to form surface $O{=}CO_2^{\delta-}$ is ΔE_{ads} = −0.75 eV, ΔG = −0.28 eV. We denote this carbonic acid-like adsorbate as $O{=}CO_2^{\delta-}$ to indicate that the negative charge is on the two O binding to the Ag surface. The total charge of $O{=}CO_2^{\delta-}$ is $-1.26e^-$ and charge on C is +1.46, leading to C1s binding energies (BEs) of −269.45 eV. The simulated BE value corresponds to 287.9 eV in

the experimental observation (Figure 4-2b). The properties of the surface adsorbate (including those discussed in the later section) are summarized in Supplementary **Figure 4-3, 4**. The simulated vibrational frequency data for $O{=}CO_2^{\delta-}$ (and those discussed later) are summarized in Supplementary **Table 4-1**.

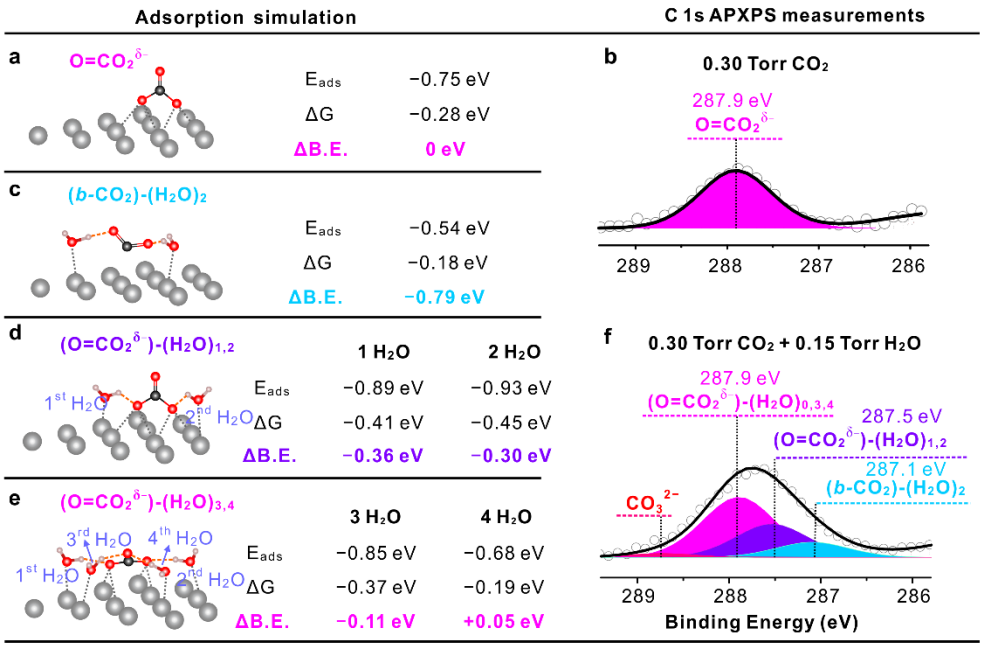

Figure 4-2 | The QM predictions and experimental observations of Ag surface with CO_2 adsorption alone and in the presence of H_2O at 298 K. a, Predicted structures for $O{=}CO_2^{\delta-}$ on Ag surface. The $O{=}CO_2^{\delta-}$ C1s peak BE has been set as the reference point for subsequent experiments with H_2O. **b,** The C1s APXPS spectra for Ag surfaces in the presence of 0.3 Torr CO_2 at 298 K. One single C1s peak representing $O{=}CO_2^{\delta-}$ was observed. **c,** *b*-CO_2 becomes stabilized by a pair of H_2O_{ad} each forming a hydrogen bond (HB) with an O of *b*-CO_2, leading to ΔG of −0.18 eV with respect to desorbing H_2O and CO_2. **d,e,** The adsorbed $O{=}CO_2^{\delta-}$ species stabilizes one or two H_2O_{ad} via HBs to the O_{ad} and two more water with HBs to the O_{up}. $O{=}CO_2^{\delta-}$ stabilizes the 1st, 2nd, 3rd, and 4th H_2O on this site with ΔG of −0.41 eV, −0.45 eV, −0.37 eV, and −0.19 eV, respectively. **f,** The C1s APXPS spectra and the peak deconvolution results for Ag surfaces in the presence of 0.3 Torr CO_2 and 0.15 Torr H_2O at 298 K. This deconvolution used the peak separations from the theory. The new surface adsorbates, $(O{=}CO_2^{\delta-})$-$(H_2O)_{1,2}$ and (*b*-CO_2)-$(H_2O)_2$, are observed experimentally in the

APXPS measurements, showing up as the two new peaks at 0.4 eV and 0.8 eV, lower than the $O{=}CO_2^{\delta-}$ peak. The species $(O{=}CO_2^{\delta-})$-$(H_2O)_{3,4}$ do not lead to additional peaks, because they are located at position that overlaps with that of $O{=}CO_2^{\delta-}$.

The adsorption states of CO_2 on various Ag surfaces at 298 K were monitored by C1s APXPS. The pristine Ag surface showed no detectable carbon- and oxygen- based contamination (Supplementary **Figure 4-5**), while dosing O_2 under different experimental conditions resulted in various oxygen coverages on Ag surface (Supplementary **Figure 4-6**).

We partition the C1s spectra obtained on clean and oxygen-covered Ag surfaces into two parts: (1) High binding energy region from 286 eV to 290 eV, showing the surface adsorbate, $O{=}CO_2^{\delta-}$ at 287.9 eV. $O{=}CO_2^{\delta-}$ is the only stable species on the Ag surface when exposed solely to CO_2 (no H_2O is present), leading to a single C1s peak in the adsorbate signal region of the APXPS spectra (**Figure 4-2b and Supplementary Figure 4-8**). (2) Low binding energy region from 282 eV to 286 eV represents the surface reaction products. The chemical species can be assigned as atomic C or carbide (283.0 eV), sp^2 C=C (284.2 eV), sp^3 C-C (285.2 eV), and C-O(H) (286.0 eV)[29-32].

Formation of this carbonic acid-like species requires O_{ad}, which can be constituted from O_2 pre-dosing and CO_2 self-decomposition prior to the CO_2 adsorption. As the initial surface O_{ad} coverage is increased (Supplementary **Figure 4-6**), CO_2 can directly adsorb on the surface to form $O{=}CO_2^{\delta-}$. This suppresses CO_2 dissociated surface carbon formation as evident in the decrease of the surface carbon (mainly the sp^2 C=C[29-32]) C 1s signals (Supplementary **Figure 4-9**), resulting in more available surfaces sites to increase the amount of adsorbed $O{=}CO_2^{\delta-}$ (Supplementary **Figure 4-8**).

Moreover, the experimental O1s spectra shown in Supplementary **Figure 4-6** provide insight to elucidate the surface chemistry. The two peaks that represent 2 O atoms attached to Ag surface and the single O atom in the C=O bond, were used to fit the spectra. The energy difference between these two peaks was set as 0.7 eV based on the QM results. This leads to 2:1 peak intensity ratio. Thus the peak fitting of the experimental data supports the QM results. By further comparing the C and O signals, we obtained that the C:O atomic ratio are

1:2.85, 1:3.13, and 1:2.97 for adsorbates on pristine and low and high oxygen covered Ag surfaces, which are all close to 1:3, providing another strong evidence of the formation of $CO_3^{\delta-}$ structure on Ag surface.

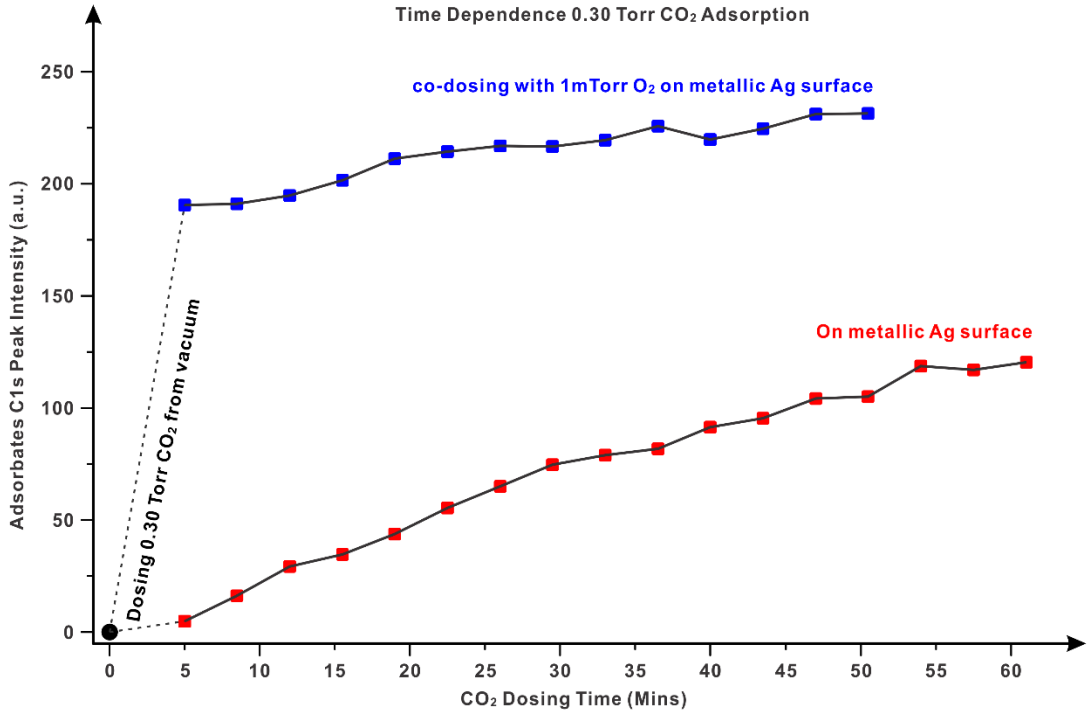

Figure 4-3 | The C1s signal of surface adsorbate increase as a function of CO_2 dosing time. The adsorbate signals for 300 mTorr CO_2 adsorption alone and in the presence of 1mTorr O_2 were recorded at an increased dosing time, shown as red and blue points, respectively. A black line across the data point is used for the eye guidance. The peak intensity is the raw intensity without considering the signal decay due to introducing gases.

The adsorption of CO_2 on pristine Ag surface both alone and at the presence of 1 mTorr O_2 at 298 K were investigated by recording the C1s peak intensity as a function of gas dosing time (**Figure 4-3**). The first spectrum was recorded after dosing CO_2 for 5 mins, which is the time period needed to reach 0.3 Torr pressure from the vacuum. In the case of the CO_2 adsorption, the adsorbate peak is negligible in the first spectrum recorded after 5 mins of CO_2 dosing, and it increased significantly as a function of increasing CO_2 dosing time. It reached equilibrate state after 60 mins gas adsorption. Adding O_2 with CO_2, even a ratio of 1:300,

significantly promoted the process of CO_2 adsorption on metallic Ag. The adsorbate signal is strong in the first spectrum, and it did not change dramatically as a function of the increasing dosing time. Since CO_2 adsorption on clean (non-oxygen pretreated) Ag surface requires a CO_2 dissociation process prior to the formation of the final surface adsorbate, the dynamics of $O{=}CO_2^{\delta-}$ formation on clean Ag surface is slower than that on the oxygen covered Ag surface. In the case of CO_2 adsorption on pristine Ag surface, surface O formation requires an additional process of CO_2 dissociation when interacting with the Ag surface. Moreover, since surface graphite carbon layer from CO_2 dissociation occupied the Ag sites and further decreased the $O{=}CO_2^{\delta-}$ coverage on the Ag surface, an increased adsorbate signal intensity was observed when co-dosing CO_2 with O_2. It is worth to note that, during this dynamic process, the O:C atomic ratio were calculated to be around 3:1, proving the surface adsorbate of $CO_3^{\delta-}$ structure, as shown in Supplementary **Figure 4-10**.

CO_2 adsorption on Ag surfaces in the presence of H_2O.

The QM studies find that the *l*-CO_2 configuration on Ag surface is not stable even considering the possible promotion effects of both O_{ad} and adsorbed water (H_2O_{ad}) (Supplementary **Figure 4-1f**). Adding H_2O to the surface with $O{=}CO_2^{\delta-}$ formed from gaseous CO_2 leads to two groups of structures stable at 298 K and the applied pressures (**Figure 4-1d**). First, a pair of surface H_2O stabilizes *b*-CO_2 on the Ag surface by forming two hydrogen bonds (HBs) between the H_2O_{ad} and CO_2 (**Figure 4-2c**). Second, $O{=}CO_2^{\delta-}$ can stabilize up to 4 H_2O molecules through formation of HBs to the surface bonds of $O{=}CO_2^{\delta-}$. The 1st and 2nd H_2O_{ad} each forms a hydrogen bond to one O_{ad} bonded to the surface (**Figure 4-2d**), while adding the 3rd and 4th H_2O forced the $C{=}O_{up}$ bond to rotate from being perpendicular to the surface to being nearly parallel to the surface, allowing the formation of HB from a 3rd and 4th surface H_2O_{ad} to the two sp^2 lone pairs on the $C{=}O_{up}$ unit (**Figure 4-2e** and Supplementary **Figure 4-2**). From QM predictions, the 1st and 2nd H_2O_{ad} shift the C1s from −269.45 eV to −269.09 eV and −269.15 eV, while the 3rd and 4th H_2O_{ad} shift the C1s back to −269.34 eV and −269.50 eV, nearly the same BE's as for no H_2O_{ad} bonding (**Figure 4-2f**). Considering that the $O{=}CO_2^{\delta-}$ and surface water stabilize each other through HB, an increase in the surface adsorbate coverage when dosing CO_2 in the presence of H_2O is

expected. This was experimentally observed as a dramatic adsorbate signal increase of C1s spectra compared to that from the adsorption of CO_2 alone (Supplementary **Figure 4-8**).

The tunability of CO_2 adsorption on metal surfaces. Activating inert CO_2 to *b*-CO_2 requires both a change of the geometric molecular structure and accommodation of extra charge. For Cu, *b*-CO_2 is stabilized by a subsurface O combined with a single surface adsorbed H_2O_{ad} while for Ag it is stabilized by two adsorbed H_2O_{ad}. The *b*-CO_2 with surface H_2O configuration leads to a similar amount of charge transferred directly from the metal catalyst to the C for both Cu and Ag. Interestingly, the *b*-CO_2 on Ag and Cu surfaces showed similar charge distribution but different C1s binding energy peak position. This may be ascribed to the increased final state screening effect of Cu on surface *b*-CO_2 due to the smaller distance between the surface adsorbate and the metal substrate (2.55 Å for C-Ag *vs.* 1.69 Å for C-Cu) [33]. The direct Ag-C interaction in (*b*-CO_2)-$(H_2O)_2$ leads to a $-0.67e^-$ charge accumulating on the adsorbed CO_2 molecule which is larger than the $-0.3e^-$ for the $O{=}CO_2^{\delta-}$ configuration (compared to O_{ad}) (**Figure 4-4**). Moreover, adding surface H_2O led to additional charge redistribution through the hydrogen bonding (**Figure 4-4**). Attaching more water to $O{=}CO_2^{\delta-}$ decreased the total charge on adsorbates, while the 1st H_2O decreased the charge on C atoms to +1.27 and the 2nd to 4th shift it back to +1.48, nearly the same as for no H_2O (**Figure 4-4**).

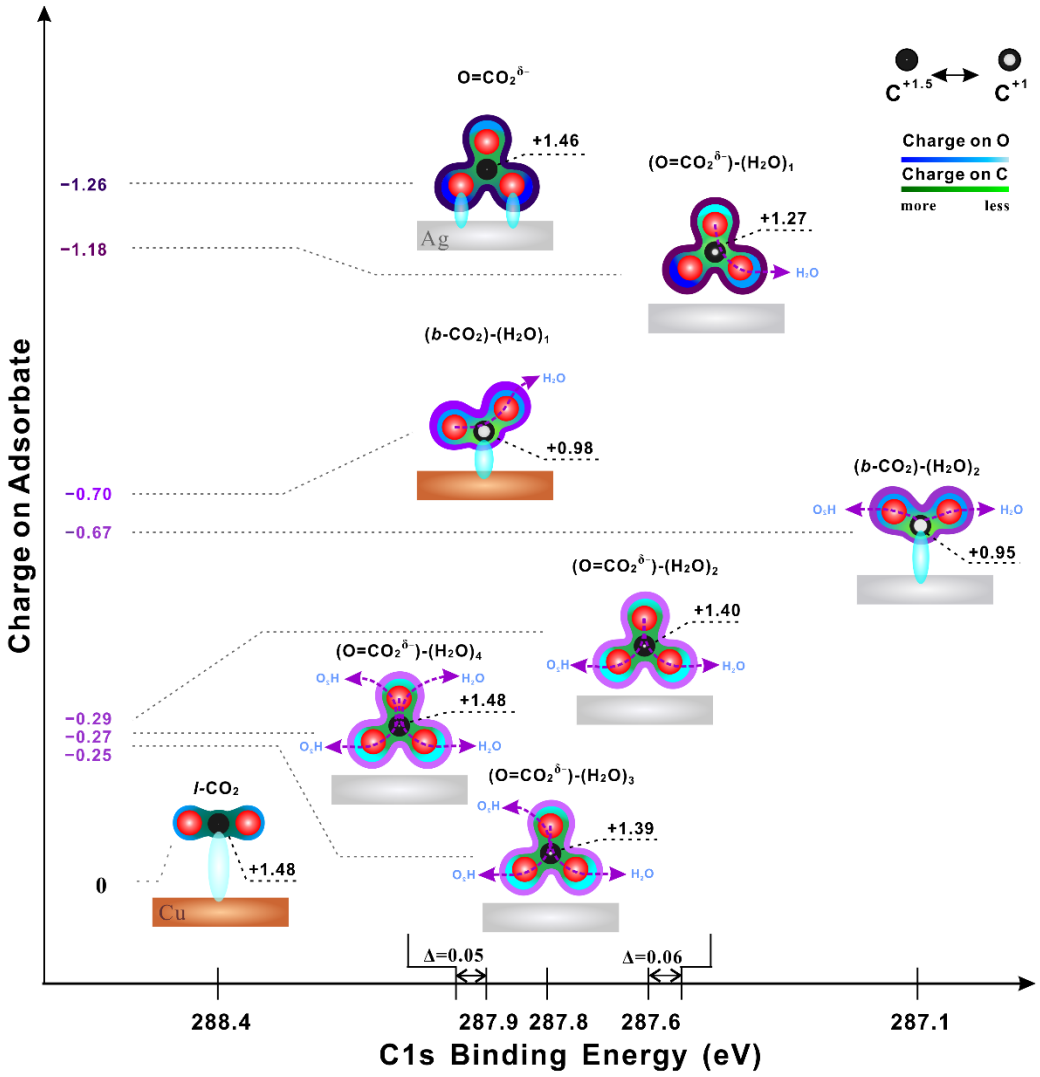

Figure 4-4 | The electronic properties of various surface adsorbates on Ag and Cu. The charge distribution (calculated by performing Bader Charge Analysis on optimized structures[34-36]) on the C, O and the adsorbates are summarized, with the corresponding C1s BE revisited. The various configurations of the adsorbates on the surface modified the charge transfer process, leading to different charge distribution on the adsorbates. Compared to *l*-CO_2 (only observed on Cu surface), CO_2 in the bent configuration exhibits extra charge accumulation. *b*-CO_2 is stabilized on Ag only with two surface H_2O but the charge distribution is similar to *b*-CO_2 on Cu surface. However, their different distances to the Ag and Cu surface, lead to different C 1s peak BE's. With the formation of the first two hydrogen

bonds to surface H_2O, the total charge on $O{=}CO_2^{\delta-}$ decreases, which decreases the C1s BE by ~ 0.30 eV. But adding the 3rd and 4th H_2O with HB to the $C{=}O_{up}$, of the $O{=}CO_2^{\delta-}$ increases the charge, shifting the BE back to 0.05 eV above the peak for no H_2O. Thus the predicting C1s shifts and charge distribution on surface adsorbates are fully consistent with the experimental observed C1s BE. These observed differences show the tunability of CO_2 adsorption on the metal surfaces.

This work highlights that the charge transfer configurations are responsible for the tunability of CO_2 adsorption on the metal catalyst surface. These results suggest two modes for stabilizing adsorbed CO_2. In the case of Cu, a subsurface O provided a positive Cu^+ on the surface that stabilized water molecule sufficiently to stabilize *b*-CO_2. This mechanism has been studied previously[37].

For Ag there is no subsurface O, but the surface O_{ad} promotes the formation of surface carbonic acid-like species, **$O{=}CO_2^{\delta-}$**, **which leads to a very different reaction mechanism for Ag than for Cu**. This new insight requires re-examining the subsequent steps of reactions to activate **$O{=}CO_2^{\delta-}$** to form products and how this depends on surface structure, solvent, pH, applied potential, the presence of anions and cations, and alloying with nonmetals (S, P, N, Cl) that might change the local charges and structures.

Proposed CO_2 reduction reaction pathway on Ag and Cu. The CO_2 adsorption on Ag contrasts dramatically from the results on Cu (Supplementary **Table 4-2**) providing possible explanations for why these metal catalysts have very different CO_2 reduction performances. For Cu our full explicit solvent QM calculations for the initial step of CO_2 to CO found that hydrogen bonding with the explicit solvent forms a similar *b*-CO_2 stabilized by two surface H_2O[37]. In that case, the next step is for one of these two H_2O molecules to transfer an H to form the HOCO intermediate plus OH_{ad} and then a 2nd surface H_2O transfers an H to the OH of HOCO to form H_2O plus OH_{ad}, leading to CO_{ad}, (this general reaction pathway is depicted in **Figure 4-5a**).

For Ag with (*b*-CO_2)-$(H_2O)_n$, **Figure 4-5a** shows that the QM predicted free energy barrier is 0.99 eV on Ag for protonating the complex of *b*-CO_2 with two H_2O to form HOCO* plus

OH* and H_2O (Supplementary **Figure 4-11**), leading to a total barrier of hydrogenation of CO_2 to HOCO* of −0.18+0.99 = 0.81 eV (**Figure 4-5a**). This energy barrier is comparable to that on Cu, which is 0.80 eV[37].

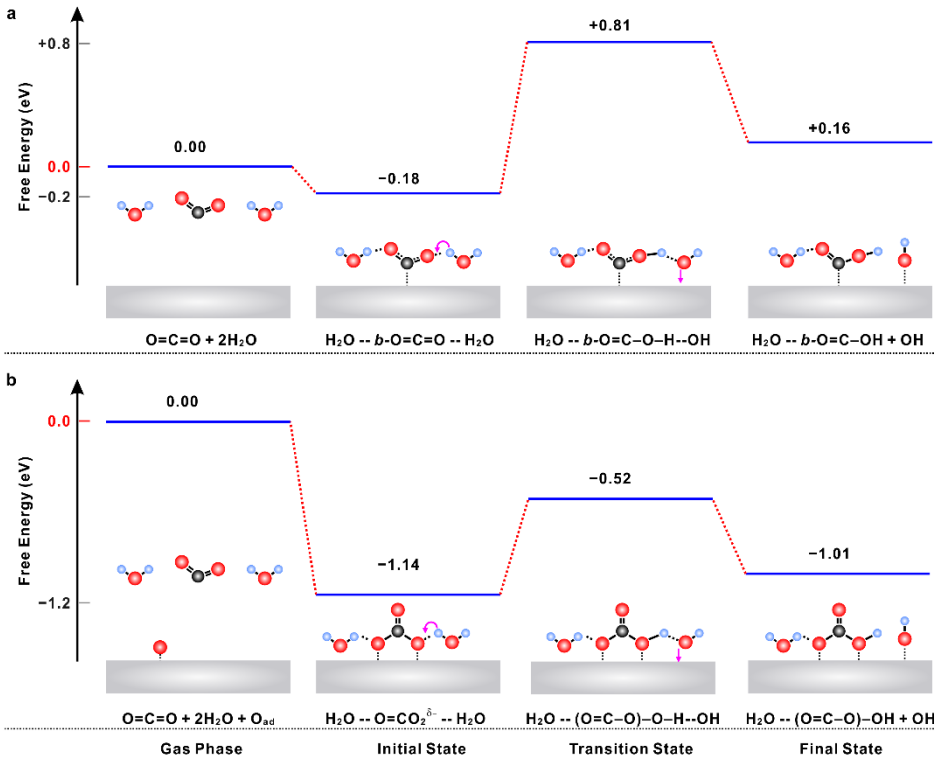

Figure 4-5 | The QM predicted kinetic pathway for the CO_2 hydrogenation process from full explicit solvent calculations. a. The reaction pathway starting with *b*-CO_2, the energy level of each step is referenced to gaseous (*g*-) CO_2 and *g*-H_2O; **b.** The reaction pathway starting with $O{=}CO_2^{\delta-}$, the energy level of each step is referenced to *g*-CO_2, *g*-H_2O and surface O_{ad}. The first step was shown in **Figure 4-2**, representing the stable adsorption configuration observed on the catalyst surface. The energy barrier information obtained from our climbing image nudged elastic band (NEB) calculations are detailed in Supplementary **Figure 4-11**. We consider here the case of $O{=}CO_2^{\delta-}$ with $2H_2O$ to compare directly with *b*-CO_2+$2H_2O$.

Surprisingly for Ag with $(O{=}CO_2^{\delta-})$-$(H_2O)_n$ clusters we find a different mechanism that is significantly more favorable. The discovery that $(O{=}CO_2^{\delta-})$-$(H_2O)_n$ is a stable surface cluster

is most unprecedented, differing dramatically from our previous understanding of CO_2 on a metal surface, which essentially all involve (*b*-CO_2)-(H_2O)$_n$ configurations[38-42].

We used QM to discover the mechanism of activation for the carbonic acid-like species on Ag. We find that the first step is for the H_2O hydrogen bonded to the surface O to transfer an H to form the (C=O)(O)(OH) intermediate plus OH_{ad}, as shown in **Figure 4-5b.** The QM energy barrier is 0.62 eV, which is dramatically lower than the value of 0.80 eV for Cu, perhaps explaining the faster rate for Ag. Thus the barrier of hydrogenation of CO_2 to OCOOH* of (−0.28)+(−0.41)+(−0.45)+0.62 = −0.52 eV (**Figure 4-5b** and Supplementary **Figure 4-11b**). This energy barrier is much smaller than for Cu. In particular, it is important to note that the energy levels of all the reaction steps starting with O=$CO_2^{\delta-}$ are negative. This suggests that we might be able to see this reaction in APXPS by simply increasing the temperature. These results predict that the most **energetically favorable** reduction reaction pathway to hydrogenate CO_2 to HOCO* involves the O=$CO_2^{\delta-}$ configuration present only on Ag surface. **This process is unprecedented and has never even been previously speculated.** This result raises numerous questions about subsequent steps that will drive many new experimental and theoretical studies to determine the implications. Future studies will include the operando spectroscopic characterizations of these adsorbates under external potentials, and we will predict the Tafel slope to compare with previous experimental observations and to gain more insights into the new mechanism.

Our studies have established a comprehensive but **totally new picture of the first steps of CO_2 activation on Ag**. The dramatic differences with Cu show how interactions between adsorbate and catalyst can be altered by tuning the charge transfer between them through changing the adsorption sites, configuration, and by introducing surface co-dosing adsorbates. These findings provide fresh insights about CO_2 adsorption species and the initial steps of CO_2 reduction mechanism on Ag surfaces. It is dramatically different from those on Cu surfaces, where *l*-CO_2 leads to *b*-CO_2 and then directly to CO_2 reduction[32].

4.4 Conclusions

Using synergistic experimental and theoretical analyses, we show that Cu and Ag operate entirely differently for the first step of activating CO_2, even though the product CO is the same. We find that surface O (from O_2 pre-dosing and CO_2 self-decomposition) interacts with *g*-CO_2 to form a carbonic acid like intermediate $O{=}CO_2^{\delta-}$, the only stable species on Ag surface (exposed to CO_2 only). Adding H_2O and CO_2 then leads to attaching up to four water on $O{=}CO_2^{\delta-}$. In addition, two water stabilize *b*-CO_2 on the Ag surface, which for Cu is the intermediate on the way to forming CO. On Ag we find a very different and much more favorable mechanism involving the $O{=}CO_2^{\delta-}$, one that has not been suggested or observed previously. This raises numerous questions about the subsequent steps that could motivate the exploration of new chemistries.

These studies emphasize the power from combining BE, vibrational frequency, APXPS with QM for discovering the fundamentals underlying CO_2 reduction. These unexpected findings will stimulate new thinking about the CO_2 reduction reactions on metal surfaces, suggesting that stabilization of various surface adsorption configurations can be controlled through additives or alloying along with externally applied potentials to control the reaction processes.

Acknowledgement

This work was supported through the Office of Science, Office of Basic Energy Science (BES), of the US Department of Energy (DOE) under Award DE-SC0004993 to the Joint Center for Artificial Photosynthesis, DOE Energy Innovation Hubs. The Advanced Light Source is supported by the Director, Office of Science, Office of BES, of the US DOE under Contract DE-AC02-05CH11231. H.Y. and H.S. gratefully acknowledge China Scholarship Council (CSC, No. 201608320161 and No. 201706340112) for financial support. This work used the Extreme Science and Engineering Discovery Environment (XSEDE), which is supported by National Science Foundation grant number ACI-1548562.

BIBLIOGRAPHY

(1) Qiao, Jinli, Yuyu Liu, Feng Hong, and Jiujun Zhang. "A review of catalysts for the electroreduction of carbon dioxide to produce low-carbon fuels." *Chemical Society Reviews* 43, no. 2 (2014): 631-675.

(2) Spichiger-Ulmann, Martine, and Jan Augustynski. "Electrochemical reduction of bicarbonate ions at a bright palladium cathode." *Journal of the Chemical Society, Faraday Transactions 1: Physical Chemistry in Condensed Phases* 81, no. 3 (1985): 713-716.

(3) Appel, Aaron M., John E. Bercaw, Andrew B. Bocarsly, Holger Dobbek, Daniel L. DuBois, Michel Dupuis, James G. Ferry et al. "Frontiers, opportunities, and challenges in biochemical and chemical catalysis of CO2 fixation." *Chemical reviews*113, no. 8 (2013): 6621-6658.

(4) Chu, Steven, and Arun Majumdar. "Opportunities and challenges for a sustainable energy future." *nature* 488, no. 7411 (2012): 294.

(5) Mistry, Hemma, Ana Sofia Varela, Cecile S. Bonifacio, Ioannis Zegkinoglou, Ilya Sinev, Yong-Wook Choi, Kim Kisslinger et al. "Highly selective plasma-activated copper catalysts for carbon dioxide reduction to ethylene." *Nature communications* 7 (2016): 12123.

(6) Mistry, Hemma, Ana Sofia Varela, Stefanie Kuehl, Peter Strasser, and Beatriz Roldan Cuenya. "Nanostructured electrocatalysts with tunable activity and selectivity." *Nature Reviews Materials* 1, no. 4 (2016): 16009.

(7) Gao, Shan, Zhongti Sun, Wei Liu, Xingchen Jiao, Xiaolong Zu, Qitao Hu, Yongfu Sun et al. "Atomic layer confined vacancies for atomic-level insights into carbon dioxide electroreduction." *Nature communications* 8 (2017): 14503.

(8) Yang, Hong Bin, Sung-Fu Hung, Song Liu, Kaidi Yuan, Shu Miao, Liping Zhang, Xiang Huang et al. "Atomically dispersed Ni (i) as the active site for electrochemical CO 2 reduction." *Nature Energy* 3, no. 2 (2018): 140.

(9) Gao, Shan, Yue Lin, Xingchen Jiao, Yongfu Sun, Qiquan Luo, Wenhua Zhang, Dianqi Li, Jinlong Yang, and Yi Xie. "Partially oxidized atomic cobalt layers for carbon dioxide electroreduction to liquid fuel." *Nature* 529, no. 7584 (2016): 68.

(10) Liu, Min, Yuanjie Pang, Bo Zhang, Phil De Luna, Oleksandr Voznyy, Jixian Xu, Xueli Zheng et al. "Enhanced electrocatalytic CO 2 reduction via field-induced reagent concentration." *Nature* 537, no. 7620 (2016): 382.

(11) Zhuang, Tao-Tao, Zhi-Qin Liang, Ali Seifitokaldani, Yi Li, Phil De Luna, Thomas Burdyny, Fanglin Che et al. "Steering post-C–C coupling selectivity enables high efficiency electroreduction of carbon dioxide to multi-carbon alcohols." *Nature Catalysis* 1, no. 6 (2018): 421.

(12) Lieber, Charles M., and Nathan S. Lewis. "Catalytic reduction of carbon dioxide at carbon electrodes modified with cobalt phthalocyanine." *Journal of the American Chemical Society*106, no. 17 (1984): 5033-5034.

(13) Hara, Kohjiro, Akihiko Kudo, and Tadayoshi Sakata. "Electrochemical reduction of carbon dioxide under high pressure on various electrodes in an aqueous electrolyte." *Journal of Electroanalytical Chemistry* 391, no. 1-2 (1995): 141-147.

(14) Hoshi, Nagahiro, Makiko Kato, and Yoshio Hori. "Electrochemical reduction of CO2 on

single crystal electrodes of silver Ag (111), Ag (100) and Ag (110)." *Journal of Electroanalytical Chemistry* 440, no. 1-2 (1997): 283-286.

(15) Back, Seoin, Min Sun Yeom, and Yousung Jung. "Understanding the Effects of Au Morphology on CO2 Electrocatalysis." *The Journal of Physical Chemistry C* 122, no. 8 (2018): 4274-4280.

(16) Mistry, Hemma, Yong-Wook Choi, Alexander Bagger, Fabian Scholten, Cecile S. Bonifacio, Ilya Sinev, Nuria J. Divins et al. "Enhanced Carbon Dioxide Electroreduction to Carbon Monoxide over Defect-Rich Plasma-Activated Silver Catalysts." *Angewandte Chemie* 129, no. 38 (2017): 11552-11556.

(17) Favaro, Marco, Hai Xiao, Tao Cheng, William A. Goddard, Junko Yano, and Ethan J. Crumlin. "Subsurface oxide plays a critical role in CO2 activation by Cu (111) surfaces to form chemisorbed CO2, the first step in reduction of CO2." *Proceedings of the National Academy of Sciences* (2017): 201701405.

(18) Xiao, Hai, William A. Goddard, Tao Cheng, and Yuanyue Liu. "Cu metal embedded in oxidized matrix catalyst to promote CO2 activation and CO dimerization for electrochemical reduction of CO2." *Proceedings of the National Academy of Sciences* (2017): 201702405.

(19) Li, Wei-Xue, Catherine Stampfl, and Matthias Scheffler. "Subsurface oxygen and surface oxide formation at Ag (111): A density-functional theory investigation." *Physical review B*67, no. 4 (2003): 045408.

(20) Bao, X., G. Lehmpfuhl, G. Weinberg, R. Schlögl, and G. Ertl. "Variation of the morphology of silver surfaces by thermal and catalytic etching." *Journal of the Chemical Society, Faraday Transactions* 88, no. 6 (1992): 865-872.

(21) Schmid, Michael, A. Reicho, A. Stierle, I. Costina, Jan Klikovits, P. Kostelnik, O. Dubay et al. "Structure of Ag (111)− p (4× 4)− O: No Silver Oxide." *Physical review letters* 96, no. 14 (2006): 146102.

(22) Schnadt, Joachim, Angelos Michaelides, Jan Knudsen, Ronnie Thorbjørn Vang, Karsten Reuter, Erik Lægsgaard, Matthias Scheffler, and Flemming Besenbacher. "Revisiting the structure of the p (4× 4) surface oxide on Ag (111)." *Physical review letters* 96, no. 14 (2006): 146101.

(23) Soon, Aloysius, Mira Todorova, Bernard Delley, and Catherine Stampfl. "Oxygen adsorption and stability of surface oxides on Cu (111): A first-principles investigation." *Physical Review B*73, no. 16 (2006): 165424.

(24) Li, Wei-Xue, Catherine Stampfl, and Matthias Scheffler. "Oxygen adsorption on Ag (111): A density-functional theory investigation." *Physical Review B* 65, no. 7 (2002): 075407.

(25) Andryushechkin, B. V., V. M. Shevlyuga, T. V. Pavlova, G. M. Zhidomirov, and K. N. Eltsov. "Adsorption of O 2 on Ag (111): Evidence of Local Oxide Formation." *Physical review letters*117, no. 5 (2016): 056101.

(26) Felter, T. E., W. H. Weinberg, G. Ya Lastushkina, A. I. Boronin, P. A. Zhdan, G. K. Boreskov, and J. Hrbek. "An XPS and UPS study of the kinetics of carbon monoxide oxidation over Ag (111)." *Surface Science* 118, no. 3 (1982): 369-386.

(27) Barteau, M. A., and R. J. Madix. "Photoelectron spectra of adsorbed carbonates." *Journal of Electron Spectroscopy and Related Phenomena* 31, no. 2 (1983): 101-108.

(28) Bowker, M., M. A. Barteau, and R. J. Madix. "Oxygen induced adsorption and reaction of H2, H2O, CO and CO2 on single crystal Ag (110)." *Surface Science* 92, no. 2-3 (1980): 528-548.

(29) Heine, Christian, Barbara AJ Lechner, Hendrik Bluhm, and Miquel Salmeron. "Recycling of CO2: probing the chemical state of the Ni (111) surface during the methanation reaction with ambient-pressure X-ray photoelectron spectroscopy." *Journal of the American Chemical Society* 138, no. 40 (2016): 13246-13252.

(30) Zhang, Liang, Liwen Ji, Per-Anders Glans, Yuegang Zhang, Junfa Zhu, and Jinghua Guo. "Electronic structure and chemical bonding of a graphene oxide–sulfur nanocomposite for use in superior performance lithium–sulfur cells." *Physical Chemistry Chemical Physics* 14, no. 39 (2012): 13670-13675.

(31) Deng, Xingyi, Albert Verdaguer, Tirma Herranz, Christoph Weis, Hendrik Bluhm, and Miquel Salmeron. "Surface chemistry of Cu in the presence of CO2 and H2O." *Langmuir*24, no. 17 (2008): 9474-9478.

(32) Taifan, William, Jean-François Boily, and Jonas Baltrusaitis. "Surface chemistry of carbon dioxide revisited." *Surface Science Reports* 71, no. 4 (2016): 595-671.

(33) Kong, Dandan, Guodong Wang, Yonghe Pan, Shanwei Hu, Jianbo Hou, Haibin Pan, Charles T. Campbell, and Junfa Zhu. "Growth, structure, and stability of Ag on CeO2 (111): synchrotron radiation photoemission studies." *The Journal of Physical Chemistry C* 115, no. 14 (2011): 6715-6725.

(34) Tang, W., E. Sanville, and G. Henkelman. "A grid-based Bader analysis algorithm without lattice bias." *Journal of Physics: Condensed Matter* 21, no. 8 (2009): 084204.

(35) Sanville, Edward, Steven D. Kenny, Roger Smith, and Graeme Henkelman. "Improved grid-based algorithm for Bader charge allocation." *Journal of computational chemistry* 28, no. 5 (2007): 899-908.

(36) Henkelman, Graeme, Andri Arnaldsson, and Hannes Jónsson. "A fast and robust algorithm for Bader decomposition of charge density." *Computational Materials Science* 36, no. 3 (2006): 354-360.

(37) Cheng, Tao, Hai Xiao, and William A. Goddard III. "Reaction mechanisms for the electrochemical reduction of CO2 to CO and formate on the Cu (100) surface at 298 K from quantum mechanics free energy calculations with explicit water." *Journal of the American Chemical Society* 138, no. 42 (2016): 13802-13805.

(38) Singh, Meenesh R., Jason D. Goodpaster, Adam Z. Weber, Martin Head-Gordon, and Alexis T. Bell. "Mechanistic insights into electrochemical reduction of CO2 over Ag using density functional theory and transport models." *Proceedings of the National Academy of Sciences* 114, no. 42 (2017): E8812-E8821.

(39) Ma, Ming, Kai Liu, Jie Shen, Recep Kas, and Wilson A. Smith. "In-situ Fabrication and Reactivation of Highly Selective and Stable Ag Catalysts for Electrochemical CO2 Conversion." *ACS energy letters* (2018).

(40) R Rosen, Jonathan, Gregory S. Hutchings, Qi Lu, Sean Rivera, Yang Zhou, Dionisios G. Vlachos, and Feng Jiao. "Mechanistic insights into the electrochemical reduction of CO2 to CO on nanostructured Ag surfaces." *Acs Catalysis* 5, no. 7 (2015): 4293-4299.

(41) Hatsukade, Toru, Kendra P. Kuhl, Etosha R. Cave, David N. Abram, and Thomas F. Jaramillo. "Insights into the electrocatalytic reduction of CO 2 on metallic silver surfaces." *Physical Chemistry Chemical Physics* 16, no. 27 (2014): 13814-13819.

(42) Wu, Jinghua, Yang Huang, Wen Ye, and Yanguang Li. "CO2 reduction: from the electrochemical to photochemical approach." *Advanced Science* 4, no. 11 (2017): 1700194.

(43) Grass, Michael E., Patrik G. Karlsson, Funda Aksoy, Måns Lundqvist, Björn Wannberg,

Bongjin S. Mun, Zahid Hussain, and Zhi Liu. "New ambient pressure photoemission endstation at Advanced Light Source beamline 9.3. 2." *Review of Scientific Instruments* 81, no. 5 (2010): 053106.

Chapter 5

Bridging the gap between Quantum Mechanics Calculations and XPS Spectroscopy: Decoding the initial H2O adsorption and complex formation on Ag(111) surface

Jin Qian, Yifan Ye, Hao Yang, Junko Yano*, Ethan Crumlin* and William A. Goddard III*. "Bridging the gap between Quantum Mechanics Calculations and XPS Spectroscopy: Decoding the initial H_2O adsorption and complex formation on Ag(111) surface.", preparing for submission.

Abstract

XPS and QM studies of CO_2 reduction on Cu(111) surface at 298K and ~ 1 torr pressure, showed that water plays a significant role by binding to a surface Cu+ site stabilized by a subsurface O and forming a hydrogen bond that stabilizes bent CO_2 , the first step in the reduction mechanism, where l-CO_2 + H_2O=> b-CO_2 +H_2O => HCO_2 + OH => CO + 2OH. [1]We recently reported that H_2O and surface O play a critical role for CO_2 reduction on Ag(111), but the mechanism is quite different, with surface O on Ag, activating CO_2 into a carbonic acid $O{=}CO_2^{\delta-}$ surface species that stabilizes surface H_2O that subsequently activates the $O{=}CO_2^{\delta-}$. In this paper, we address the issues of the nature of these O species, where they come from, how to characterize them, and their concentration on the surface. Previous works[2] attempted to assign the species associated with the observed XPS peaks, but there remain questions. Here we combine Quantum Mechanics calculations, Chemical Reaction Network (CRN) kinetics simulation, and atmospheric XPS experiment (apXPS), to connect the atomic understanding and the macroscopic picture. Our protocol not only characterizes surface species qualitatively, but also quantifies their populations, leading to excellent agreement with experiment and it should be transferable to other heterogeneous catalytic systems of interests.

5.1 Introduction

Ubiquitous in electrocatalytic systems are heterogeneous metal surfaces or metal nanoparticles with H_2O based solvent. Examples include CO_2 reduction (CO2RR) using Cu, Ag, and Au[3–6] and Oxygen Evolution (OER) using Ru, Ir, Pt.[7]. Thus, understanding the adsorption of H_2O at transition metal surfaces and their role in electrocatatysis is important for unraveling the chemistry at these solid−liquid interfaces.[8] In particular, surface oxygen was found to interact with CO_2 to form carbonate species [9]; adsorbed H_2O has been found to provide the H to protonate b-CO_2 or $CO_3^{\delta-}$; but OH was proposed to poison the surface by taking up 3-fold sites. Thus, characterizing the stability and concentration of oxygen containing species formed upon water adsorption are essential to the understanding of the first steps of adsorption, reaction, and selectivity to reduction products.

Previous experimental methods employed to provide a macroscopic picture for water adsorption on metal surfaces, include low-temperature UHV-based experiments,[9,10] Temperature-programmed desorption spectroscopy (TPD),[11-13] work function measurements,[14] and ultraviolet spectroscopy or X-ray photoelectron spectroscopy (UPS and XPS). [15,16]Among these experimental methods, XPS provides the sensitivity and resolution to distinguish oxygen containing surface species (surface O atom, subsurface oxygen atom, water clusters, or byproducts of H_2O decomposition such as OH, by measuring the O1s core electron binding energy (BE). Often, the XPS peak assignments are based on combining databases[17], previous publications, and chemical insight. In this work we created the following protocol to clearly and correctly reflects the chemistry:

a) Quantum Mechanics (QM) screening of stable surface adsorbents based on free energy G, under experimental condition of temperature and pressure

b) assignment of core level BE peak of stable surface species based on QM core level calculation

c) Chemical Reaction Network (CRN) kinetics simulation of the concentration of each surface species

d) deconvolution of XPS data using the QM core level shifts

e) cross-validation of experiment and theory by matching the intensity of deconvoluted peaks with the concentrations predicted from the CRN.

The key advantage of this new protocol is that both the peak position and peak intensity of multiple species in a complex system can be predicted in an ab-initio fashion, and can be cross-validated with the XPS experimental data directly. We demonstrate this procedure by decoding the complex landscape of H_2O adsorption on Ag(111) at 298K and different pressures, as shown in section 3. And then we predict isobar/isotherm conditions, which are both further tested and validated by experiments in section 4. At last, we predict the overall concentration landscape from room temperature to 500 ºC, and pressure from 10^{-6} torr to 1 torr.

5.2 Method

5.2.a DFT Calculation

All calculations, including geometric optimization, free energy correction, and O1s corelevel shift, were carried out with the Vienna Ab-initio Simulation Package (VASP).[18] We used the Perdew–Burke–Ernzerhof (PBE) formulation of the generalized gradient approximation (GGA) exchange-correlation functional using the projector-augmented (PAW) method and including the D3 (Grimme, Becke, and Johnson)[19] empirical corrections for long-range London dispersion.[20] We used a plane-wave basis set cutoff of 600 eV. We sampled reciprocal space by a Γ-centered Monkhorst–Pack scheme with 3 x 3 x 1 for all calculations.

The PBE-D3(BJ) level of DFT leads to a calculated lattice parameter of a = 4.012 Å for the bulk Ag structure at 0 K, slightly smaller than the experimental value 4.085 Å at 298□K. [21] We used experimental lattice parameter 4.085 Å to construct a two-dimensional periodic slab with four layers of Ag (111) atoms each of which consists of a (4 x4) unit cell (16 surface Ag per cell). We include 15 Å of vacuum in the z direction to minimize possible interactions between the replicated cells. The top two layers are relaxed while the bottom layers are kept fixed. The O1s core-level relative to gas phase H_2O was used to the position of the center of the peak.

Calculations for the gas phase molecules used the PBE functional (as implemented in Jaguar) with the D3 empirical correction for London dispersion.[19]

Free energy corrections of the enthalpy (H), entropy (S), and zero-point energy (ZPE) from Jaguar calculations are included in supplemental material. To obtain the total free energy, G=H-TS, for the gas molecules at temperature T, we add to the DFT electronic energy (E), the zero-point energy (ZPE) from the vibrational levels (described as simple harmonic oscillators), and the specific heat corrections in the enthalpy from 0 to T. The entropy (S) is evaluated from the same vibrational levels. To correct the free energy for pressure we assume an ideal gas and add RT*ln(P_2/P_1) with a reference pressure of P= 1 atm.

5.2.b CRN Kinetics Simulation

We relate the QM formation free energies to the reaction rate constant K, using the Arrhenius equation $K = kB * \frac{T}{h} * \exp\left(\frac{dG}{kB*T}\right)$. For each reaction, the rate depends on both the concentration of reactants, as well as reaction rate constant. For example, reaction A+B => C has the rate of $\frac{d[C]t}{dt} = [A]t * [B]t * K$. As the reaction proceeds, products from previous reaction serve as the reactants for the next reaction. Our purposed CRN is shown in the Result Section. We obtained numerical solutions for the CRN[22] at equilibrium state in terms of the population for each species for the (4x4) unit cell. The predicted population of each species is then used to determine the height of XPS peak (using the same full width at half maximum (FWHM) as the experimental value) for visualization purposes.

5.2.c Experimental Methods

Ambient pressure XPS/XAS measurements were performed at Beamline 9.3.2 of the Advanced Light Source, Lawrence Berkeley National Laboratory.[23] The pristine Ag surface was prepared *in-situ* in the vacuum chamber by repeated argon sputtering (2keV, 60mins) and vacuum annealing (900 K, 60mins). During the APXPS measurements performed at 298K, H_2O partial pressure was kept either at 0.15 Torr or 10^{-6} Torr. The purities of the dosing gases (H_2O) were *in-situ* monitored by a conventional quadrupole mass spectrometer to ensure no additional gas cross-contamination. The XPS spectra were collected at an incident photon energy of 670 eV, in the following order: a low-resolution survey with a

binding energy of 600 eV to –5 eV, then high-resolution scans of the O1s and the valence band. The IMFP (Inelastic mean free path) for the photoelectrons was below 0.9 nm for all the spectra collected. For each condition, samples were equilibrated for at least 30 min before measurements. By taking spectra at different sample spots and comparing spectra before and after beam illumination for 2hrs, we found beam damage on the sample is negligible during the measurements.

5.3 Result and Discussion

1) Adsorption geometry and O1s BE

Six species were investigated using DFT, with their adsorption geometries shown in Figure 1. We found that isolated OH* and O* adsorb at a fcc 3-fold site, while isolate H_2O* adsorbs at the on-top site, consistent with previous calculations. [24] H_2O molecule can also be stabilized by surface O* or OH* by forming hydrogen bonds, which we note as H_2O*---hb. We find that Multilayer H_2O molecules can be stabilized by OH*. The O1s core-level of each species is calculated using DFT with the relative values compared with experiment in Figure 2. The stability of these species as a function of temperature and pressure are shown and discussed in details in result section 2 and section 4.

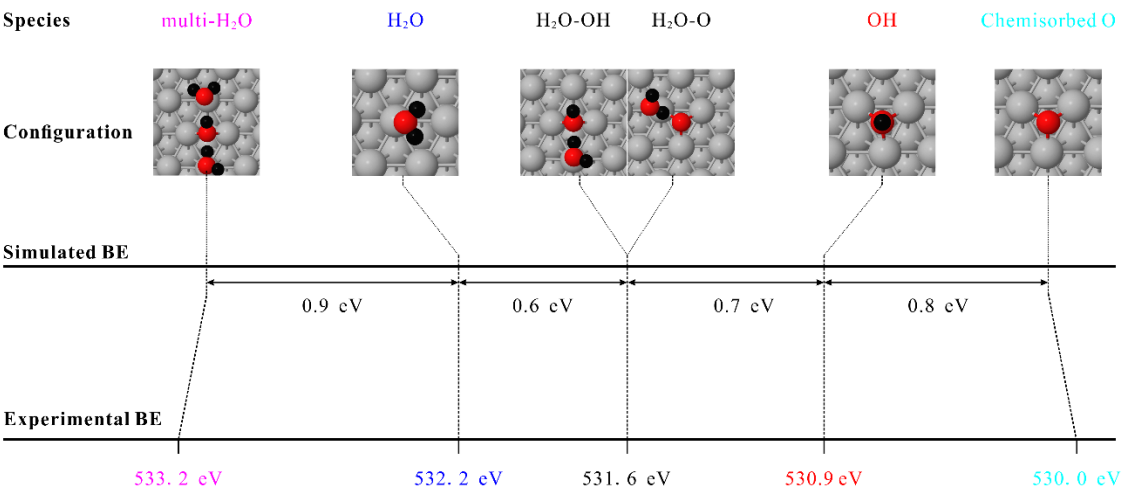

Figure 5-1. Assignment of oxygen containing species on Ag(111) surface by calculating the corelevel shift of O1s level, which shows excellent agreement with the ambient pressure XPS

experiment (all within 0.1eV). Five distinct peaks can be identified, including multilayer H_2O*, H_2O*, H_2O*---hb (including both H_2O*-OH, and H_2O*-O), OH* and O*.

2) Proposed CRN

We propose a CRN consisting of 12 reactions, where '*' denotes a surface site or adsorbed species, 'g' represents gas phase, and '---hb' indicates hydrogen bond formed with neighboring O or OH. Two extreme pressure condition (10^{-6} torr and 100 mtorr under room temperature) are chosen as representatives. G1 stands for the free energy for 100 mtorr and G2 stands for the free energy for 10^{-6} torr. The favorable reactions with negative energy are highlighted in bold character.

(1) adsorption O*+ H_2Og + *-> O*+ H_2O*---hb,
G1 = −0.28 eV, G2 = 0.02 eV

(2) adsorption OH*+ H_2Og+ *-> OH*+ H_2O*---hb,
G1 = −0.14 eV, G2 = 0.16 eV

(3) reaction O*+ H_2O*---hb -> 2OH*,
G1 = −0.32 eV, **G2 = −0.32 eV**

(4) diffusion H_2O*---hb+ OH*->H_2O*+ OH*,
G1 = 0.28 eV, G2 = 0.28 eV

(5) diffusion H_2O*---hb+ O*->H_2O*+ O*,
G1 = 0.41 eV, G2 = 0.41 eV

(6) desorption H_2O* -> H_2Og + *,
G1 = −0.14 eV, **G2 = −0.43 eV**

(7) adsorption H_2Og + * -> H_2O*,
G1 = 0.14 eV, G2 = 0.43 eV

(8) desorption OH* + H_2O*---hb -> OH*+ H_2Og,
G1 = 0.14 eV, **G2 = −0.16 eV**

(9) desorption O* + H_2O*---hb -> O*+ H_2Og,
G1 = 0.28 eV, G2 = −0.02 eV

(10) adsorption OH*+ H_2O*---hb + H_2Og ->OH* + multilayerH_2O,
G1 = −0.02 eV, G2 = 0.29 eV

(11) desorption OH* + multilayerH_2O -> OH*+ H_2O*---H + H_2Og,

G1 = 0.01 eV, **G2 = −0.29 eV**

(12) reaction 2OH* -> O*+ H_2O*---hb,

G1 = 0.32 eV, G2 = 0.32 eV

We consider that this CRN represents all possibilities for the initial steps of H_2O adsorption. Direct dissociation of H2O* -> OH* + H* and OH* -> O* + H* are not included in the CRN because their barriers are reported to be 1.80 eV, and 2.40 eV[25] respectively, which are orders of magnitude slower than all the presented than the reactions considered in current CRN (all within 0.5eV).

3) Direct Comparison of Theory and Experiment

To validate our protocol, we used two extreme pressure conditions (100 mtorr and 10^{-6} torr) for H_2O adsorption on Ag(111) surface . Direct comparison of theory and experiment is illustrated in Figure 2.

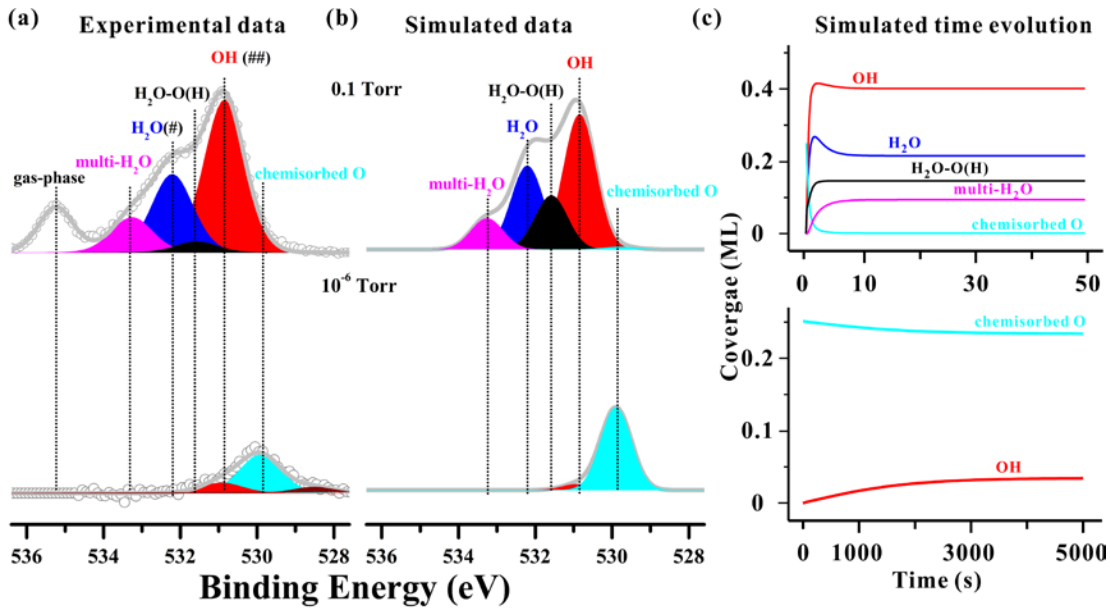

Figure 5-2 a)- c) Comparison between predicted populations in steady state from the CRN kinetics and experimental deconvoluted XPS populations. Color-code for OH* is red, O* sky-blue, H_2O*---H is black, H_2O* is navy, and multilayerH_2O is magenta. Top row is a

comparison between experiments and theory at P = 100 mtorr, room temperature; whereas bottom row is a comparison between experiments and theory at P = 10^{-6} torr a) column is the experimental spectrum, b) column is the theory prediction of the spectrum using QM and CRN, and c) column is the theory prediction of the time evolution of species concentration.

The relative concentration for the seven species are in excellent agreement with experiment. Note that we are not able to directly compare the population of gas phase H_2O (light grey). Similarly, experiment sees non-surface species AgOx (dark orange at around 528.5 eV in the experimental 10^{-6} torr spectrum), but our kinetics only focus on surface species and does not include them. The results can be explained using chemistry.

At high pressure (100 mtorr), the dominant chain reactions are:

$O^* + H_2Og \Rightarrow O^* + H_2O^*$---hb (1), follow by,

$O^* + H_2O^*$---hb $\Rightarrow 2OH^*$ (3),

This surface OH* can then stabilize additional gas phase H_2O and multilayerH_2O, as in

$OH^* + H_2Og \Rightarrow OH^* + H_2O^*$ (2),

OH*+ H2O*---hb + H2Og ->OH* + multilayerH2O, (10),

Assuming that the initial surface concentration of O* is sufficiently dilute (¼ mL) that the above product species can be accommodated, all O* should be consumed, so that the O*peak (orange) would be undetectable. Instead, strong OH* (red), moderate H_2O^*, H_2O^*---hb, and multilayer H_2O^* peaks are detected;

Under low pressure (10^{-6} torr), the chemistry is different:

$O^* + H_2Og \Leftrightarrow O^* + H_2O^*$---hb (1),

is in equilibrium. Although reaction

$O^* + H_2O^*$---hb $\Rightarrow 2OH^*$ (3),

is exoenergetic, the equilibrium would be for only a fraction of surface O* to help binding of H_2Og to then gets converted into OH via (1) and (3). As a result, strong O* and weak OH*

peaks are detected. Extrapolated from the low pressure regime XPS data, the O* concentration is estimated to be ¼ mL.

4) Predictions as a function of pressure and temperature

4a). Isotherm condition at 298K

Pressure plays two major roles in the kinetics.

1). Higher pressures of H_2Og increase the total amount of H_2O and products on the surface. (pV= nRT). Collison frequency increases as well, where the flux of particles impinging on the surface is given by fs = $p/\sqrt{2\pi mkBT}$

2). The Entropy term depends on pressure by RT*ln(P_2/P_1), so that the free energy for reactions involving adsorption and desorption are pressure-dependent.

As shown in Figure 4b, we predict that there are two regions of interest: low pressure region (below ~10^{-5} torr) where chemisorbed O* is dominant and some amount of OH is observed; and a more interesting high pressure region (~10^{-3} torr – 1torr), where all oxygen containing species except for chemisorbed O are present. The dominant species under high pressure region is OH*. This is further validated in the experimental data shown in Figure 4a.

Both experiments and theory arrives at the same trend for all species, which are summarized as below: OH* coverage increases until ~10mtorr and then decreases because of site constraint, as shown in reaction 3) O*+ H_2O*---hb => 2OH*, where two adjacent sites are required for the production of OH*. H_2O, H_2O-OH and multi H_2O coverage increases as pressure increases; among which H_2O coverage increases at the fastest speed.

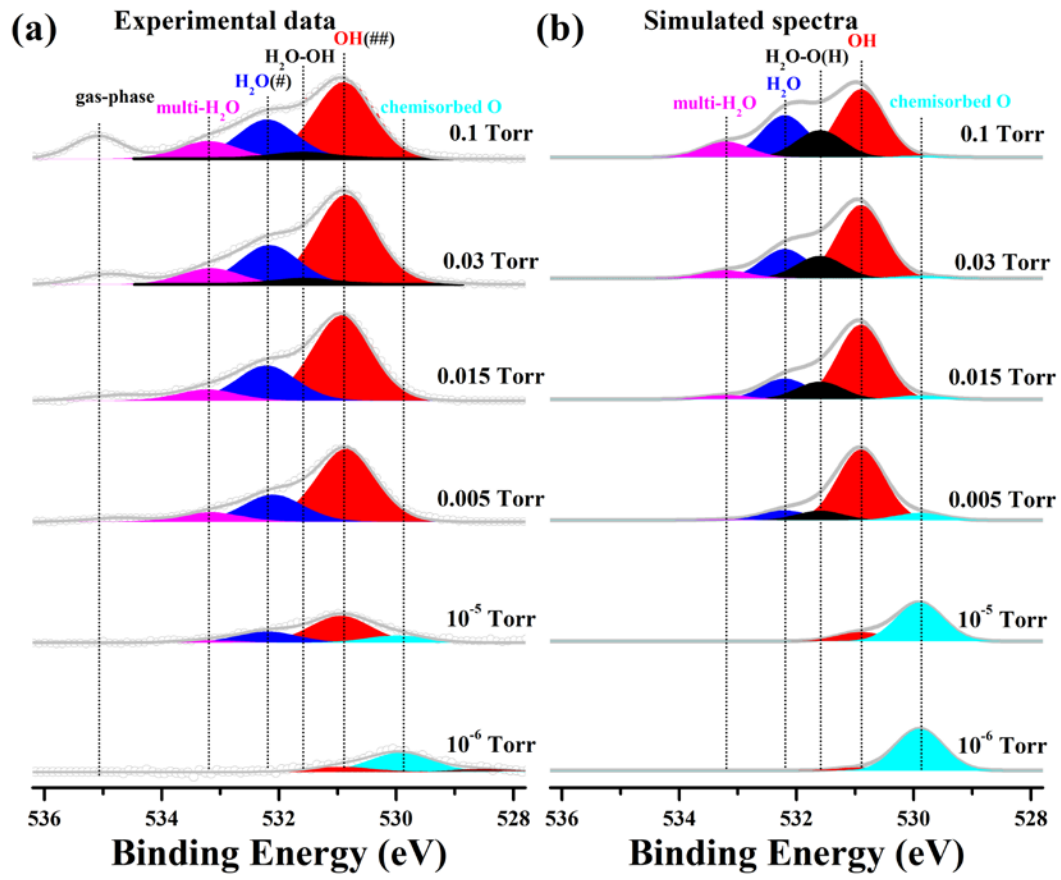

Figure 5-3 Isothermal condition at 298K, comparison of experiment and theory.

4b). Isobar condition at 100mtorr

Whereas temperature also plays two major roles in the kinetics.

1). The rotational, vibrational and translational entropy term depends on temperature, as calculated in Jaguar Maestro.

2). The rate constant for all 12 reactions involved in the CRN changes, as defined by Arrhenius equation $K=kB * \frac{T}{h} * \exp\left(\frac{dG}{kB*T}\right)$, where the final concentration profile of species is most sensitive to the exponential part.

As shown in Figure 5b, we predict that a non-negligible amount of chemisorbed O* starts to appear at around 423K, whereas all other species, such as multilayerH_2O*, H_2O*, and OH-H_2O* desorb and show a significant decrease in signal, in general agreement with the experiment shown in Figure 5a. The only small discrepancy is that OH was also observed to

decrease in signal in experiment, but theory does not show such obvious decrease, although some decrease is shown at higher temperature, see Figure 6. This discrepancy is hypothesized to be a possible existence of hydrogens in experimental condition, which could recombine with OH* and desorb as H_2Og at high temperature.

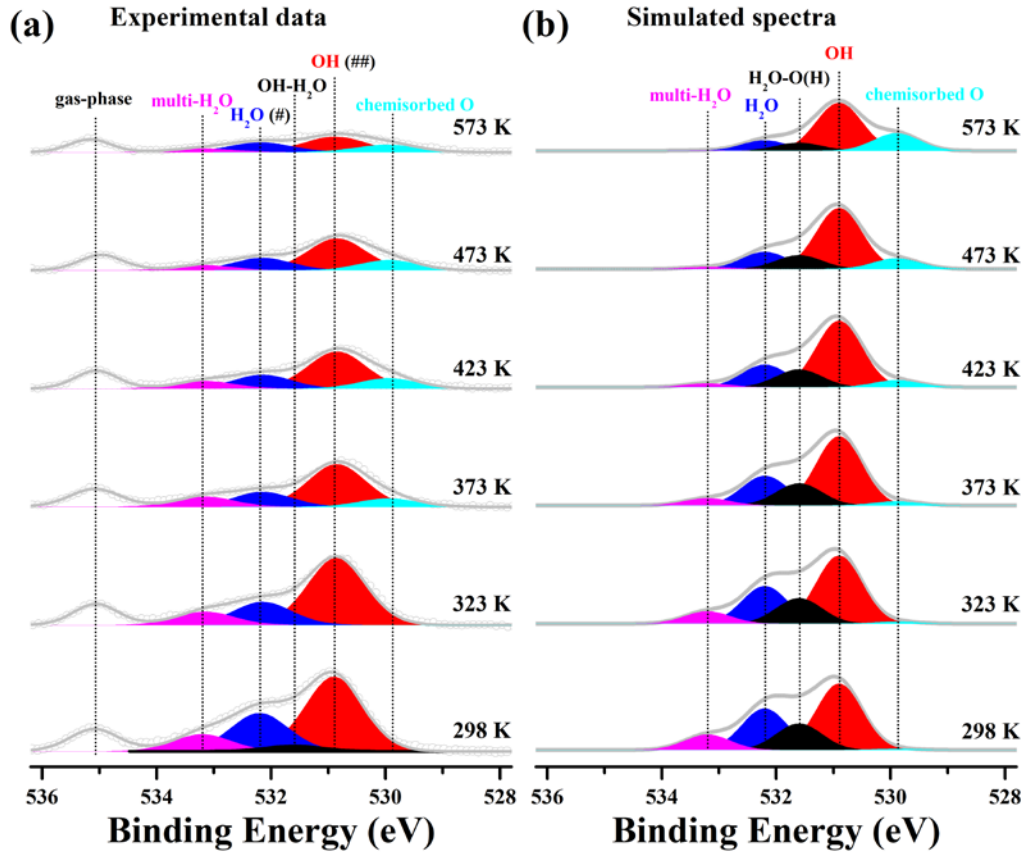

Figure 5-4 Isobar condition at 100mtorr, comparison of theory and experiment.

4c). Overall landscape

After our prediction and cross-validation of isotherm and isobar conditions, we extend our scope of predictions across a wide range of temperature and pressure, from 298K to 737K, 10^{-6} torr to 1torr. We notice the separation of high pressure region which all species except O* exist, and low pressure region, where strong O* signal and moderate OH* signal show up. We report that this transition point moves to the right hand side (higher pressure side) as temperature increases. This is mostly because reaction 3 is exothermic, and thus more O* would be present at higher temperature. O* and OH* are arguably the most reaction

important intermediates in this system, as they further determine the concentration of H_2O*, H_2O—hb and multilayerH_2O* as reaction 1, 2, and 10 proceed. At every T/P grid in Figure 6, we can visualize the relative concentration of all oxygen containing species.

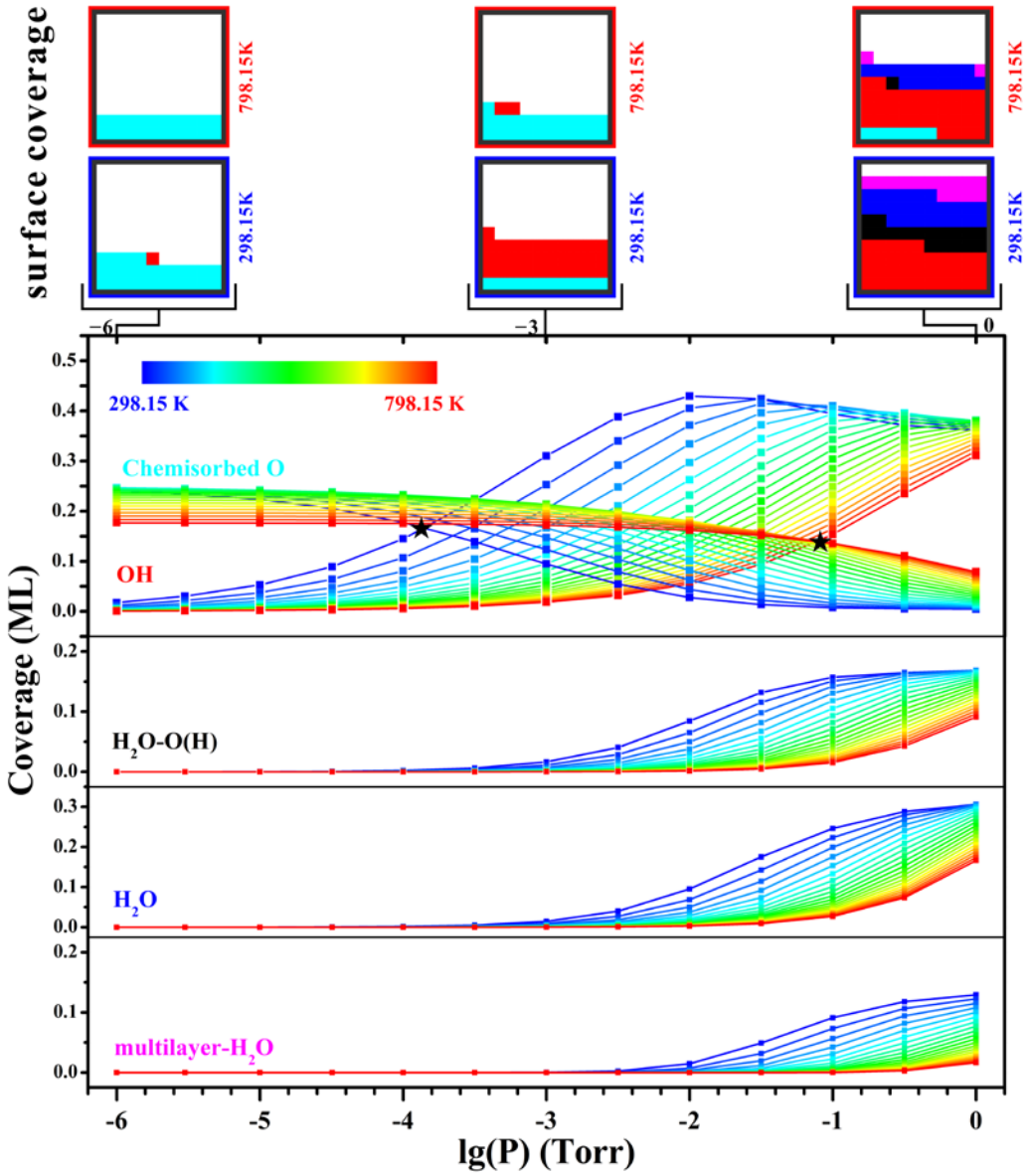

Figure 5-5 Overall predicted landscape taking consideration of both P and T.

Conclusion

Combining quantum mechanics to obtain binding free energies with CRN kinetics simulation to obtain the equilibrium concentrations as function of pressure and temperatures with QM

O1s chemical shifts to deconvolution the XPS experiments, we show a procedure that provides an atomic description compatible with the macroscopic observables. Theory and experiment are intertwined closely to provide the chemistry understanding, with both qualitative and quantitative agreements. In the presented system H_2O on Ag(111), we are able to explain the nature of all oxygen containing surface species, the free energy of these species, and pin down the kinetics and concentration profile of all the 5 oxygen containing surface species across a wide range of pressure and temperature (pressure from 10^{-6} torr to 1 torr, and temperature ranging from RT to 500ºC). We propose a new protocol that revolutionizes how we should interpolate spectrum data from the theory side, and it is cross-validated using experimental data. Because of its fundamental nature in thermodynamics and kinetic theory, this method should be malleable to be applied to a broad surface systems of interest.

Acknowledgement

This work was supported through the Office of Science, Office of Basic Energy Science (BES), of the US Department of Energy (DOE) under Award DE-SC0004993 to the Joint Center for Artificial Photosynthesis, DOE Energy Innovation Hubs. The Advanced Light Source is supported by the Director, Office of Science, Office of BES, of the US DOE under Contract DE-AC02-05CH11231. This work used the Extreme Science and Engineering Discovery Environment (XSEDE), which is supported by National Science Foundation grant number ACI-1548562. We thank Dr. Yufeng Huang and Samuel Clamons for their helpful discussions.

BIBLIOGRAPHY

(1) Cheng, Tao, Hai Xiao, and William A. Goddard III. "Reaction mechanisms for the electrochemical reduction of CO2 to CO and formate on the Cu (100) surface at 298 K from quantum mechanics free energy calculations with explicit water." *Journal of the American Chemical Society* 138, no. 42 (2016): 13802-13805.

(2) Favaro, Marco, Hai Xiao, Tao Cheng, William A. Goddard, Junko Yano, and Ethan J. Crumlin. "Subsurface oxide plays a critical role in CO2 activation by Cu (111) surfaces to form chemisorbed CO2, the first step in reduction of CO2." *Proceedings of the National Academy of Sciences* (2017): 201701405.

(3) Xiao, Hai, Tao Cheng, William A. Goddard III, and Ravishankar Sundararaman. "Mechanistic explanation of the pH dependence and onset potentials for hydrocarbon products from electrochemical reduction of CO on Cu (111)." *Journal of the American Chemical Society* 138, no. 2 (2016): 483-486.

(4) Hoshi, Nagahiro, Takeshi Mizumura, and Yoshio Hori. "Significant difference of the reduction rates of carbon dioxide between Pt (111) and Pt (110) single crystal electrodes." *Electrochimica acta* 40, no. 7 (1995): 883-887.

(5) Luc, Wesley, Charles Collins, Siwen Wang, Hongliang Xin, Kai He, Yijin Kang, and Feng Jiao. "Ag–Sn bimetallic catalyst with a core–shell structure for CO2 reduction." *Journal of the American Chemical Society* 139, no. 5 (2017): 1885-1893.

(6) Cheng, Tao, Yufeng Huang, Hai Xiao, and William A. Goddard III. "Predicted structures of the active sites responsible for the improved reduction of carbon dioxide by gold nanoparticles." *The journal of physical chemistry letters* 8, no. 14 (2017): 3317-3320.

(7) Reier, Tobias, Mehtap Oezaslan, and Peter Strasser. "Electrocatalytic oxygen evolution reaction (OER) on Ru, Ir, and Pt catalysts: a comparative study of nanoparticles and bulk materials." *Acs Catalysis* 2, no. 8 (2012): 1765-1772.

(8) Ikemiya, Norihito, and Andrew A. Gewirth. "Initial stages of water adsorption on Au surfaces." *Journal of the American Chemical Society* 119, no. 41 (1997): 9919-9920.

(9) Thiel, Patricia A., and Theodore E. Madey. "The interaction of water with solid surfaces: fundamental aspects." *Surface Science Reports* 7, no. 6-8 (1987): 211-385.

(10) Kolb, Dieter M., J. Lipkowski, and P. N. Ross. "Structure of electrified interfaces." *VCH, New York* (1993): 65.

(11) Kay, Bruce D., Keith R. Lykke, J. Randall Creighton, and Stephen J. Ward. "The influence of adsorbate–absorbate hydrogen bonding in molecular chemisorption: NH3, HF, and H2O on Au (111)." *The Journal of chemical physics* 91, no. 8 (1989): 5120-5121.

(12) Smith, R. Scott, C. Huang, E. K. L. Wong, and Bruce D. Kay. "Desorption and crystallization kinetics in nanoscale thin films of amorphous water ice." *Surface science* 367, no. 1 (1996): L13-L18.

(13) Löfgren, P., P. Ahlström, D. V. Chakarov, J. Lausmaa, and B. Kasemo. "Substrate dependent sublimation kinetics of mesoscopic ice films." *Surface science* 367, no. 1 (1996): L19-L25.

(14) Heras, J. M., and L. Viscido. "Work function changes upon water contamination of metal surfaces." *Applications of Surface Science* 4, no. 2 (1980): 238-241.

(15) Atkinson, S. J., C. R. Brundle, and M. W. Roberts. "Ultra-violet and X-ray photoelectron spectroscopy (UPS and XPS) of CO, CO 2, O 2 and H 2 O on molybdenum and gold films." *Faraday Discussions of the Chemical Society* 58 (1974): 62-79.

(16) Brundle, C. R., and M. W. Roberts. "Surface sensitivity of He I photoelectron spectroscopy (UPS) for H 2O adsorbed on gold." *Surface Science* 38 (1973): 234-236.

(17) Jablonski, A., F. Salvat, and C. J. Powell. "NIST electron elastic-scattering cross-section database." *NIST Standard Reference Database* 64 (2010).

(18) Kresse, Georg, and Jürgen Furthmüller. "Efficient iterative schemes for ab initio total-energy calculations using a plane-wave basis set." *Physical review B* 54, no. 16 (1996): 11169.

(19) Johnson, Erin R., and Axel D. Becke. "A post-Hartree-Fock model of intermolecular interactions: Inclusion of higher-order corrections." *The Journal of chemical physics* 124, no. 17 (2006): 174104.

(20) Grimme, Stefan, Jens Antony, Stephan Ehrlich, and Helge Krieg. "A consistent and accurate ab initio parametrization of density functional dispersion correction (DFT-D) for the 94 elements H-Pu." *The Journal of chemical physics* 132, no. 15 (2010): 154104.

(21) Kittel, C. "Introduction to Solid State Physics , Willey 2004." 978-0471415268.

(22) Soloveichik, David, Matthew Cook, Erik Winfree, and Jehoshua Bruck. "Computation with finite stochastic chemical reaction networks." *natural computing* 7, no. 4 (2008): 615-633.

(23) Grass, Michael E., Patrik G. Karlsson, Funda Aksoy, Måns Lundqvist, Björn Wannberg, Bongjin S. Mun, Zahid Hussain, and Zhi Liu. "New ambient pressure photoemission endstation at Advanced Light Source beamline 9.3. 2." *Review of Scientific Instruments* 81, no. 5 (2010): 053106.

(24) Phatak, Abhijit A., W. Nicholas Delgass, Fabio H. Ribeiro, and William F. Schneider. "Density functional theory comparison of water dissociation steps on Cu, Au, Ni, Pd, and Pt." *The Journal of Physical Chemistry C* 113, no. 17 (2009): 7269-7276.

(25) Wang, Shengguang, V. Petzold, Vladimir Tripkovic, Jesper Kleis, Jakob Geelmuyden Howalt, Egill Skulason, E. M. Fernandez et al. "Universal transition state scaling relations for (de) hydrogenation over transition metals." *Physical Chemistry Chemical Physics* 13, no. 46 (2011): 20760-2

Appendix A
Supplementary Information for Chapter 2

Table of Contents

Fig S2-1 to S2-6

Fig S2-1 Energy Level Diagram at 673K, 20atm using PBE functional

Fig S2-2 to S2-4 Transition state geometry and potential energy curves

Fig S2-5 Linear and zig-zag configuration

Fig S2-6 Energy Level Diagram at 730K, 200atm using PBE-D3 functional

Table S2-1

Table S2-1 Kinetic Monte Carlo results based on PBE DFT

Table S2-2 Comparison with previous theory results

Comparison with PBE results

This paper used the DFT/PBE functional including the Grimme empirical correction for London dispersion (van der Waals attraction) because this level of DFT in our recent calculations of ORR for Pt and CO2RR for Cu led to very close agreement with experiment (barriers to 0.05 eV and overpotentials to 0.05 V). However, we also carried out all calculation using just PBE with no D3 corrections (often the case for metallic systems). These calculations used the PBE optimized lattice parameters for Fe (PBE: a=2.827 Å, PBE-D3: a=2.807 Å, experiment at 300K a=2.867 Å, and experiment at 673K: a=2.881 Å).

Figure S2-1 shows the new energetics for PBE corresponding to Figure 2-2 in the text.

Using these modified energetics, we carried out the full set of kMC simulations, leading to Table S2-1, in place of Table 2-2 of the main text. For Somorjai conditions (673K) this predicts a TOF=89.3 compared to 17.7 for PBE-D3 and 9.7 experiment. This indicates that simple PBE may lead to rates that are too fast.

In particular, the poisoning effect of ammonia is substantially underestimated with PBE, with only a modest decrease of NH_3 production by increasing ammonia pressure. Thus

- the TOF changes from 89.3 to 75.7 NH_3mol/s/(2x2)surface area as the NH_3 pressure is increased from 1.5 torr to 1 atm at T=673 K, pH_2=15 atm, pN_2=5 atm; In contrast for

PBE-D3, the TOF changes from 17.7 to 2.8 NH_3mol/s/(2x2)surface area. The experiments by Somorjai suggest a change by a factor of ~3 from 1.5 torr to 20 torr.

- the TOF increases from 1983.5 to 1430.0 NH_3mol/s/(2x2) at T=730 K as conditions are changed from pH_2=150 atm, pN_2=50 atm, pNH_3=1 atm, to pH_2=120 atm, pN_2=40 atm, pNH_3=20 atm. In contrast for PBE-D3, the TOF changes from 93.7 to 18.6.
- However, the increase of ammonia production with temperature seems to be better predicted by PBE: from TOF=89.3 to 231.2 NH_3mol/s/(2x2) as the temperature is increased from 673 K to 730 K, under condition of pH_2=15 atm, pN_2=5 atm, pNH_3=1.5 torr. In contrast for PBE-D3, the TOF changes from 17.7 to 83.3. The experiments by Somorjai suggest a change by a factor of 2.4.

Overall, we conclude that theGrimme D3 dispersion correction with the Becke-Johnson parameters lead to a better description of the reaction energetics.

Table S2-1 lists the steady-state apparent ΔG (i.e., the logarithm of the relative populations) for the most important states obtained using PBE results in the kMC.

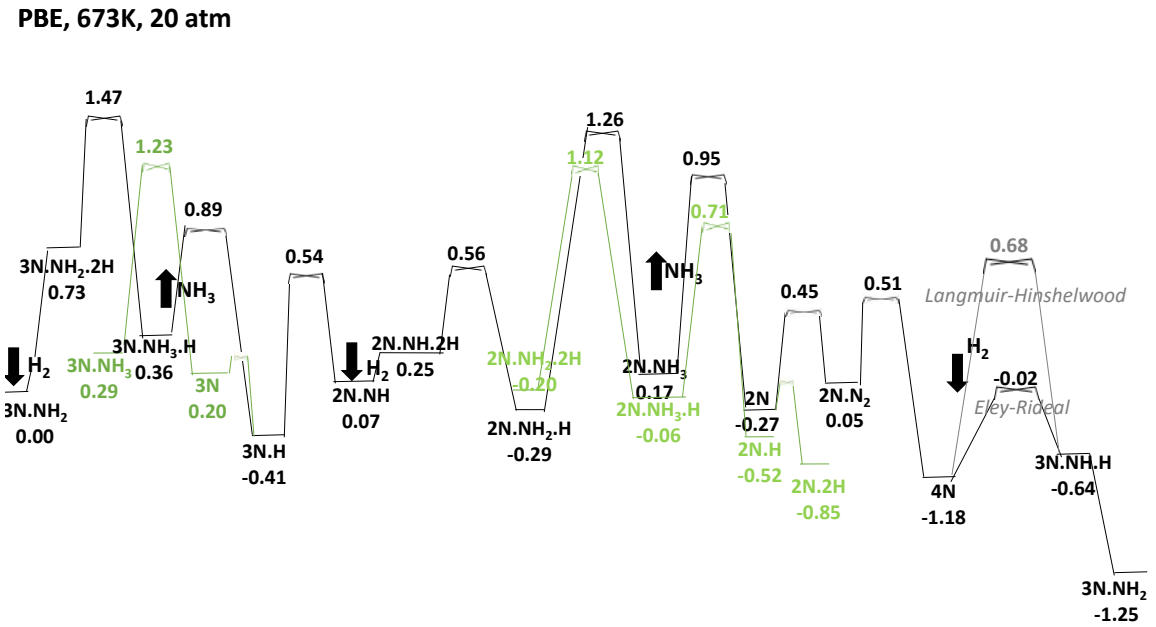

Figure S2-1. This is equivalent to Figure 2-2 of the text except using PBE rather than PBE-D3. We also use the PBE lattice parameter for bulk Fe. Energy landscape for NH_3 synthesis reactions under Somorjai condition, 673 ºK, 20atm. The lowest energy state 3N_NH_2 is taken as reference, with a free energy of zero. We considered the linear pathway in black and proposed alternative pathway in green, in order to lower some barriers. NH_3 production rate is dominated by 3 steps: N_2 adsorption, hydrogenation of NH_2, and NH_3 desorption. Note that we consider reacting 3 H_2 plus 1 N_2 to form 2 NH_3, so that the total free energy decreases by 1.25 eV as we go from 3N_NH_2 on the left to 3N_NH_2 on the right.

	T=673, pH_2=15, pN_2=5, pNH_3=1.5/760			T=730, pH_2=150, pN_2=50, pNH_3= 1			T=730, pH_2=120, pN_2=40, pNH_3=20		
configuration	t_i (%)	$-\ln(P_i/P_0)$	ΔG	t_i (%)	$-\ln(P_i/P_0)$	ΔG	t_i (%)	$-\ln(P_i/P_0)$	ΔG
3N_NH_2	32.7	0.00	0.00	29.7	0.00	0.00	38.4	0.00	0.00
3N_NH_2_2H	1E-4	0.73	0.73	7E-4	0.67	0.66	8E-4	0.68	0.68
3N_NH_3_H	8E-5	0.75	0.36	6E-3	0.53	0.27	0.14	0.35	0.29
3N_H	39.9	-0.01	-0.05	15.1	0.04	-0.22	16.8	0.05	-0.02
2N_NH	2E-2	0.43	0.43	1E-2	0.48	0.26	2E-2	0.49	0.46
2N_NH_2H	9E-4	0.61	0.61	3E-3	0.58	0.36	3E-3	0.60	0.58
2N_NH_2_H	10.7	0.06	0.07	18.1	0.03	-0.19	16.3	0.05	0.03
2N_NH_3	1E-4	0.73	0.53	6E-4	0.68	0.26	3E-3	0.60	0.48
2N	4E-4	0.65	0.45	8E-4	0.66	0.11	7E-4	0.69	0.51
4N	2.95	0.14	-0.46	0.73	0.23	-0.86	1.15	0.22	-0.86
3N_NH_H	1E-3	0.60	0.08	2E-3	0.60	-0.41	3E-3	0.60	-0.39
2N_2H_lin	9.4	0.07	-0.13	23.8	0.01	-0.56	17.4	0.05	-0.16
2N_2H	2.0	0.16	-0.04	4.15	0.12	-0.43	3.0	0.16	-0.03
2N_NH_3_H	1E-3	0.60	0.45	1E-2	0.49	-0.02	0.11	0.37	0.20
2N_H	3E-2	0.40	0.49	1E-1	0.36	-0.19	8E-2	0.39	0.21
2N_NH_2_2H	2.3	0.15	0.16	8.18	0.08	-0.14	6.6	0.11	0.10
kMC NH_3 mol/s/(2x2)	89.3			1983.5			1430.0		
total NH_3mol	148584			193826			172003		
3N_NH_3_H ↔ 3N_H	74312			96935			86021		
2N_NH_3_H ↔ 2N_H	74272			96891			85982		

Table S2-1. Kinetic Monte Carlo results based on PBE DFT (without the D3 London dispersion correction). For Somorjai conditions (673K) this predicts a TOF=89.3 compared to 17.7 for PBE-D3 and 9.7 experiment. Top rows – Per cent of populations (i.e., residence times) = t_i(%), apparent free energy differences [evaluated as minus the logarithm of ratio of populations = P_i/P_0, where P_0 = P_{3N_NH2}], and thermodynamic free energy differences (ΔG) for selected configurations in a Fe(111)-(2x2) unit cell under steady-state of ammonia synthesis as predicted by kMC simulations at different temperatures (673 and 730 K), and different H_2, N_2, NH_3 pressures, using DFT/PBE data instead of DFT/PBE-D3 data as in Table 2-2 of the main text. All configurations are assumed in the zig-zag arrangement, except for "2N_2H_lin" which is linear (see SI for details). Temperature in Kelvin, pressure in atmospheres, free energy differences in eV. Bottom rows – NH_3 molecules

produced per second per (2x2) unit cell under the given conditions [NH_3mol/s/(2x2)], total number of NH_3 molecules produced in the kMC runs (total NH_3mol), further partitioned into the 2 main steps involving NH_3 adsorption/desorption: 3N_NH_3_H ↔ 3N_H; 2N_NH_3_H ↔ 2N_H

Transition state geometry and potential energy curves

The Transition state geometries and potential energy curves are reported in Figure S2-2 to S2-4

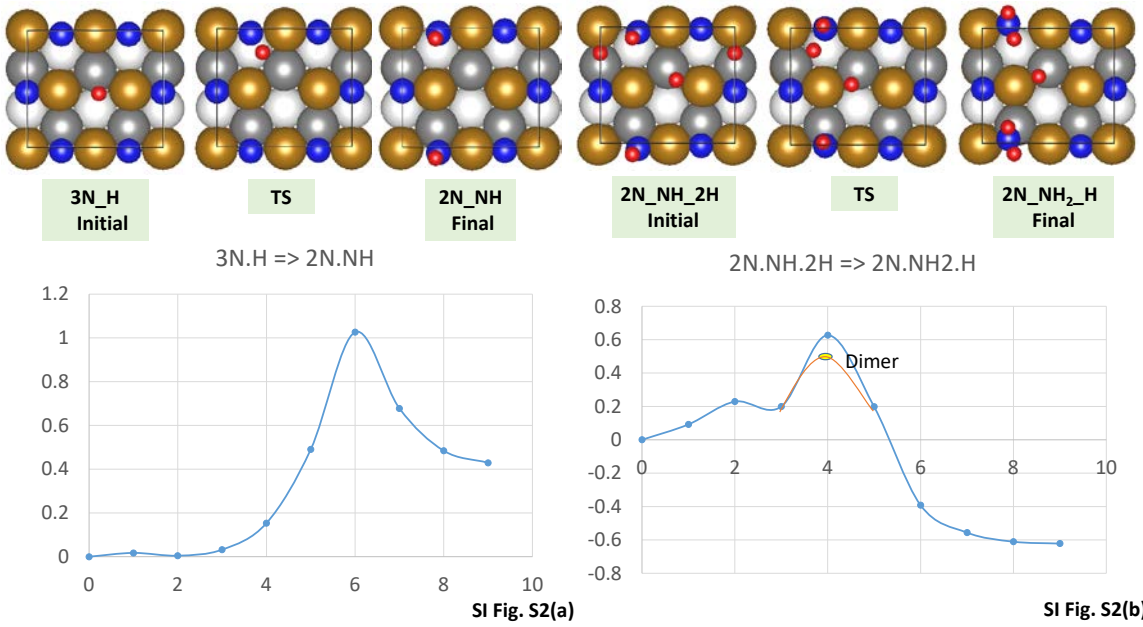

Figure S2-2. Mechanism for 3N_H =>2N_NH, migration of hydrogen and addition to N on the surface (LH) is shown in a). Mechanism for 2N_NH_2H => 2N_NH_2_H, hydrogen migration and addition to NH on the surface (LH) is shown in b). The climbing NEB method generates a true transition state, as we confirmed by performing vibrational frequency calculations showing a single negative curvature in the Hessian. The dimer calculations were performed if the negative frequency was found from NEB transition state image.

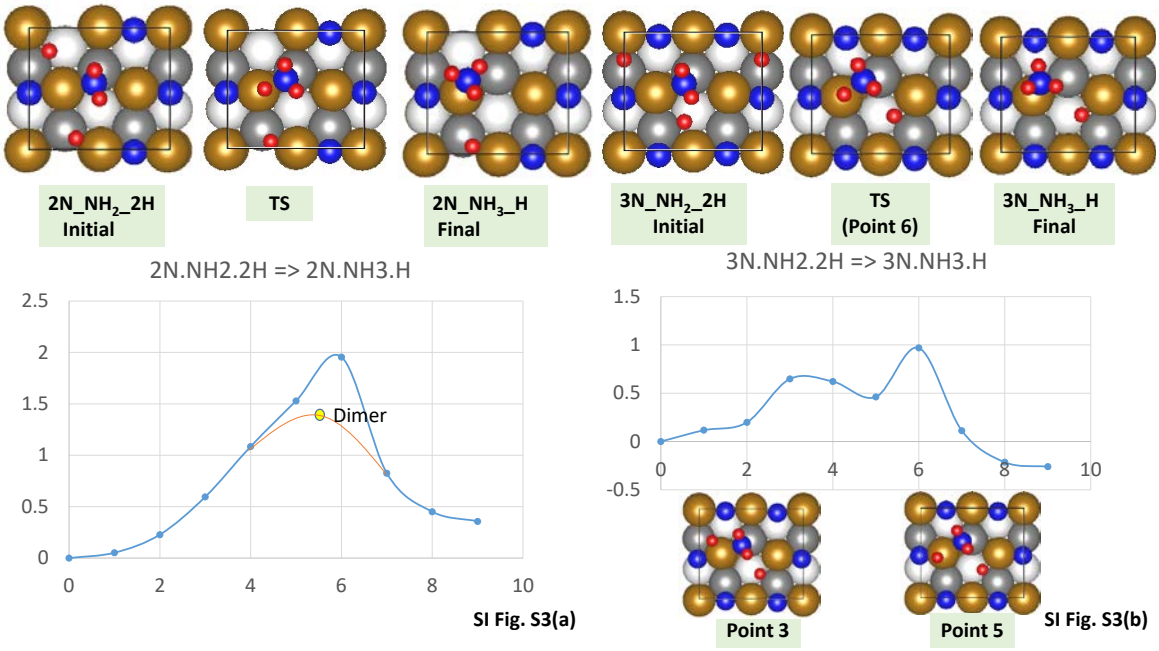

Figure S2-3. Mechanism for 3N_NH_2_2H => 3N_NH_3_H, hydrogen migration and addition to NH_2 on the surface (LH) is shown in a). Mechanism for 2N_NH_2_2H => 2N_NH_3_H, hydrogen migration and addition to NH_2 on the surface (LH) is shown in b). The climbing NEB method generates a true transition state, as we confirmed by performing vibrational frequency calculations showing a single negative curvature in the Hessian. The dimer calculations were performed if the negative frequency was found from NEB transition state image.

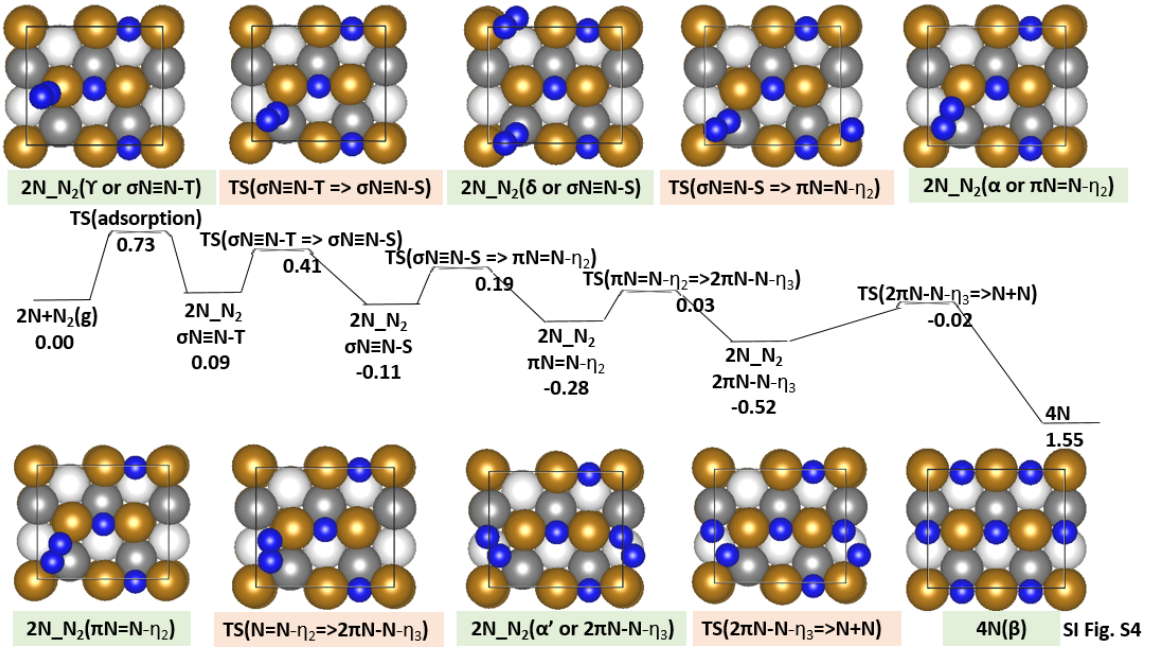

Fig S2-4. Mechanism for N_2 dissociation is purposed to be triple-bonded N_2 adsorbed on the first layer (denoted as N^3N-T phase, the superscription in the middle represents the bond order, and T represents adsorption on top layer) => triple-bonded N_2 adsorbed on the second layer (denoted as N^3N-S phase) => double-bonded N_2 on two-fold site (denoted as N^2N-η_2 phase) => single-bonded N_2 on three-fold site (denoted as N^1N-η_3 phase) => dissociative 4N.

Linear versus zig-zag configurations

For each stoichiometry of the system, there can be more than one possible configuration. Thus consider the 4 bridge sites of the (2x2) unit cell. If 2 or more different species are adsorbed on these, sites there can be at least two alternative configurations, which we name "linear" and "zig-zag", as illustrated in Figure S2-5 for the "2N" system. Indeed, for most stoichiometries the "linear" configuration is lower in energy than the "zig-zag" one, but only the "2N zig-zag" configuration is able to dissociate N_2. Thus most of our discussions report only zig-zag configurations. An exception is for "2N_2H_lin" which is linear and is reported in Table 2-2 and Table S2-1 due to its abundance (high population) under steady state conditions.

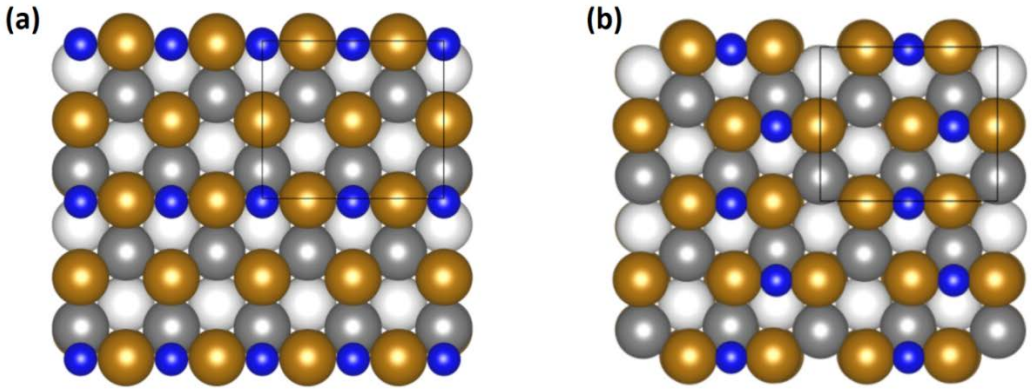

Figure S2-5. Schematic illustration of: (a) "linear" and (b) "zig-zag" configurations for the "2N" system. The (2x2) unit cell is replicated 4 time for better visualization.

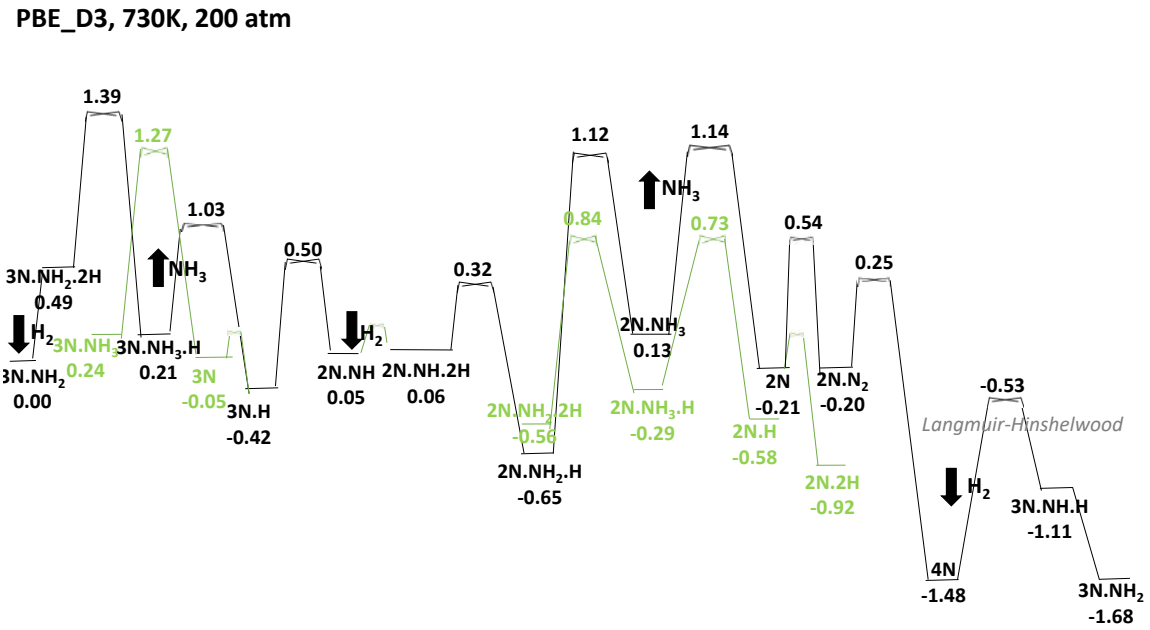

Fig S2-6. This is equivalent to Figure 2-2 of the text except using 730K , 200 atm instead of 673K, 20 atm. The lowest energy state 3N_NH_2 is taken as reference, with a free energy of zero. We considered the linear pathway in black and proposed alternative pathway in green. NH_3 production rate is dominated by 3 steps: N_2 adsorption, hydrogenation of NH_2, and NH_3 desorption. Note that we consider reacting 3 H_2 plus 1 N_2 to form 2 NH_3, so that the total free energy decreases by 1.68 eV as we go from 3N_NH_2 on the left to 3N_NH_2 on the right.

States	Description	rN-N	Ead (present)	covergae (present)	Norskov	coverage (Noskov)	Lin	coverage (Lin)

γ	top vertical (1st layer)	1.13	-0.62	0.25	-0.400	1.00	NA	NA
δ	top vertical (2nd layer)	1.16	-0.72	0.25	-0.150	1.00	NA	NA
α	2-fold site	1.20	-0.84	0.25	-0.500	1.00	NA	NA
α'	3-fold site	1.33	-0.67	0.25	-0.250	1.00	NA	NA
β	dissociated N	4.02	-1.56	0.25	-1.400	1.00	-1.696	0.33
NH	TTS site	NA	-4.59	0.25	NA	NA	-4.182	0.33
NH2	TS site	NA	-3.31	0.25	NA	NA	-2.811	0.33
NH3	T site	NA	-0.93	0.25	NA	NA	-0.705	0.33

Table S2-2 Comparison of dissociatively chemisorbed binding energies for N2, with Mortensen et al.[50] Different adsorption states are labeled as α, β, γ. Comparison of different chemisorbed species binding energies with Lin et.al.[41]

Instructions on excel file containing full numerical data

Overview

Excel sheet "HB_111_Apr24" contains all calculations mentioned in this paper.

It is divided into 4 sub-sheets, namely

- "ENERGY_COMPILE_673K",

This sheet has two complete sets of 53 intermediate states' energy using PBE and PBE-D3 functionals at 673 K, Somorjai condition.

- "ENERGY_COMPILE_730K",

This sheet has two complete sets of 53 intermediate states' energy using PBE and PBE-D3 functionals at 730 K, industrial condition.

- "Small Molecule",

This sheet has two sets of molecular energy using PBE and PBE-D3 functionals at both 673 K and 730 K,

- "Reaction_Barriers",

This sheet has NEB electronic energy of all crucial reaction barriers along the NH_3 production pathway.

Detailed Explanation and Instruction

"ENERGY_COMPILE_673K" and "ENERGY_COMPILE_730K" are parallel of each other, and we have the relative energy in Column J and M to plot Figure 2-2 in the text, Figure S2-1 and S2-6 in SI. Both sheets read data from "Small Molecule" and "Reaction_Barriers" because free energy is dependent upon temperature and pressure.

Currently, “ENERGY_COMPILE_673K” reflects Somorjai experiment condition: 15 atm pressure for H_2, 5 atm for N_2 and 1.5 torr for NH_3. Electronic energy of these small molecules and 53 intermediate states (column H and K) were calculated from VASP, and they are independent of pressure and temperature. On the other hand, free energy (column I and L) depends on temperature and pressure, thus need to be carefully selected from “Small Molecule” and “Reaction_Barriers”. Column J and M are dG calculated using PBE and PBE-D3 functionals respectively, and they are referenced to the lowest energy state $3N.NH_2$. Each time 1 NH_3 is produced, we subtracted the free energy of ammonia. Column H-J are PBE values using PBE lattice parameter 2.820 Å, Column K-M are PBE-D3 values using PBE_D3 lattice parameter 2.807 Å. We have also considered using experiment lattice parameter of iron at 673K, which is 2.881 Å, from Column N to P, and they give very similar answers to PBE-D3 lattice parameter results (Column K-M), within ~0.1 eV in difference.

Similarly, “ENERGY_COMPILE_730K” reflects industrial condition of producing NH_3: 150 atm pressure for H_2, 50 atm for N_2 and 1.5 torr for NH_3. The layout of this sheet is exactly the same as “ENERGY_COMPILE_673K”.

“Small Molecule” contains electronic energy of N_2, H_2, NH_3 calculated using VASP, PBE and PBE-D3 functionals, and free energy corrections calculated from Jaguar. Free energy corrections include zero point energy (ZPE), Enthalpy, and Entropy (see Column D-G). These energies are raw output from Jaguar. ZPE and Enthalpy are in the unit of Kcal/mol, and entropy is in the unit of cal/mol. For details of rotational, translational and vibrational contributions of each section, user can refer to Row 1-27. Pressure dependence is added by assuming ideal gas, using RT*ln(P2/P1). User can choose any pressure they like by adjusting Column C. “ENERGY_COMPILE_673K” and “ENERGY_COMPILE_730K” will automatically reflect the pressure preference.

“Reaction_Barriers” contains NEB electronic energy of important reaction barriers and along the pathway we purposed in the text. For hydrogenation step and N_2 dissociation step, we used NEB climb to find transition state, if more than one negative frequencies are found, we used dimer method to pinpoint the real transition state. Please refer to Column A-C and picture illustrations within the sheet for NEB energy potential curve. We used electronic adsorption energy+ZPE, for desorption and adsorption barriers for NH_3 and N_2, and please refer to column K-T for them.

User can opt to switch between 673 K and 730 K by selecting and linking the appropriate rows in “Small Molecule” and “Reaction_Barriers”. User can select any pressure according to their need, by typing in the pressure in column C of “Small Molecule”, in the unit of atm.

Example

Currently "ENERGY_COMPILE_673K" reflects Somorjai experiment condition: 15 atm pressure for H_2, 5 atm for N_2 and 1.5 torr for NH_3, and here's a screen print of the intermediate and small molecules' energy.

G	H	I	J	K	L	M	N	O	P
	PBE	PBE	PBE	PBE_D3_2.807	PBE_D3_2.807	PBE_D3_2.807	PBE_D3_2.881	PBE_D3_2.881	PBE_D3_2.881
Name	E(tot)	G	dG	E(tot)	G	dG	E(tot)	G	dG
H2(673K,15atm)	-6.76	-7.20		-6.77	-7.22			-7.22	
N2(673K,5atm)	-16.60	-17.66		-16.65	-17.71			-17.71	
NH3(673K,1.5 torr)	-19.52	-20.25	-1.25	-19.54	-20.29	-1.22		-19.94	-0.51
3N.NH2	-224.10	-224.34	0.00	-230.00	-231.40	0.00	-229.92	-230.19	0.00
3N.NH2.2H	-230.91	-230.80	0.73	-237.03	-238.05	0.57	-237.02	-236.95	0.46
TS_3N.NH2.2H	-230.09	-230.06	1.47	-236.05	-237.15	1.47			N/A
3N.NH3.H	-231.24	-231.17	0.36	-237.29	-238.32	0.30			N/A
TS_NH3desorption	(Ead = 0.63)	-0.10 from ZPE'	0.89	(Ead = 0.925)	-0.10 from ZPE'	1.12			N/A
3N.H+NH3(g)	-211.10	-211.70	-0.41	-216.82	-218.59	-0.26			N/A
TS_3N.H+NH3(g)	-210.24	-210.75	0.54	-215.79	-217.67	0.66			N/A
2N.NH_diagonal+NH3(g)	-210.76	-211.22	0.07	-216.39	-218.11	0.22			N/A
2N.NH.2H+NH3(g)	-218.10	-218.23	0.25	-223.91	-225.24	0.30			N/A
TS_2N.2H.NH+NH3(g)	-217.53	-217.93	0.56	-223.48	-224.99	0.56			N/A
2N_diagonal.NH2.H+NH3(g)	-218.68	-218.78	-0.29	-224.53	-225.94	-0.39			N/A
TS_2N_diagonal.H.NH2+NH3(g)	-217.09	-217.23	1.26	-222.84	-224.18	1.36			N/A
2N_diagonal.NH3+NH3(g)	-218.20	-218.32	0.17	-223.84	-225.16	0.39	-223.90	-223.91	0.78
TS_NH3desorption	(Ead = 0.88)	-0.10 from ZPE'	0.95	(Ead =1.111)	-0.10 from ZPE'	1.40	(Ead = 1.10)		1.88
2N_diagonal+2NH3(g)	-197.81	-198.51	-0.27	-203.21	-205.14	0.11	-203.28	-203.96	0.79
2N.N2(v.diagonal)+2NH3(g)	-214.86	-215.85	0.05	-220.64	-222.76	0.20			N/A

If the user is curious at energy landscape of high pressure condition, say 150 atm pressure for H_2, 50 atm for N_2 and 1 atm for NH_3, the user need to go to column C of "Small Molecule" and the notation in "ENERGY_COMPILE_673K". Sheet "ENERGY_COMPILE_673K" will automatically reflect the change.

Here's a screen print of the intermediate and small molecules' energy at 150 atm pressure for H_2, 50 atm for N_2 and 1 atm for NH_3.

G	H	I	J	K	L	M	N	O	P
	PBE	PBE	PBE	PBE_D3_2.807	PBE_D3_2.807	PBE_D3_2.807	PBE_D3_2.881	PBE_D3_2.881	PBE_D3_2.881
Name	E(tot)	G	dG	E(tot)	G	dG	E(tot)	G	dG
H2(673K,150atm)	-6.76	-7.06		-6.77	-7.08			-7.08	
N2(673K,50atm)	-16.60	-17.52		-16.65	-17.57			-17.57	
NH3(673K,1 atm)	-19.52	-19.88	-1.06	-19.54	-19.94	-1.05		-19.94	-1.05
3N.NH2	-224.10	-224.34	0.00	-230.00	-231.40	0.00	-229.92	-230.19	0.00
3N.NH2.2H	-230.91	-230.80	0.60	-237.03	-238.05	0.43	-237.02	-236.95	0.33
TS_3N.NH2.2H	-230.09	-230.06	1.34	-236.05	-237.15	1.34			N/A
3N.NH3.H	-231.24	-231.17	0.23	-237.29	-238.32	0.16			N/A
TS_NH3desorption	(Ead = 0.63)	-0.10 from ZPE'	0.76	(Ead = 0.925)	-0.10 from ZPE'	0.99			N/A
3N.H+NH3(g)	-211.10	-211.70	-0.18	-216.82	-218.59	-0.04			N/A
TS_3N.H+NH3(g)	-210.24	-210.75	0.76	-215.79	-217.67	0.88			N/A
2N.NH_diagonal+NH3(g)	-210.76	-211.22	0.30	-216.39	-218.11	0.44			N/A
2N.NH.2H+NH3(g)	-218.10	-218.23	0.35	-223.91	-225.24	0.39			N/A
TS_2N.2H.NH+NH3(g)	-217.53	-217.93	0.65	-223.48	-224.99	0.64			N/A
2N_diagonal.NH2.H+NH3(g)	-218.68	-218.78	-0.20	-224.53	-225.94	-0.30			N/A
TS_2N_diagonal.H.NH2+NH3(g)	-217.09	-217.23	1.35	-222.84	-224.18	1.45			N/A
2N_diagonal.NH3+NH3(g)	-218.20	-218.32	0.26	-223.84	-225.16	0.47	-223.90	-223.91	0.51
TS_NH3desorption	(Ead = 0.88)	-0.10 from ZPE'	1.04	(Ead =1.111)	-0.10 from ZPE'	1.49	(Ead = 1.10)		1.61
2N_diagonal+2NH3(g)	-197.81	-198.51	0.19	-203.21	-205.14	0.55	-203.28	-203.96	0.52
2N.N2(v.diagonal)+2NH3(g)	-214.86	-215.85	0.37	-220.64	-222.76	0.51			N/A

How to obtain rates to be used in the kMC simulations

As discussed in the main text, we evaluated forward and backward rates connecting two different states using transition state theory as $(k_BT/h)\exp(-\Delta G\dagger/k_BT)$, where k_B is the

Boltzmann constant, T is the temperature, h is the Planck constant, $\Delta G\dagger$ is the difference in free energy between the starting state and the saddle point. In the case of ER reactions involving gas-phase species turning into adsorbates, we again use transition state theory, but for the reverse desorption process, and then we invoke microscopic reversibility principle to calculate the rate of the direct process.

Appendix B
Supplementary Information for Chapter 3

Supplementary Materials

Figure S3-1 Complete sampling of possible states.

Figure S3-2 Pictorial illustration of reaction pathway for two sets of Co doped structures.

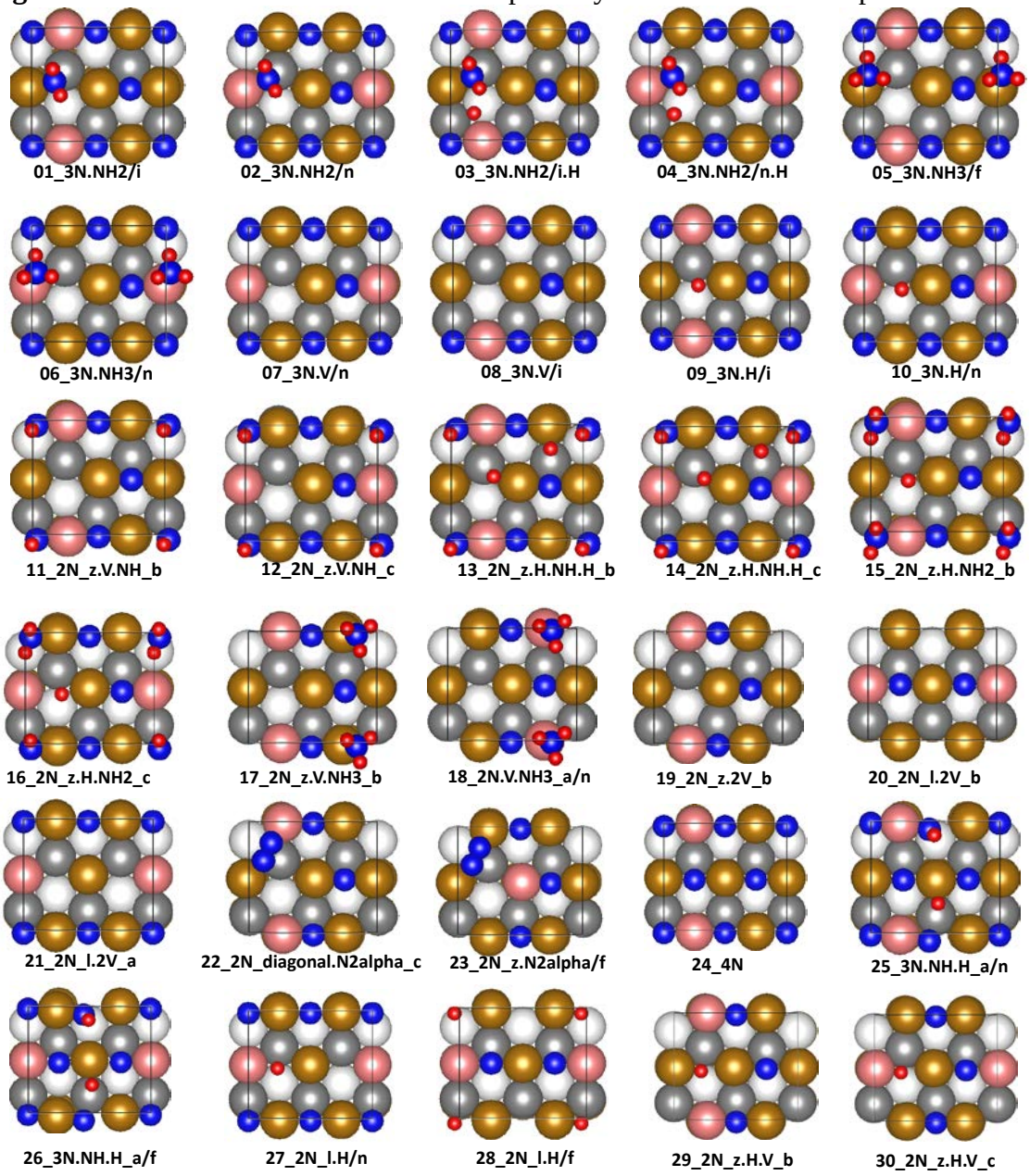

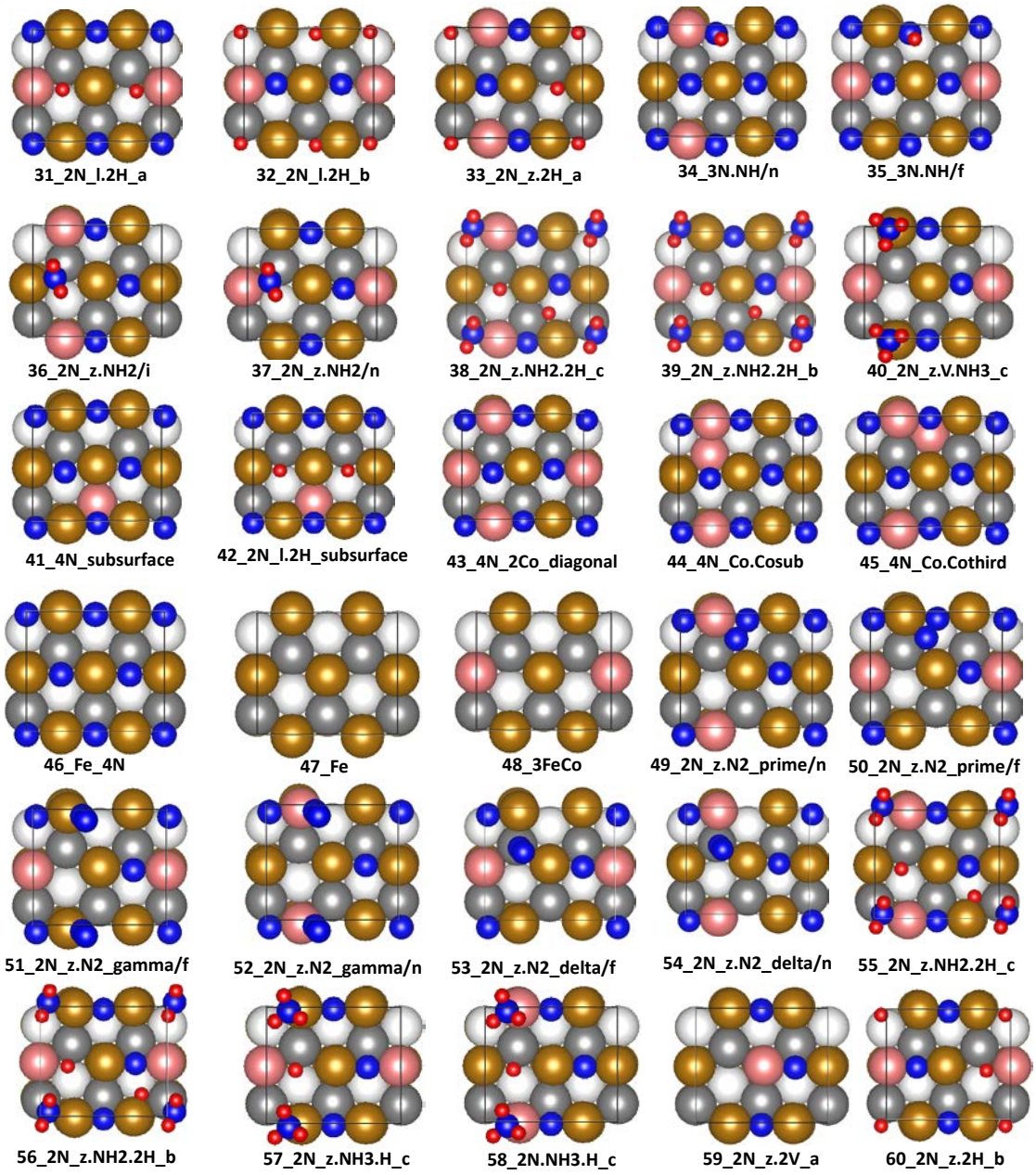

Figure S3-1. Complete sample of possible states. All structures are named based on our nomenclature in main text Table 3-1. Out of 60 structures, 40(with name and energetics in main text Table 3-2 are used in studying the mechanism of Haber Bosch mechanism. Out of the remaining 20 cases, such as 41-38 are useful for studying stabilities of Co atoms and the stabilities of double dopants.

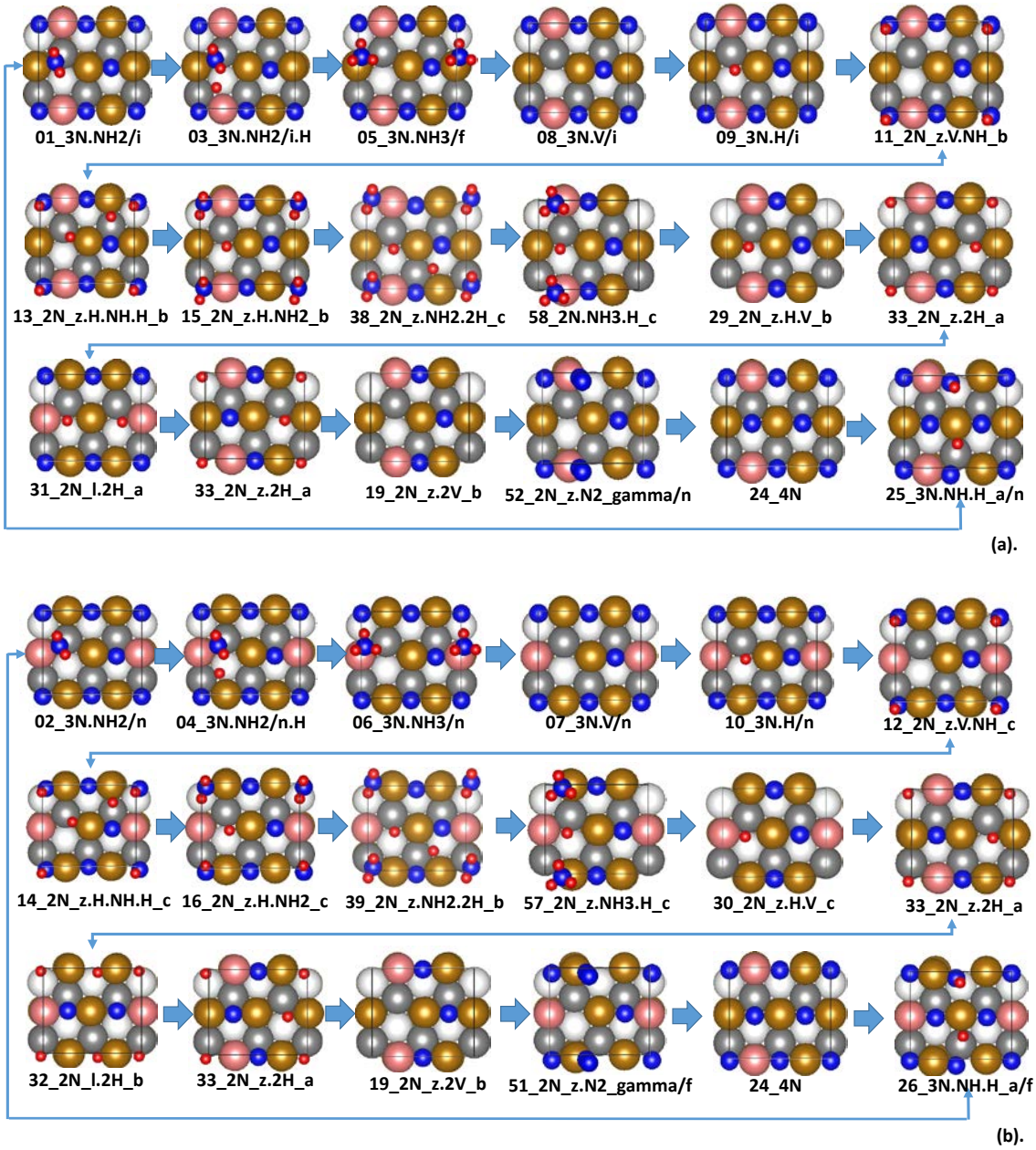

Figure S3-2a) and S3-2b). Pictorial illustration of reaction pathway for two sets of Co doped structures. Whereas figure a). has the initial surface species NH_2 far from Co dopant and figure b). has the initial surface species NH_2 near Co dopant. Energetics of the intermediate states along the pathway, including transition state is given in Table 3-2 and Figure 3-2 in main text.

Appendix C
Supplementary Information for Chapter 4

1. Supplementary Methods

1.1 QM Methods:

1.1.1 Surface Optimization

The PBE-D3(BJ) level of DFT leads to a calculated lattice parameter of a = 4.012 Å for the bulk Ag structure at 0°K, slightly smaller than the experimental value 4.085 Å at 298°K[1]. We used experimental lattice parameter 4.085 Å to construct a two-dimensional periodic slab with four layers of Ag atoms each of which consists of a (4 x4) unit cell (16 surface Ag per cell). We include 15 Å of vacuum in the z direction to minimize possible interactions between the replicated cells. The top two layers are relaxed while the bottom layers are kept fixed.

All calculations were carried out with the VASP[2] software package. We established that an energy cutoff of 500eV leads to converged forces. The K-point sampling was chosen to be 3 x 3 x 1. All calculations include spin-polarization. We used the Perdew-Burke-Ernzerhof (PBE) flavor of Density Functional theory (DFT), including the D3 (Becke Johnson) [3] empirical corrections for long range London dispersion (van der Waals attraction)[4].

This level of QM has been validated recently for several systems. Thus reference[5] carried out systematic studies for the oxygen reduction reaction (ORR, O_2 + protons → H_2O) on Pt(111) using the same PBE-D3 level as in this paper. Including 5 layers of explicit solvent in QM metadynamics on all reaction steps, comparisons could be made to experimental activation barriers for two values of the external potential. In both cases the calculated activation barriers were within 0.05 eV of the experiment[6-9].

Previous calculations for the CO_2 reduction reaction on Cu(100) using the same level of theory obtain an activation energy within 0.05 eV of experiment. This same level of theory has also led to similar accuracy for the oxygen evolution reaction on IrO_2 and for onset potentials on Cu(111) [10-12].

1.1.2 Small Gas Molecules

Calculations for the gas phase molecules used the PBE functional (as implemented in Jaguar) with the D3 empirical correction for London dispersion[13]. To obtain the total free energy, G=H-TS, for the gas molecules at temperature T, we add to the DFT electronic energy (E), the zero-point energy (ZPE) from the vibrational levels (described as simple

harmonic oscillators), and the specific heat corrections in the enthalpy from 0 to T. The entropy (S), as a sum of vibrational, rotational and translational contributions, are evaluated from the same levels. To correct the free energy for pressure, we assume an ideal gas and add $RT*\ln(P_2/P_1)$ with a reference pressure of P= 1 atm. For example, CO_2 gas at room temperature and 1atm would have a free energy correction of -0.25eV, including ZPE (0.32eV), translational entropy contribution (-0.42eV), rotational entropy contribution (-0.15eV) and almost negligible vibrational entropy contribution (-0.003eV). All calculations assume the current experimental condition: $P(CO_2)$ = 300 mtorr, and $P(H_2O)$ = 150 mtorr.

1.1.3 Free Energy of Equilibrium Configurations

After the gas molecules the adsorbed on metal surface, their rotational and translational degrees of freedom are reduced to vibrational modes. The vibrational frequencies for surface adsorbents are calculated by allowing the adsorbed molecules and the top layer of metal to relax, with the bottom layers fixed. For these phonon calculations we used 10^{-6} eV energy convergence threshold to obtain reliable phonon frequencies (no negative eigenvalues.) To obtain the Free energy, G=H-TS, for the various equilibrium configurations, we used density functional perturbation theory (DFPT) to calculate the phonon density of states, which was used to calculate the ZPE, the temperature correction to the enthalpy, and the vibrational contributions to the entropy.

1.1.4 Core Level Shift Calculations

There are two ways of calculating the change in core level energies implemented in VASP[2]. The simpler option (ICORELEVEL = 1) calculates the core levels in the initial state approximation, which involves recalculating the KS eigenvalues of the core states after a self-consistent calculation of the valence charge density. The second option (ICORELEVEL = 2) is more involved. In this case, electrons are removed from the core and placed into the valence. Our previous studies found that the ICORELEVEL =1 leads to relative binding energy shift in good agreement with experimental XPS[14], so we use this approach here.

1.2 Ambient Pressure XPS Measurements:

Ambient pressure XPS measurements were performed at Beamline 9.3.2 of the Advanced Light Source, Lawrence Berkeley National Laboratory. The beamline has station consisted of a load lock chamber with base pressure of ~5×10^{-8} Torr for sample loading; a preparation chamber with base pressure of ~$\times10^{-9}$ Torr for sample preparation,

and a main chamber for sample characterization under ambient pressure condition. The beamline provides beams with a photon energy range of 200-800 eV.

The clean surface of pristine Ag foil was obtained in the preparation chamber, by repeated argon sputtering (2keV, 60mins) and vacuum annealing (900 K, 60mins). No carbon- and oxygen- based contaminations were detected on the sample surface. The oxygen covered Ag surfaces were prepared by annealing the samples at 430 K at 40mTorr O_2 for 5mins, and 60 mTorr O_2 for 15mins.

During the APXPS measurements performed at 298K, CO_2 partial pressure was kept at 0.3 Torr for CO_2 adsorption, whereas the total pressure was kept at 0.45 Torr with 0.3 Torr CO_2 and 0.15 Torr H_2O. The purities of the dosing gases (CO_2, H_2O) were *in-situ* monitored by a conventional quadrupole mass spectrometer to ensure no additional gas crosscontamination (especially, the CO and H_2 gases).

2. Discussion of the subsurface oxygen in Cu system.

In a recent study performed by Garza et al., the stability of subsurface oxygen in Cu is questioned[15]. Thus, we want to further clarify the Cu results by comparing the differences and consistencies between our previous work with Garza's.

We are interested in the existence of both subsurface and surface oxygen on Cu surface. Our previous QM calculations on Cu used the advanced M06 version of DFT theory that is optimized to describe both van der Waals attraction and reaction pathways, whereas Garza et al. used the semiempircally modified PBE method for oxygen and the SCAN+rVV10 functional for physisorption of CO_2 with copper. Our previous QM calculations were carried at experimental condition with gas phase CO_2 and H_2O (total pressure 0.7 torr, and room temperature), which could be directly compared to this current manuscript. On the other hand, Garza et.al carried out the calculation with electrolyte and external potential, which is valuable but not directly comparable.

Our work calculated the free energy of binding of the various species showing the stability of the various species under the experimental pressures and temperatures. This led to excellent agreement with the APXPS chemical shifts. The experimental evidence of subsurface oxide is quite clear from the O1s spectra characterizations. Also, the experimental results of adding additional O experimentally confirmed our QM predictions.

Even so, there are some consistencies between Garza's work and our work. We both found that the *b*-CO_2 can only be stable with extra charge transferred to CO_2 to change the molecule structure. While the M06 DFT finds subsurface O changes the Cu valence state to provide extra charge, Garza applied an external potential that can provide extra charge that stabilized the bent configuration. Although our Cu experimental data does not represent the environment under applied potential, it shows that extra charge can stabilize the *b*-CO_2 with H_2O together with the theory.

Summarizing. The previous experiments prove the existence of subsurface O that the M06 DFT also finds and the QM and APXPS are fully consistent.

3. Stability and properties of adsorbates on Ag

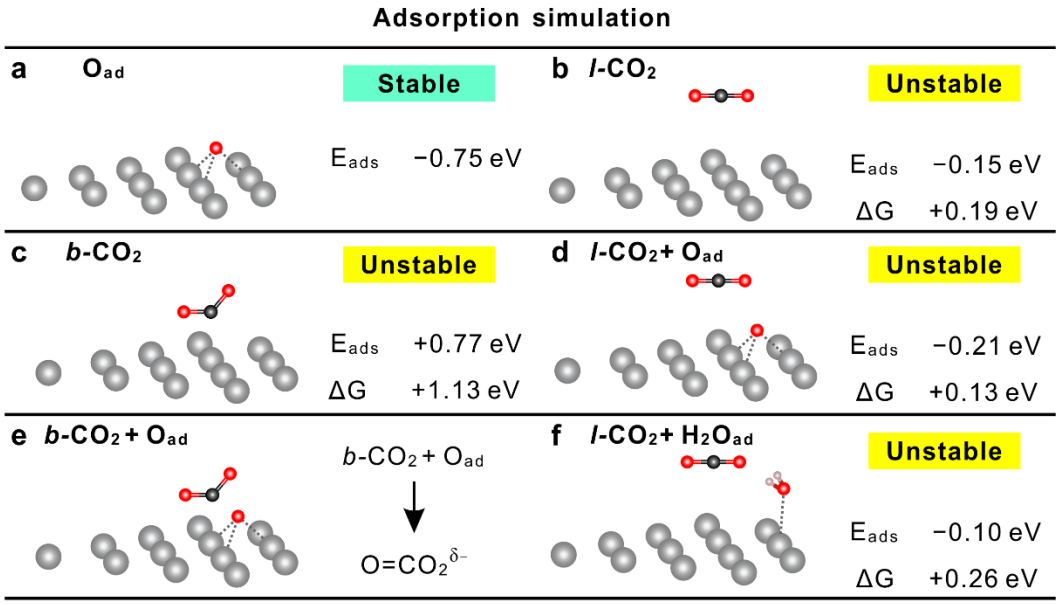

Figure S4-1. The QM predictions of adsorbates on the Ag surface. a, Surface O adsorbed (O_{ad}) on Ag surface on-top three-fold (η_3) site. **b,c,** The optimized structure for *l*- and *b*- CO_2 on pristine Ag surface. Both *l*- and *b*- CO_2 are found to be unfavorable with E_{ads} = −0.15 eV and ΔG = +0.19 eV, and E_{ads} = +0.77 eV and ΔG = +1.13 eV, respectively. **d,** The optimized structure of *l*-CO_2 on Ag surface in the presence of isolated surface O_{ad}. This configuration is found to be unfavorable with ΔE_{ads} = −0.21 eV, but ΔG = +0.13 eV. Thus a pressure of ~30 Torr would be required to stabilize *l*-CO_2 on the O/Ag surface at 298 K. **e,** The optimized structure of *b*-CO_2 on Ag surface in the presence of isolated surface O_{ad}. *b*-CO_2 interact with the on-top surface O_{ad} atoms to form a chemisorbed surface carbonic acid-like $O{=}CO_2^{\delta-}$ species as shown in main text **Figure 4-1c and 4-2a**. **f.** The optimized structure of *l*-CO_2 on Ag surface in the presence of surface H_2O. We find that (*l*-CO_2)-(H_2O) remains unstable on Ag surface (E_{ads} = −0.10 eV and ΔG = +0.26 eV), even with the help of H_2O. The hydrogen, carbon, oxygen, and silver atoms were represented with rosy brown, black, red, and gray balls, respectively.

O on Ag surface

We find that sublayer O (which stabilized both the *l*- and *b*- CO_2 in Cu system) is not stable on Ag, quantum mechanics (QM) finds that putting an O in a Ag sublayer site goes without a barrier to an on-top three-fold (η_3) site (Ag-O = 2.14 Å) with ΔE = −1.46 eV. Previous studies included some discussion on the subsurface O in the Ag system, which is introduced by through the grain boundary, defects in the structure, and diffusion of the surface oxygen into the bulk. These cases required moderate to high temperature and high oxygen coverage[16,17]. Moreover, Li et al. performed a series of studies examining the stability of subsurface oxygen in Ag and found that the transition barrier from surface oxygen to subsurface oxygen on Ag(111) surface is +0.86eV, whereas the reverse barrier from subsurface to surface oxygen is only +0.18eV, leading to the population of surface oxygen

is around exp(34)=5.8×10^{14}, which is around 10^{14} times more than subsurface oxygen[18]. It is found that crystal expansion is needed to stable subsurface oxygen, where the high oxygen coverage is needed[19,20].

l-CO_2 on Ag surface

The optimized structure for physisorbed CO_2 on the clean surface has an O-C-O angle of 180° with 1.177Å CO bonds, essentially the same for the PBE-D3 calculation on gas phase CO_2 (1.176Å). This linear CO_2, denoted *l*-CO_2, is physisorbed parallel to the Ag surface, at a height of 3.08Å above Ag surface (**Figure S4-1b**). The calculated QM adsorption energy is ΔE_{ads} = −0.15 eV. Including the phonon corrections for zero-point energy (ZPE) and pressure leads to a free energy of ΔG_{298} = +0.19 eV, so this state is not observed in our experiments. The core levels are C1s = 270.82 eV and O1s = 509.70 eV. These energetics would require a CO_2 pressure of ~500 Torr for the *l*-CO_2 be stabilized on the clean Ag surface at 298K. This agrees with previous reports that at UHV condition *l*-CO_2 was only observed at temperatures below 130K.

l-CO_2 on Ag surface with surface oxygen

In the presence of isolated surface O, we found that *l*-CO_2 has ΔE_{ads} = −0.21 eV with C1s = −270.26 eV, but ΔG = +0.13 eV. Thus a pressure of ~30 Torr would be required to stabilize *l*-CO_2 on the O/Ag surface at 298K. This contrasts with observations for Cu, where sublayer O stabilized the adsorption of *l*-CO_2 on Cu surface under 0.7 Torr CO_2 partial pressure at 298K. This attraction resulted from the subsurface O in a tetrahedral site inducing Cu^+ character into the single Cu above it on the surface, which stabilized the *l*-CO_2. This oxygen promotion effect was not observed in this work because the O is chemisorbed on top of the Ag, which does not change the valence state of Ag.

b-CO_2 on Ag surface

We also investigated the stability of the *b*-CO_2 on Ag surface. The optimized structure for *b*-CO_2 is 2.012Å above Ag surface for C atom, and 2.145Å and 2.945Å for the two O atoms, respectively (**Figure S4-1c)**. The predicted C-O bond lengths are 1.283Å and 1.245Å, respectively, significantly increased compared to those of *g*- and *l*-CO_2 (1.176Å). The DFT finds that *b*-CO_2 is unfavorable by E_{ads} = +0.77 eV. Thus *b*-CO_2 is not stable the on pristine Ag surface.

4. The configuration of $(O=CO_2^{\delta-})$-$(H_2O)_{0\text{-}4}$ illustrated in top view

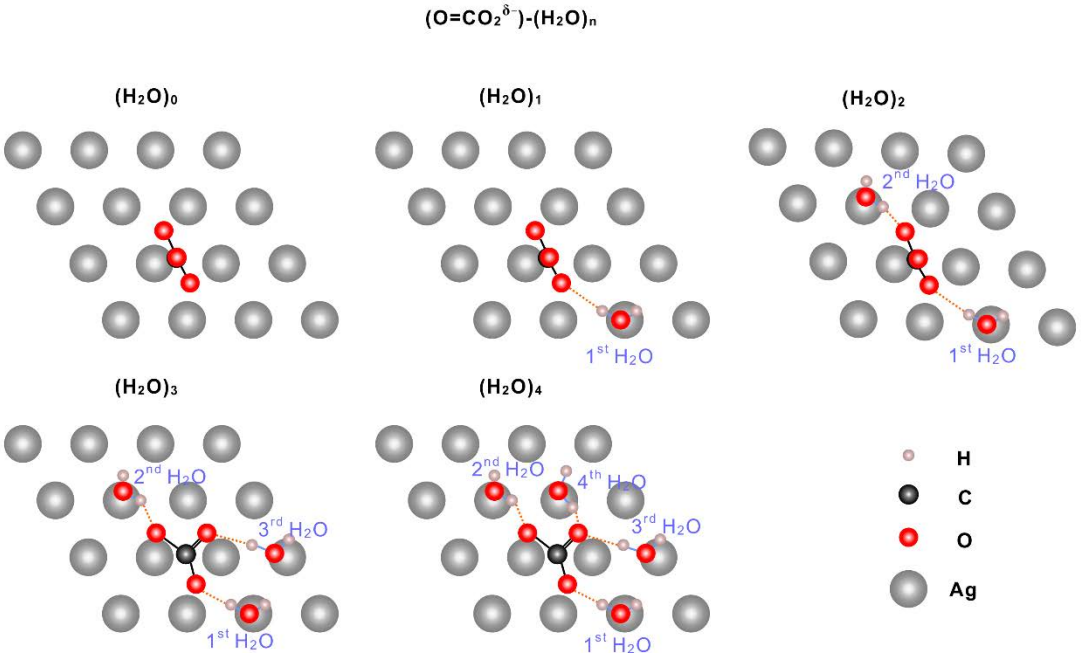

Figure S4-2. The configuration of $O=CO_2^{\delta-}$ stabilizing 0-4 water molecules illustrated in top view. $O=CO_2^{\delta-}$ is a carbonic acid-like structure with a $C=O_{up}$ double bond pointing up while the other two O bind to adjacent three fold Ag(111) sites. Adding the 1st and 2nd don't change the $O=CO_2^{\delta-}$ structure but forming two hydrogen bonds (shown as orange dashed lines) with each O bonded to the Ag surface. Adding 3rd and 4th H_2O forced the C=O bond to rotate from being perpendicular to the surface to being tilted nearly parallel to the surface, allowing the formation of HB from a 3rd and 4th surface H_2O to the two sp^2 lone pairs on the C=O unit. The hydrogen, carbon, oxygen, and silver atoms were represented with rosy brown, black, red, and gray balls, respectively. The C-O (and C=O), O-H, and hydrogen bonds were represented with black, blue, and orange sticks, respectively.

5. The geometrical structure of various adsorbates on the Ag surface

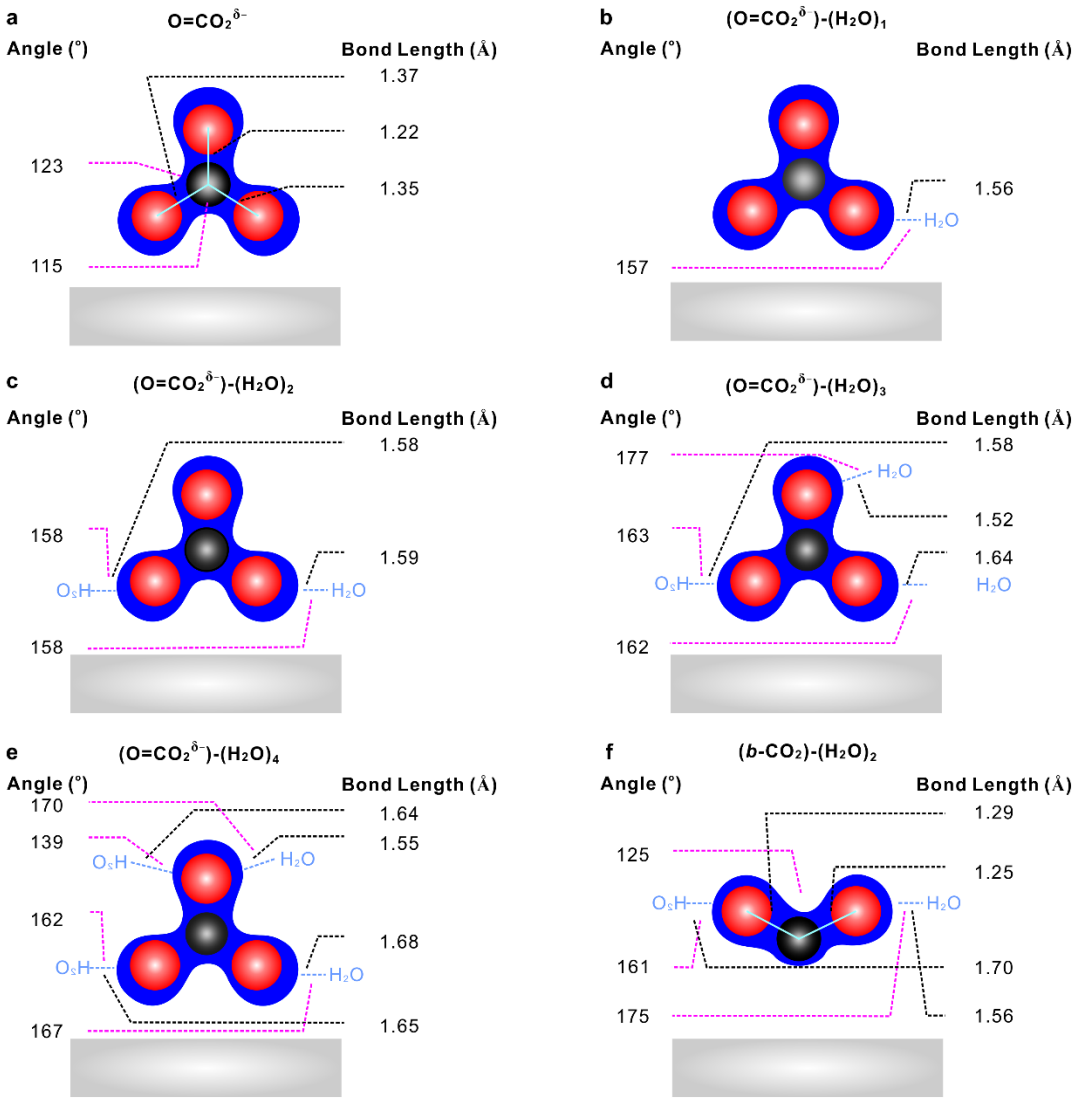

Figure S4-3. The geometrical structure of various adsorbates on the Ag surface.

$O=CO_2^{\delta-}$ on Ag

The $O=CO_2^{\delta-}$ has a $C=O_{up}$ double bond (1.222Å) pointing up while the other two O bind to adjacent three fold Ag(111) sites with C-O lengths of 1.365Å and 1.354Å, respectively, and O-Ag distances of 2.276Å.

$(O=CO_2^{\delta-})-(H_2O)_1$ on Ag

The hydrogen bond between H_2O_{ads} and $O{=}CO_2^{\delta-}$ did not change the structure of $O{=}CO_2^{\delta-}$. The hydrogen bond showed H-O bond length of 1.561Å, with an O-H-O angle of 157.5º

$(O{=}CO_2^{\delta-})$-$(H_2O)_2$ on Ag

Forming another hydrogen bond did not change the structure of $O{=}CO_2^{\delta-}$ as well. The hydrogen bonds showed H-O bond length of 1.585 Å and 1.583 Å with O-H-O angles of 157.5º and 158.3º, respectively.

$(O{=}CO_2^{\delta-})$-$(H_2O)_3$ on Ag

Adding a 3rd H_2O bends the terminal O=C toward to Ag surface to form a hydrogen bond. The hydrogen bonds showed H-O bond length of 1.576 Å and 1.637 Å with O-H-O angles of 163.3º and 161.8º for first two added waters, and H-O bond length of 1.517 Å with O-H-O angles of 176.8º for third added water, respectively. Besides, the third water formed another hydrogen bond with adjacent H_2O showed H-O bond length of 1.970 Å and O-H-O angles of 140.9º.

$(O{=}CO_2^{\delta-})$-$(H_2O)_4$ on Ag

Forming another hydrogen bond with fourth H_2O did not change the structure of $O{=}CO_2^{\delta-}$. The hydrogen bonds showed H-O bond length of 1.646 Å and 1.678 Å with O-H-O angles of 162.1º and 166.9º for first two added waters, and H-O bond length of 1.547 Å and 1.638 Å with O-H-O angles of 170.4º and 139.4º for two additional waters, respectively.

(*b*-CO_2)-$(H_2O)_2$ on Ag

This configuration has C-O bond length of 1.293Å and 1.245Å and an O-C-O angle of 125.1º. The two hydrogen bond lengths are 1.704Å, and 1.556Å, with O-H-O angles of 160.7º and 174.7º respectively.

6. The electronic structure of various adsorbates on Ag surface

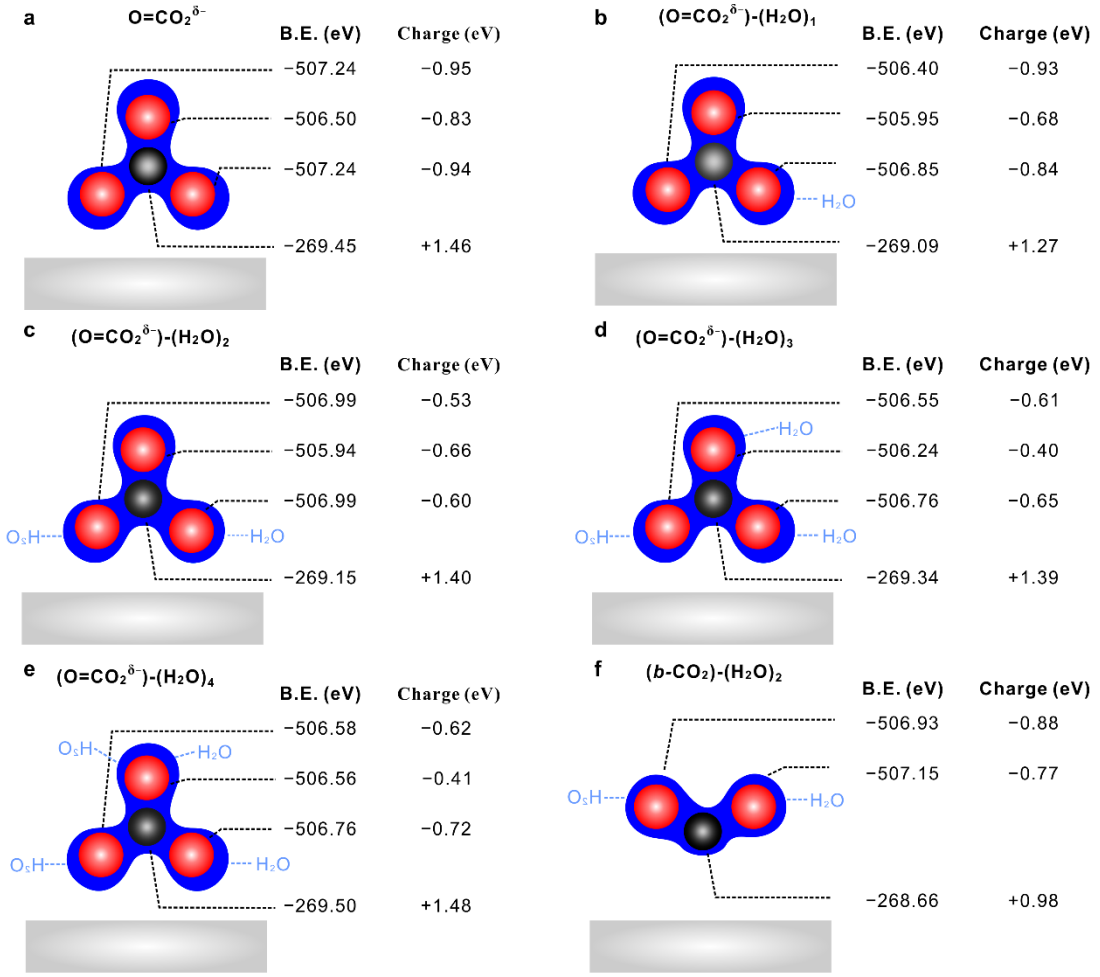

Figure S4-4. The electronic structure of various adsorbates on Ag surface.

$O=CO_2^{\delta-}$ on Ag

The two O_{down} have charges of −0.95 e^-, and −0.94 e^-, respectively, while O_{up} has a charge of −0.83 e^-. The corresponding O1s core level: two O1s= −507.24 eV, and one O1s= −506.50 eV.

$(O=CO_2^{\delta-})$-$(H_2O)_1$ on Ag

The charge on the O_{down} (O_1) hydrogen bonded to H_2O_{ads} (O_4) changes from 0.95e^- to 0.84e^- leading to O1s(1) = −506.85 eV, while the oxygen in the C=O bond (O_3) changes from 0.83e^- to 0.68e^- with O1s(3) = −505.95 eV, and the charge on the other O_{down} (O_2) remains unchanged with O1s(2) = −506.40 eV. The H_2O_{ads} (O_4) leads to O1s(4) = −507.29 eV.

(O=$CO_2^{\delta-}$)-$(H_2O)_2$ on Ag

The O1s of the C=O has charge of −0.53e^-, with the O1s = −505.94 eV, while the two O attaching to H_2O have charge of −0.6e^- and −0.66e^-, respectively, with two O1s = −506.99 eV, and the two O of H_2O have O1s = −507.43 eV.

(O=$CO_2^{\delta-}$)-$(H_2O)_3$ on Ag

The O1s of the C=O has charge of −0.40e^-, with the O1s = −506.24 eV, while another two O have charge of −0.61e^- and −0.65e^-, respectively, with two O1s = −506.55 eV and −506.76 eV, and the three O of H_2O have O1s = −507.08 eV, −507.25 eV and −507.32 eV, respectively,

(O=$CO_2^{\delta-}$)-$(H_2O)_4$ on Ag

The O1s of the C=O has charge of −0.41e^-, with the O1s = −506.56 eV, while another two O have charge of −0.62e^- and −0.72e^-, respectively, with two O1s = −506.58 eV and −506.76 eV, and the four O of H_2O have O1s = −507.06 eV, −507.14 eV, −507.57 eV and −507.42 eV, respectively,

(*b*-CO_2)-$(H_2O)_2$ on Ag

Two O of the *b*-CO_2 have charges of 0.88e^- and 0.77e^-, respectively, with O1s(1) = −506.93eV , O1s(2) = −507.15 eV, the O of the corresponding H_2O_{ads} have O1s(3) = −507.48 eV, O1s(4) = −507.81 eV.

7. APXPS of pristine and oxygen-covered Ag surfaces and the adsorbates on the surfaces

7.1. XPS characterization of the pristine Ag surface

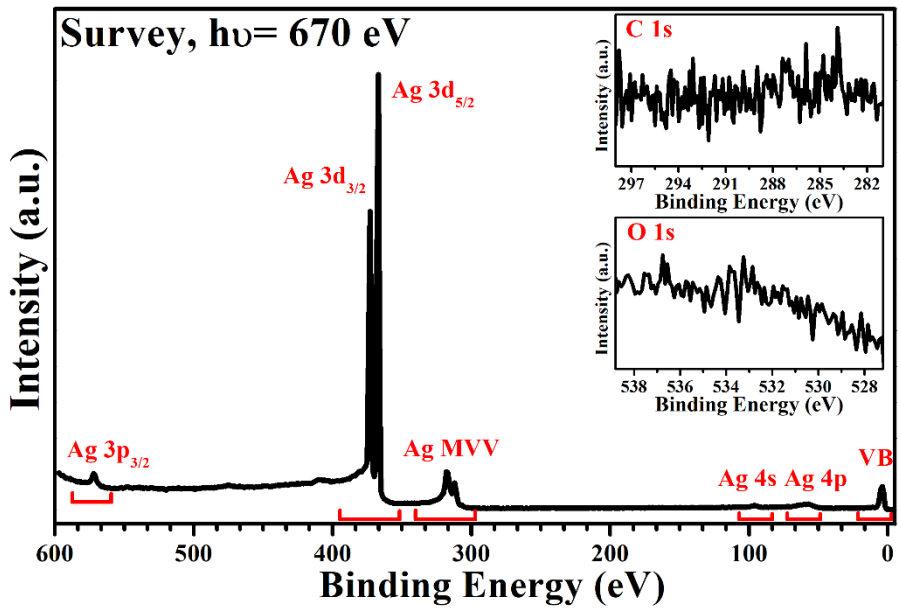

Figure S4-5. The survey and high resolution C1s and O1s scans of the pristine Ag foil.

The Ag foil was cleaned prior to each experiment, including the O_2 surface treatment, 0.3 Torr CO_2 adsorption, and 0.3 Torr CO_2 + 0.15 Torr H_2O co-adsorption. The pristine Ag surface was prepared by repeated Ar sputtering and vacuum annealing. The Ag surface was characterized by XPS to ensure no detectable contamination on the surface. The survey with a binding energy range of -10 to 600 eV, and high resolution scans of C1s and O1s recorded at photon energy of 670 eV (**Figure S4-5**). The energy scale of the spectra was calibrated using the Ag3d $_{5/2}$ peak locating at 368.2 eV. The survey spectra showed only Ag signals, including core level peaks and an auger peak. No detectable C- and O- based contamination were observed in the high resolution scans recorded in the insets.

7.2. O1s spectra of oxygen treated Ag surface before and after CO_2 adsorption

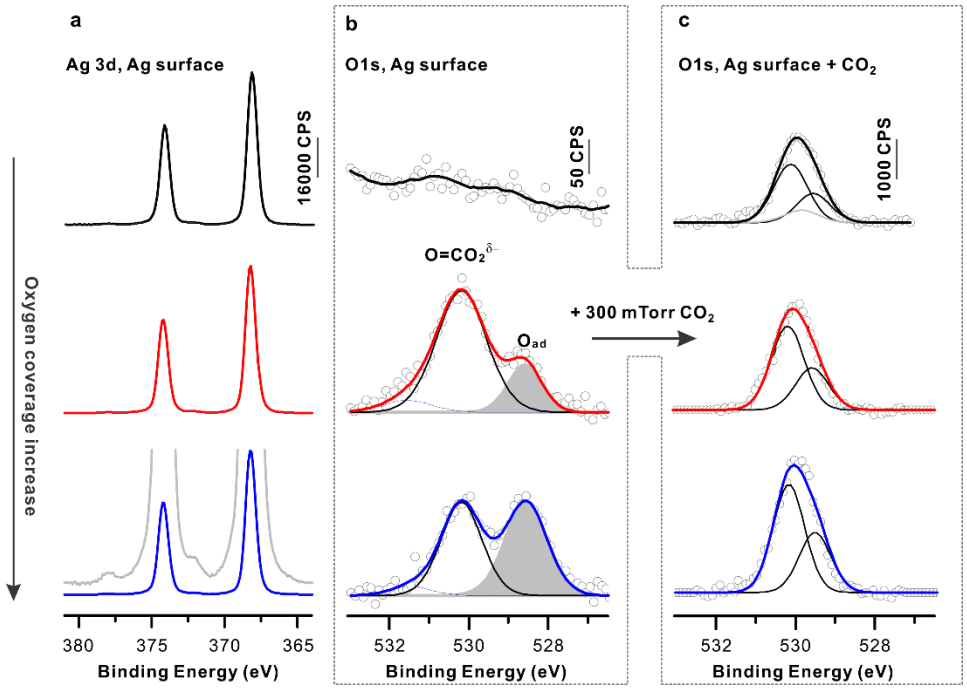

Figure S4-6. APXPS of pristine and oxygen-covered Ag surfaces and the adsorbates on them. a, Ag3d spectra of pristine and oxygen treated Ag surface. The regions of the loss feature peaks was enlarged to indicate the metallic feature of the Ag surface after O_2 treatment. **b,** C1s spectra of pristine and oxygen treated Ag surface. Three peaks locating at 528.5 eV, 530.3 eV, and 531.5 eV were observed on oxygen covered Ag surface. These peaks are assigned as the atomically adsorbed O on the surface, signal from $O{=}CO_2^{\delta-}$, and surface OH bonds, respectively. **c,** O1s spectra of pristine and oxygen treated Ag surface after CO_2 adsorption. The O_{ads} peak showed before the CO_2 adsorption disappeared after CO_2 adsorption. The signal attenuation due to 300 mTorr CO_2 in the chamber has been calibrated by applying the substrate signal decay.

The O1s spectra recorded on clean and oxygen covered surfaces. Surfaces with low and high oxygen coverage surfaces were obtained by heating pristine Ag foil under 40 mTorr O_2 at 400 K for 5 mins and under 60 mTorr O_2 at 400 K for 15 mins, respectively. O1s spectra recorded on oxygen covered Ag surface showed three peaks locating at 528.5 eV, 530.3 eV, and 531.5 eV, respectively. The peak locating at 528.5 eV is between the previous observed signal of Ag_2O and signal from Ag (111)- p(4 × 4)- O surface reconstruction[21]. However, we haven't observed any changes on the Ag peak (as shown in **Figure S4-6a**), which may show a peak lower than the bulk metallic peak if these two cases appeared. Thus, we tentatively assign this peak as the atomically adsorbed O on the surface[22-24]. The peak locating at 530.3 eV was assigned to the peak of $O{=}CO_2^{\delta-}$, which has also been reported previously[24]. This assignment is supported by checking the C1s signal and the C:O atomic ratios, which are around 1:3 during the O_2 adsorption process (**Figure S4-7**). Since the peak position of this species in both the C1s and O1s spectra is located at the identical position as those we observed later with CO_2 adsorption, we are confident to assign them to $O{=}CO_2^{\delta-}$. This is further evidenced by its unstable of peak B

above 430K. This is against the previous assigned bulk dissolved O peak, locating at similar position, is stable at up to 800K[16,17]. By applying the sensitivity factors for both Ag3d and O1s, which are about 1.8 and 0.32, respectively, under photon energy of 670 eV, the Ag:O atomic ratio is around 0.01 and 0.015 for low and high oxygen covered surface, respectively. The maintenance of the metallic state of Ag and the low coverage of oxygen on the Ag further ruled out the formation of the Ag (111)- p(4 × 4)- O surface reconstruction.

Finally, the peak located at the 531.5 eV is assigned to the OH signal, which has been well established in the previous work[14].

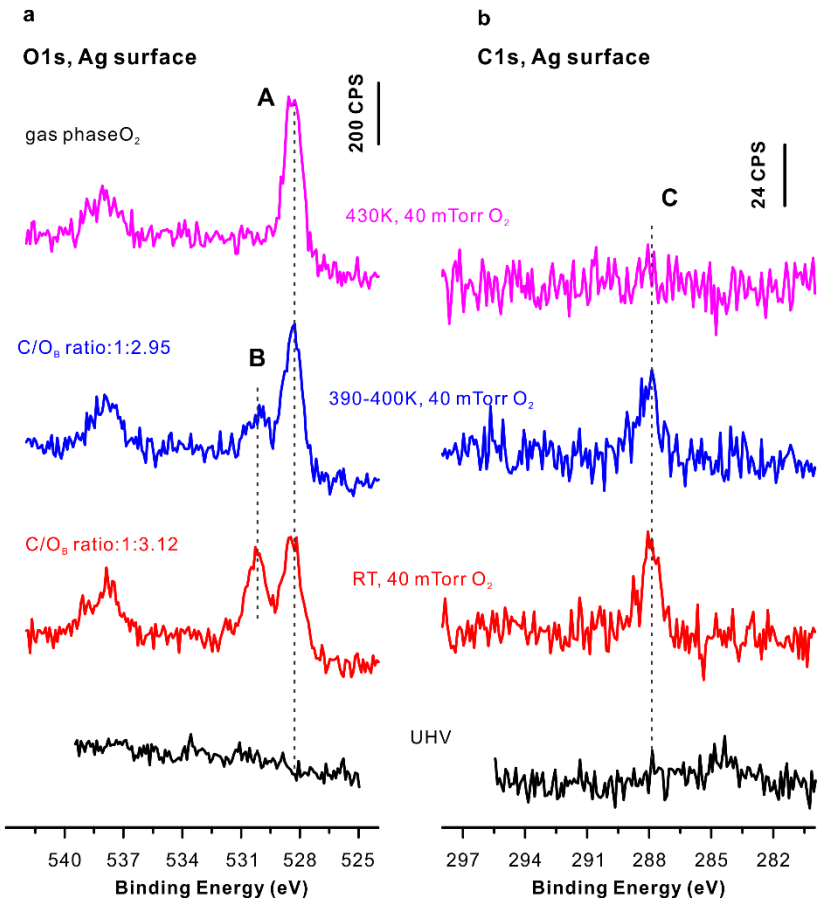

Figure S4-7. APXPS of Ag surfaces during O_2 dose. (a) O1s and (b) C1s spectra taken at UHV, 40 mTorr O_2 at room temperature, 40 mTorr O_2 at around 400 K, and 40 mTorr O_2 at 430K were recorded as black, red, blue, and pink, respectively, from bottom to top.

7.3. C1s spectra of Ag surface with different oxygen coverage after CO_2 adsorption

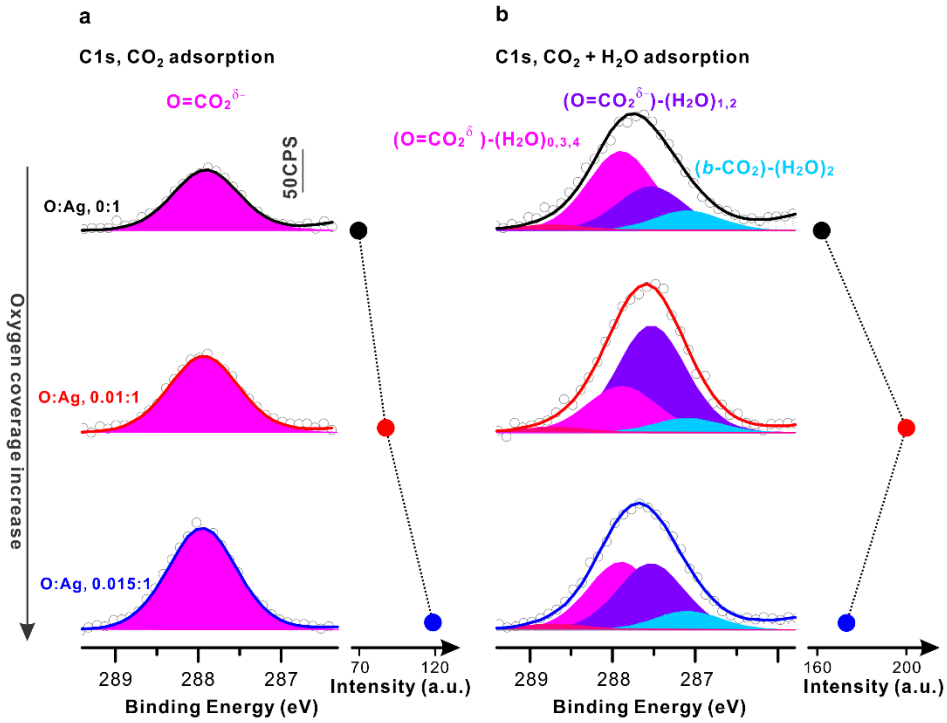

Figure S4-8: C1s spectra of adsorbates on Ag surface after CO_2 adsorption both alone and in the presence of H_2O. a, C1s spectra of CO_2 adsorption on various Ag surfaces. As the surface O_{ad} coverage is increased, additional CO_2 adsorbed on the surface to form $O{=}CO_2^{\delta-}$ while suppressing CO_2 dissociated surface carbon formation, thus leading to an increase in $O{=}CO_2^{\delta-}$ signals. **b,** C1s spectra of CO_2 + H_2O adsorption on various Ag surfaces. The total adsorbate signal from CO_2+H_2O co-adsorption shows a volcano-shaped dependence on the surface oxygen coverages.

The formation of each $O{=}CO_2^{\delta-}$ species requires one O_{ad} prior to the CO_2 adsorption. Starting with the pristine Ag surface, we found that exposing Ag to CO_2 leads to the formation of $O{=}CO_2^{\delta-}$ where the surface adsorbed oxygen (O_{ad}) atom required likely came from CO_2 dissociation, where the CO desorbs into the gas phase while leaving behind an O_{ad}. Some surface O_{ad} may desorb as O_2, but we conclude that some are available to react with *g*-CO_2 to form $O{=}CO_2^{\delta-}$.

The surface C species formed from CO_2 dissociation cover available Ag sites and thus inhibit CO_2 adsorption. Interestingly, as the surface O coverage is increased, additional CO_2 adsorbed on the surface to form $O{=}CO_2^{\delta-}$ while suppressing CO_2 dissociated surface carbon formation, thus leading to an increase in $O{=}CO_2^{\delta-}$ and a decrease in sp^2 C=C signals (showing in the later section).

7.4. C1s spectra of Ag surface with different oxygen coverage after CO_2 adsorption in the presence of H_2O

Using the QM predicted C1s levels for each of the three stable species, we were able to deconvolute the APXPS adsorbate peak measurements. The newly formed surface adsorbates with decreased C1s binding energy of 0.4 eV and 0.8 eV with respect to $O{=}CO_2^{\delta-}$ peak represent the $(O{=}CO_2^{\delta-})$-$(H_2O)_n$ (n=1,2) and (*b*-CO_2)-$(H_2O)_2$ clusters on surface, respectively, with n=1,2, showing a negligible energy difference of 0.06 eV, too small to measure. $(O{=}CO_2^{\delta-})$-$(H_2O)_2$ also stabilizes an additional two waters that shifted back the C1s to the positon of $O{=}CO_2^{\delta-}$.

Considering that the surface adsorbate, $O{=}CO_2^{\delta-}$, and surface water stabilize each other on the surface through HB, we expect increased surface adsorbate coverage when dosing CO_2 in the presence of H_2O. Indeed the C1s spectra show a dramatically increased adsorbate signal compared to that from adsorption of CO_2 alone.

Interestingly, the total adsorbate signal from CO_2+H_2O co-adsorption shows a volcano-shaped dependence on the surface oxygen coverages in contrast to the linear positive correlation between surface oxygen coverage and dry CO_2 adsorption. We explain this in terms of the competitive adsorption among the surface species. Given a coverage of O_{ad}, we expect adsorption competition between (a) CO_2 reacting with O_{ad} to form $O{=}CO_2^{\delta-}$ requiring 2 sites (b) one to four H_2O coordinating to $O{=}CO_2^{\delta-}$ requiring 3 to 6 sites and (c) H_2O reacting with O_{ad} to form two OH_{ad} requiring 2 or 3 sites. Thus increased amounts of $O{=}CO_2^{\delta-}$ block further adsorption of H_2O_{ads}, which suppresses the effect of H_2O_{ads} in stabilizing the surface adsorbates. For the clean Ag surface, surface adsorption is suppressed by the formation of sp^2 carbon from CO_2 dissociation, showing decreased amounts of surface adsorbates compared to oxygen covered Ag surfaces. Thus, having too many surface O (more than 0.15 O per Ag) or none at all both lead to decreased adsorbates on the surface.

8. Surface products and adsorbate signals from CO_2 adsorption on pristine and oxygen covered Ag surfaces

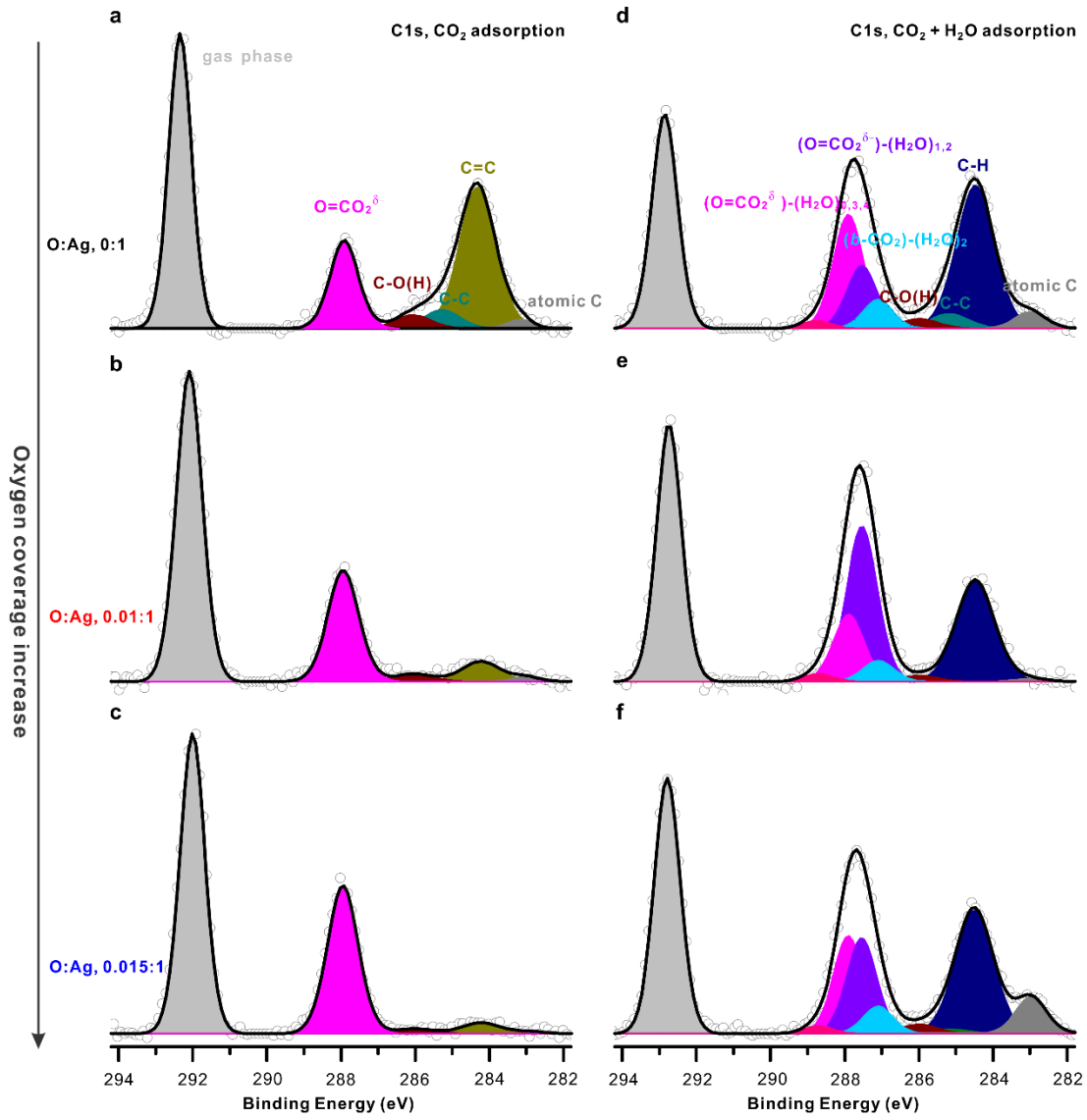

Figure S4-9. The detailed peak deconvolution of the C1s spectra recorded on various Ag surface under CO_2 adsorption alone and in the presence of H_2O.

The C1s spectra were divided into three parts: the surface reaction products, surface adsorbates, and gas phase peak. The chemical species can be assigned as atomic C (283.0 eV), sp^2 C=C (284.2 eV), sp^3 C-C (285.2 eV), C-O(H) (286.0 eV), $O{=}CO_2^{\delta-}$ (287.9 eV), *g*-CO_2 (292-293 eV)[25,26]. During the coadsorption of CO_2 and H_2O, a new species appeared at 284.5 eV between the peaks of sp^2 C=C and sp^3 C-C. Detailed assignment for this species has not been made, but it may be related to the C-H bond formation, due to the reaction

between sp^2 C=C and H_2O on Ag surface. We also observed the ionic carbonate species at 288.7 eV in the C 1s XPS spectra. The appearance of CO_3^{2-} may originate from some side reactions, which have been reported previously. The energy difference of ~0.8 eV between the CO_3^{2-} and $O{=}CO_2^{\delta-}$ peaks provides direct evidence that these two species have completely different electronic structure properties.

Adding H_2O also changes the low energy region carbon species by shifting the main feature to higher binding energy. The peak shift is ascribed to the appearance of new species between sp^2 C=C carbon and sp^3 C-C carbon peaks. Detailed assignment for this species has not been made, but it may be related to the C-H bond formation, due to the reaction between sp^2 C=C and H_2O on Ag surface. A similar reaction has been reported on Al surface[27]. Another surface reaction product that should be specially noted is the ionic carbonate species at 288.7 eV in the C 1s XPS spectra. The appearance of CO_3^{2-} may originate from some side reactions, which have been reported previously [26]. The energy difference of ~0.8 eV between the CO_3^{2-} and $O{=}CO_2^{\delta-}$ peaks provides direct evidence that these two species have totally different electronic structure properties.

9. Dynamic process of CO_2 adsorption alone and in the presence of O_2 on pristine Ag surface:

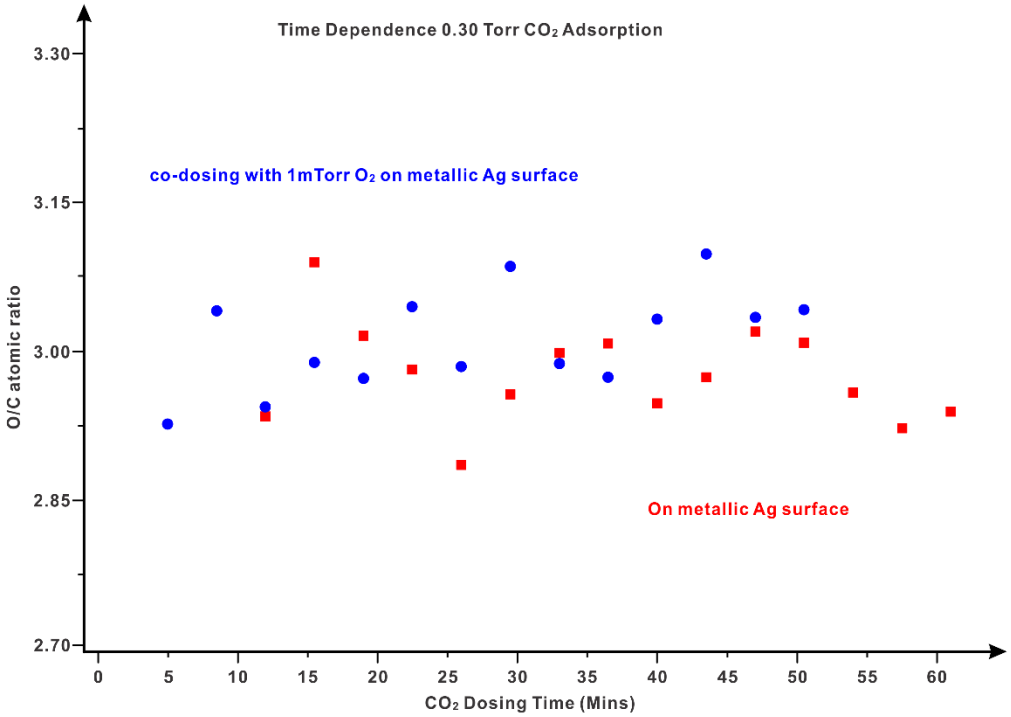

Figure S4-10. The O:C atomic ratio of surface adsorbates as a function of CO_2 dosing time.

10. The proposed reaction pathway

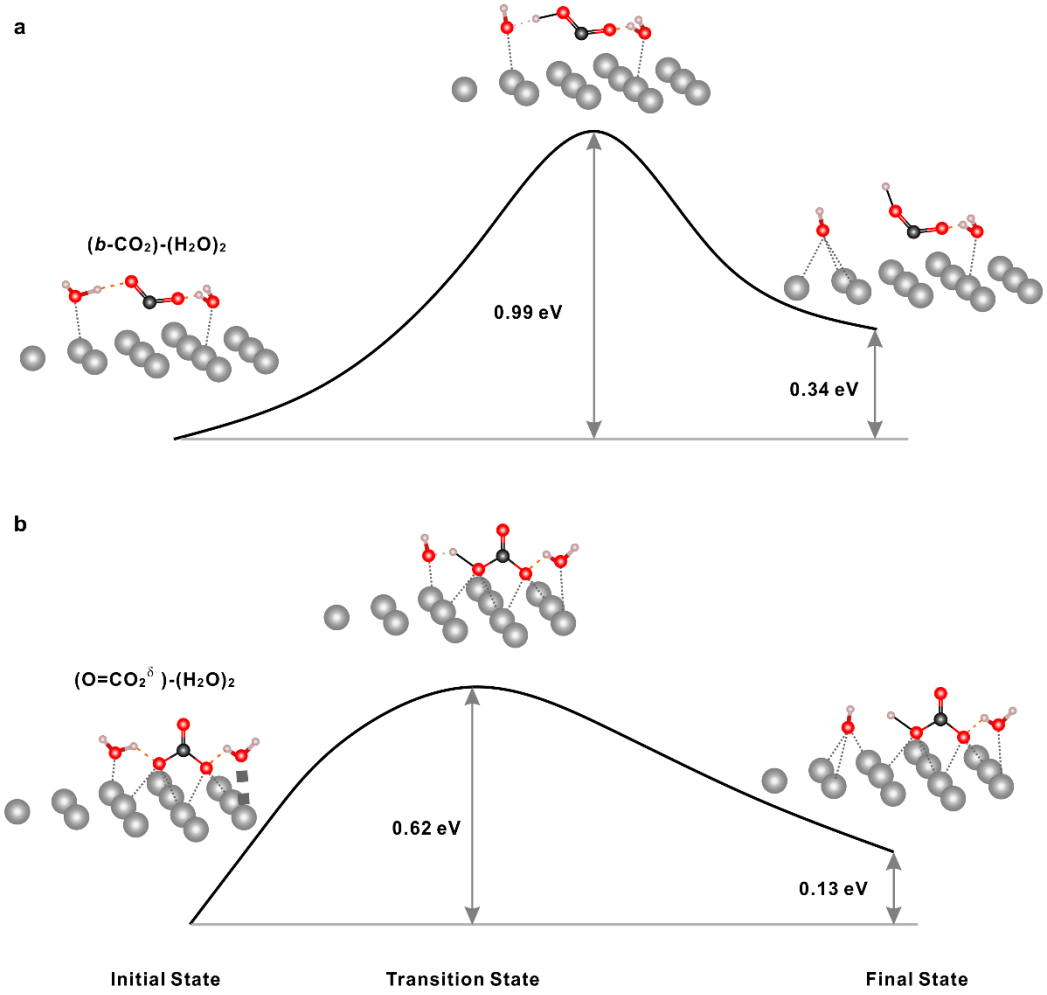

Figure S4-11. Energy barrier of H transferring process originating from *b*-CO_2 and $O{=}CO_2^{\delta-}$.

Hydrogenation process of *b*-CO_2 with one H transferred from attached H_2O molecule to form the HOCO intermediate plus OH_{ad} (**Figure S4-11a**). The energy barrier for this process is 0.99 eV. In the initial state, the O-H bond lengthen for the attached H_2O is 1.025 Å, while the HB lengthen is 1.557 Å. In the transition state with a H transferred, the distance between the attached H and the O in H_2O is 2.856 Å. While this distance increased to 3.823 Å in the final state

Hydrogenation process of $O{=}CO_2^{\delta-}$ with one H transferred from attached H_2O molecule to form the (C=O)(O)(OH) intermediate plus OH_{ad} (**Figure S4-11b**). The energy barrier for this process is 0.62 eV. In the initial state, the O-H bond lengthen for the attached H_2O is 1.023 Å, while the HB lengthen is 1.582 Å. In the transition state with a H transferred, the

distance between the attached H and the O in H_2O is 2.576 Å. While this distance increased to 4.357 Å in the final state.

11. Simulated Vibrational frequency for all possible adsorbates on Ag surface with CO_2 adsorption both alone and in the presence of H_2O.

CO_2 adsorption		
Species	**Bond**	**vibrational frequency (cm^{-1})**
$O{=}CO_2^{\delta-}$	C-O stretch	908.06
$O{=}CO_2^{\delta-}$	C=O stretch	1663.51
CO_2+H_2O adsorption		
Species	**Bond**	**vibrational frequency (cm^{-1})**
H_2O	O-H stretch	3709.04 (anti); 3612.91 (sym)
	H-O-H bend	1555.86
$O{=}CO_2^{\delta-}$+H_2O	C-O stretch	900.79
	C=O stretch	1659.96
	O-H stretch	3777.14; 2730.96
$O{=}CO_2^{\delta-}$+2H_2O	C-O stretch	992.578159
	C=O stretch	1669.03
	O-H stretch	3772.44, 3767.26
$O{=}CO_2^{\delta-}$+3H_2O	C-O stretch	931.07
	C=O stretch	1610.86
	O-H stretch	3765.34; 2743.9; 3764.92
$O{=}CO_2^{\delta-}$+4H_2O	C-O stretch	935.66
	C=O stretch	1600.43
	O-H stretch	3762.63; 2765.34; 3720.03
b-CO_2+2H_2O	O-H stretch	3763.64; 3761.32; 3180.168; 2739.99

Table S4-1. Vibrational frequency for all possible species on the surface with CO_2 adsorption both alone and in the presence of H_2O.

We report mainly stretching frequencies for C-O, C=O, and O-H as they are unambiguous. Other modes such as bending, scissoring and etc. are mixed up with species nearby or first layer metal, hence making them hard to categorize. The vibrational frequency of the C=O bond ranges from 1659.96 to 1600.43 cm^{-1} for 0 to 4 H_2O. But we expect the cases with 0 to 2 water to be much more intense due to image charge enhancement of the dipole derivative. This may provide an experimental means to discriminate the various species on the surface.

12. Comparison of CO_2 adsorption on Ag and Cu

	Ag		Cu	
adsorbate	**Stability**	**ΔG (eV)**	**Stability**	**ΔG (eV)**
***l*-CO_2**	Not stable	+0.19 (PBE-D3)	Stable with sublayer oxygen	−0.39 (M06L)
***b*-CO_2**	Stable with two hydrogen bonds	−0.18 (PBE-D3)	Stable with one hydrogen bond and a sublayer oxygen	−0.06 (M06L)
O=$CO_2^{\delta-}$	Stable with surface O	−0.28 (PBE-D3)	Not stable	+1.33 (PBE-D3)
	Stable with one hydrogen bonds	−0.43 (PBE-D3)		
	Stable with two hydrogen bonds	−0.48 (PBE-D3)		
	Stable with three hydrogen bonds	−0.37 (PBE-D3)		
	Stable with four hydrogen bonds	−0.19 (PBE-D3)		

Table S4-2. The summary of the stability and free energy of possible surface adsorbates on Ag and Cu surfaces.

References:

1 *Introduction to Solid State Physics, 7th Ed*. (Wiley India Pvt. Limited, 2007).

2 Kresse, G. & Furthmüller, J. Efficient Iterative Schemes for Ab Initio Total-Energy Calculations Using a Plane-Wave Basis Set. *Physical Review B* **54**, 11169-11186 (1996).

3 Johnson, E. R. & Becke, A. D. A Post-Hartree-Fock Model of Intermolecular Interactions: Inclusion of Higher-Order Corrections. *The Journal of Chemical Physics* **124**, 174104 (2006).

4 Grimme, S., Antony, J., Ehrlich, S. & Krieg, H. A Consistent and Accurate Ab Initio Parametrization of Density Functional Dispersion Correction (Dft-D) for the 94 Elements H-Pu. *The Journal of Chemical Physics* **132**, 154104 (2010).

5 Cheng, T. et al. Mechanism and Kinetics of the Electrocatalytic Reaction Responsible for the High Cost of Hydrogen Fuel Cells. *Physical Chemistry Chemical Physics* **19**, 2666-2673 (2017).

6 Cheng, T., Xiao, H. & Goddard, W. A. Full Atomistic Reaction Mechanism with Kinetics for Co Reduction on Cu(100) from Ab Initio Molecular Dynamics Free-Energy Calculations at 298 K. *Proceedings of the National Academy of Sciences* **114**, 1795-1800 (2017).

7 Cheng, T., Xiao, H. & Goddard, W. A. Free-Energy Barriers and Reaction Mechanisms for the Electrochemical Reduction of Co on the Cu(100) Surface, Including Multiple Layers of Explicit Solvent at Ph 0. *The Journal of Physical Chemistry Letters* **6**, 4767-4773 (2015).

8 Cheng, T., Xiao, H. & Goddard, W. A. Nature of the Active Sites for Co Reduction on Copper Nanoparticles; Suggestions for Optimizing Performance. *Journal of the American Chemical Society* **139**, 11642-11645 (2017).

9 Ping, Y., Nielsen, R. J. & Goddard, W. A. The Reaction Mechanism with Free Energy Barriers at Constant Potentials for the Oxygen Evolution Reaction at the Iro2 (110) Surface. *Journal of the American Chemical Society* **139**, 149-155 (2017).

10 Xiao, H., Cheng, T., Goddard, W. A. & Sundararaman, R. Mechanistic Explanation of the Ph Dependence and Onset Potentials for Hydrocarbon Products from Electrochemical Reduction of Co on Cu (111). *Journal of the American Chemical Society* **138**, 483-486 (2016).

11 Xiao, H., Cheng, T. & Goddard, W. A. Atomistic Mechanisms Underlying Selectivities in C1 and C2 Products from Electrochemical Reduction of Co on Cu(111). *Journal of the American Chemical Society* **139**, 130-136 (2017).

12 Xiao, H., Goddard, W. A., Cheng, T. & Liu, Y. Cu Metal Embedded in Oxidized Matrix Catalyst to Promote Co₂ Activation and Co Dimerization for Electrochemical Reduction of Co₂. *Proceedings of the National Academy of Sciences* **114**, 6685-6688 (2017).

13 Perdew, J. P., Burke, K. & Ernzerhof, M. Generalized Gradient Approximation Made Simple. *Physical Review Letters* **77**, 3865-3868 (1996).

14 Favaro, M. et al. Subsurface Oxide Plays a Critical Role in Co₂ Activation by Cu(111) Surfaces to Form Chemisorbed Co₂, the First Step in Reduction of Co₂. *Proceedings of the National Academy of Sciences* **114**, 6706-6711 (2017).

15 Garza, A. J., Bell, A. T. & Head-Gordon, M. Is Subsurface Oxygen Necessary for the Electrochemical Reduction of Co2 on Copper? *The Journal of Physical Chemistry Letters* **9**, 601-606 (2018).

16 Nagy, A. J. et al. The Correlation of Subsurface Oxygen Diffusion with Variations of Silver Morphology in the Silver–Oxygen System. *Journal of Catalysis* **182**, 417-429 (1999).

17 Bao, X. et al. On the Nature of the Active State of Silver During Catalytic Oxidation of Methanol. *Catalysis Letters* **22**, 215-225 (1993).

18 Li, W.-X., Stampfl, C. & Scheffler, M. Subsurface Oxygen and Surface Oxide Formation at Ag(111): A Density-Functional Theory Investigation. *Physical Review B* **67**, 045408 (2003).

19 Todorova, M. et al. Role of Subsurface Oxygen in Oxide Formation at Transition Metal Surfaces. *Physical Review Letters* **89**, 096103 (2002).

20 Li, W.-X., Stampfl, C. & Scheffler, M. Why Is a Noble Metal Catalytically Active? The Role of the O-Ag Interaction in the Function of Silver as an Oxidation Catalyst. *Physical Review Letters* **90**, 256102 (2003).

21 Heine, C., Eren, B., Lechner, B. A. J. & Salmeron, M. A Study of the O/Ag(111) System with Scanning Tunneling Microscopy and X-Ray Photoelectron Spectroscopy at Ambient Pressures. *Surface Science* **652**, 51-57 (2016).

22 Campbell, C. T. & Paffett, M. T. The Interactions of O2, Co and Co2 with Ag(110). *Surface Science* **143**, 517-535 (1984).

23 T. Campbell, C. An Xps Study of Molecularly Chemisorbed Oxygen on Ag(111). *Surface Science* **173**, L641-L646 (1986).

24 Campbell, C. T. Atomic and Molecular Oxygen Adsorption on Ag(111). *Surface Science* **157**, 43-60 (1985).

25 Taifan, W., Boily, J.-F. & Baltrusaitis, J. Surface Chemistry of Carbon Dioxide Revisited. *Surface Science Reports* **71**, 595-671 (2016).

26 Deng, X. et al. Surface Chemistry of Cu in the Presence of Co2 and H2o. *Langmuir* **24**, 9474-9478 (2008).

27 Carley, A. F., Davies, P. R., Moser, E. M. & Roberts, M. W. Facile Hydrogenation of Carbon Dioxide at Al(111) Surfaces: The Role of Coadsorbed Water. *Surface Science* **364**, L563-L567 (1996).

Appendix D
Supplementary Information for Chapter 5

Table S5-1 Formation energy dG as a function of pressure from the QM based CRN.

			Pressure	150 mtorr	100 mtorr	50 mtorr	30 mtorr	15 mtorr	5 mtorr	10E-6 torr
			Temperature	298 K	298 K	298 K	298 K	298 K	298 K	298 K
#	description	Initial	final	dG	dG	dG	dG	dG	dG	dG
1	adsorption	x4+x1	x4+x5	-0.31	-0.30	-0.28	-0.27	-0.25	-0.22	0.00
2	adsorption	x3+x1	x3+x5	-0.09	-0.08	-0.06	-0.05	-0.03	0.00	0.22
3	reaction	x4+x5	2*x3	-0.47	-0.47	-0.47	-0.47	-0.47	-0.47	-0.47
4	diffusion	x5+x3	x2+x3	0.31	0.31	0.31	0.31	0.31	0.31	0.31
5	diffusion	x5+x4	x2+x4	0.46	0.46	0.46	0.46	0.46	0.46	0.46
6	desorption	x2	x1	-0.16	-0.17	-0.19	-0.20	-0.22	-0.25	-0.47
7	adsorption	x1	x2	0.16	0.17	0.19	0.20	0.22	0.25	0.47
8	desorption	x5+x3	x3+x1	0.09	0.08	0.06	0.05	0.03	0.00	-0.22
9	desorption	x5+x4	x4+x1	0.31	0.30	0.28	0.27	0.25	0.22	0.00
10	adsorption	x5+x1	x6	-0.02	-0.01	0.01	0.02	0.04	0.07	0.29
11	desorption	x6	x5+x1	0.02	0.01	-0.01	-0.02	-0.04	-0.07	-0.29

Table S5-1. Formation energy dG as a function of pressure from the QM based CRN. Example pressure conditions from 10-6 to 150mtorr are included here. For a complete table of surface species concentration with finer grids and larger scope of temperature and pressure condition, please refer to the big datasheet result.txt.